



저작자표시-비영리-변경금지 2.0 대한민국

이용자는 아래의 조건을 따르는 경우에 한하여 자유롭게

- 이 저작물을 복제, 배포, 전송, 전시, 공연 및 방송할 수 있습니다.

다음과 같은 조건을 따라야 합니다:



저작자표시. 귀하는 원저작자를 표시하여야 합니다.



비영리. 귀하는 이 저작물을 영리 목적으로 이용할 수 없습니다.



변경금지. 귀하는 이 저작물을 개작, 변형 또는 가공할 수 없습니다.

- 귀하는, 이 저작물의 재이용이나 배포의 경우, 이 저작물에 적용된 이용허락조건을 명확하게 나타내어야 합니다.
- 저작권자로부터 별도의 허가를 받으면 이러한 조건들은 적용되지 않습니다.

저작권법에 따른 이용자의 권리는 위의 내용에 의하여 영향을 받지 않습니다.

이것은 [이용허락규약\(Legal Code\)](#)을 이해하기 쉽게 요약한 것입니다.

[Disclaimer](#)

이학박사 학위논문

Phase Transition Dynamics of Quenched
Spinor Bose-Einstein Condensates with
Antiferromagnetic Interactions

퀸치된 반강자성 스피너 보즈-아인슈타인 응집체의 상 전이
동역학

2018년 8월

서울대학교 대학원

물리·천문 학부

강 세 지

Phase Transition Dynamics of Quenched Spinor
Bose-Einstein Condensates with Antiferromagnetic
Interactions

퀸치된 반강자성 스피너 보즈-아인슈타인 응집체의 상 전이
동역학

지도교수 신 용 일

이 논문을 이학박사 학위 논문으로 제출함

2018년 5 월

서울대학교 대학원

물리 · 천문 학부

강 세 지

강세지의 박사 학위 논문을 인준함

2018년 6 월

위 원 장	제 원 호	(인)
부위원장	신 용 일	(인)
위 원	민 홍 기	(인)
위 원	Uwe R. Fischer	(인)
위 원	최 재 윤	(인)

**Phase Transition Dynamics of Quenched
Spinor Bose-Einstein Condensates with
Antiferromagnetic Interactions**

by

Seji Kang, B.S.

Dissertation

Presented to the Faculty of the Graduate School of

Seoul National University

in Partial Fulfillment

of the Requirements

for the Degree of

Doctor of Philosophy

Seoul National University

August 2018

Abstract

Phase Transition Dynamics of Quenched Spinor Bose-Einstein Condensates with Antiferromagnetic Interactions

Seji Kang

Department of Physics and Astronomy
The Graduate School
Seoul National University

Understanding non-equilibrium systems are challenging, because they are usually accompanied by either strong time-dependent perturbations or non-vanishing energy and mass flows. Many efforts have been made to study the far-from-equilibrium dynamics by extending the statistical frame of an equilibrium system. One promising progress has been made in the field of phase transition dynamics near a critical point. The significant questions for phase transition dynamics contain how the many-body system evolves into a newly ordered state and how many excitations occurs. It is well known that the scaling behavior in the vicinity of a critical point is determined by the correlation length, the dimension of the system, and the symmetry of an order parameter in the thermal equilibrium. This *scaling hypothesis* can be extended to the dynamic scaling hypothesis of an out-of-equilibrium system across a phase transition. At the end of the evolution, topological defects are formed as a result of excitations.

One typical protocol is a quantum quench that explores a non-equilibrium system across a phase transition by suddenly changing the system's Hamiltonian. However, for a many-body quantum system, the time-evolution of far-

from-equilibrium system is extremely complicated for study in either an analytical or numerical way, which requires an experimental approach. Ultracold atomic gases provide a good platform to study these non-equilibrium dynamics in a highly controllable and well-isolated manner with sufficiently long coherent time.

In this thesis, we introduce some methods to induce non-equilibrium dynamics through quenched phase transition in a quasi-2D spinor Bose-Einstein condensate (BEC) with antiferromagnetic interactions. We then discuss its evolution. There are two ground states for an antiferromagnetic spinor BEC depending on the quadratic Zeeman energy, q : the easy-axis polar (EAP) phase for $q > 0$ and the easy-plane polar (EPP) phase for $q < 0$. The microwave dressing technique allow us to access both positive and negative values of q .

A BEC, initially prepared in the EAP state, becomes dynamically unstable when the q suddenly changes to negative. The EAP-to-EPP phase transition occurs through the transverse magnon excitations according to the mean-field theory. In addition, the dynamical instability is scaled with the quench depth of $|q|$. Then, the spin turbulence emerges, and the condensate enters a qualitatively different stage of the quench evolution. Interestingly, the time-space scaling is still preserved in the spin turbulence generation depending on q . As the spin turbulence decays, half-quantum vortices (HQVs) can be identified as a result of the EAP-to-EPP phase transition.

For the EPP state, the energy spectrum contains two magnon modes: transverse and axial magnon modes. Without any gapless axial magnon excitations, the EPP-to-EAP phase transition occurs due to the gapped transverse magnon excitations, similar to the EAP-to-EPP phase transition. Thus, the dynamical instability is also scaled with $|q|$. However, we can dynamically create

special solitons, named as magnetic composite solitons, which is terminated by HQVs by using the EPP-to-EAP phase transition. We investigate the structure of a magnetic composite-soliton in terms of spin texture and supercurrent. A magnetic composite-soliton splits into small pieces via the snake instability, which is caused by the mass velocity. It is possible for a magnetic composite-soliton to shrink into a singly charged vortex with a ferromagnetic core. In addition, we also observe the spin fluctuation effect on the dynamic instability, where the spin fluctuations arise from the axial magnon excitations.

This thesis also includes a study of how the circulating condensate relaxes into a rotating condensate with a vortex lattice in an anharmonic trapping potential. We drive the condensate to circulate around the trap center by circularly shaking the trapping potential. This method is one of the simplest ways to inject vortices in the condensate, which is analogous to what we typically do to rotate wine in a glass. Furthermore, we investigate the chirality of geometrical Hall effect by measuring the response of the condensate under various elliptical polarized driving. The geometrical Hall effect is caused by the 2D skyrmion spin texture, which has a finite Berry curvature so that the neutral atoms feel the effective Lorentz force.

Keywords : Antiferromagnetic Spinor Bose-Einstein condensate, Phase transition, Scaling hypothesis, Spinor quantum turbulence, Topological defects, Composite-soliton, Quantum fluctuations.

Student number : 2012-20353

Contents

Abstract	i
List of Tables	viii
List of Figures	ix
Chapter 1 Introduction	1
1.1 Phase transition dynamics	1
1.1.1 Scaling hypothesis	2
1.1.2 Creation of Topological defects	4
1.2 Spinor Bose-Einstein condensates	7
1.2.1 Scalar vs Spinor BECs	8
1.2.2 Phase diagram of $F = 1$ spinor BEC	11
1.2.3 The manifolds of order parameter of $F = 1$ spinor BEC	14
1.3 Look over quantum phase transition studies in spinor BECs	16
1.4 The outline of the thesis	18
Chapter 2 Spin Manipulation & Imaging	20
2.1 Coil configuration	20
2.2 Magnetic DC & AC fields control	22

2.2.1	Magnetic field calibration	23
2.2.2	Field inhomogeneity control	24
2.3	Microwave dressed fields	29
2.4	Imaging Spinor Bose-Einstein condensates	33
2.4.1	Absorption imaging & Stern-Gerlach imaging	33
2.4.2	Magnetization-sensitive phase contrast imaging	36
Chapter 3 The EAP-to-EPP phase transition		38
3.1	Dynamic instability for the EAP phase	39
3.2	Experimental setup & Methods	42
3.3	Emergence of Spin turbulence	45
3.3.1	Spin-wave excitation	48
3.4	Characterizing the quench dynamics & spin turbulence	48
3.4.1	Time-Space scaling	53
3.5	Spin population relaxation	57
3.6	Topological Defects: Half-quantum vortex	59
3.7	Outlook	60
Chapter 4 The EPP-to-EAP phase transition		63
4.1	Dynamic instability for the EPP phase	65
4.2	Experimental setup & Methods	67
4.3	Characterizing the quench dynamics	69
4.3.1	Measuring the transverse magnon excitation	71
4.3.2	Time-Space scaling	71
4.4	Dynamically formed topological objects	74
4.4.1	Magnetic composite-soliton: a domain wall terminated by HQVs	78

4.5	Suppression of dynamical instability by the axial spin fluctuations	84
4.6	Creation of singly charged vortices	89
4.7	Sad history	90
4.8	Outlook	94
Chapter 5 Rotating Bose-Einstein condensate		95
5.1	Anharmonic trapping potential	96
5.2	Generation of circular c.m. motion	97
5.3	Relaxation of the circulating Bose-Einstein condensate	101
5.3.1	Surface mode excitation	102
5.3.2	Thermal distillation: re-condensation	104
5.3.3	Rotating thermal clouds	109
5.4	Gauge-field effect in a magnetic quadrupole field	112
5.4.1	Skyrmion Spin texture	113
5.4.2	Chirality of Gauge potential	115
5.5	Outlook	118
Chapter 6 Conclusions		119
Bibliography		121
초 록		144
Publication List		147
Appendix A Scaling hypothesis		149
Appendix B Calculation of quantum depletion		151

Appendix C	Examples of SCPI commands	154
Appendix D	Sad history	156

List of Tables

1.1	Scaling of thermodynamic quantities in the thermal equilibrium.	3
1.2	Topological excitations described by the homotopy group.	7
1.3	The order parameter manifold of spinor condensates and their homotopy group.	15

List of Figures

1.1	Schematic phase diagram of the Ising model.	4
1.2	Schematic classification of geometric structures.	5
1.3	Schematic description of Homotopy classes.	6
1.4	Phase diagram of spin-1 Bose gas.	12
1.5	The alignment of the nematic directors in an antiferromagnetic spinor BEC.	15
2.1	Coil configuration around the main chamber.	21
2.2	Rabi oscillation within the hyperfine manifold $F = 1$	24
2.3	Background DC magnetic field calibration using Rabi oscillation.	25
2.4	Calibration of the DC magnetic field inhomogeneity.	26
2.5	Spin dipole oscillation.	28
2.6	Hyperfine structures of $3^2S_{1/2}$ level of ^{23}Na atoms.	30
2.7	Calibration of the quadratic Zeeman shift with the microwave dressed field.	31
2.8	Extract the numbers of BEC and thermal atoms from SG images.	35
2.9	Magnetization-sensitive phase contrast imaging.	37
3.1	Bogoliubov dispersion relations in the EAP phase.	41

3.2	The EAP-to-EPP phase transition for $q/h = -10$ Hz.	46
3.3	The EAP-to-EPP phase transition for $q/h = -5.4$ Hz and $q/h = -20$ Hz.	47
3.4	Spin-wave excitations for $q/h = -1.4$ Hz and $q/h = -2.7$ Hz. . .	49
3.5	Temporal evolution of the EAP-to-EPP phase transition.	50
3.6	The effect of the field gradient on the dynamical instability. . . .	52
3.7	Spin turbulence generation and decay.	54
3.8	Time-Space scaling in the EAP-to-EPP phase transition.	56
3.9	Decay of the fractional $m = 0$ population in the turbulence phase.	58
3.10	Creation of Half-quantum vortex as a result of the EAP-to-EPP phase transition.	59
3.11	The EAP-to-EPP phase transition for $ q /h > 2c_2n$	61
4.1	Bogoliubov dispersion relations in the EAP phase.	66
4.2	Power spectrum of a trapped thermal gas at high temperature. . .	68
4.3	The EPP-to-EAP phase transition for $q/h = 10.4$ Hz.	70
4.4	Temporal evolution of the EPP-to-EAP phase transition.	72
4.5	Spatial scaling of the domain formation for the quenched EPP condensate.	73
4.6	Spin texture of the topological defects with an antiferromagnetic spin interactions.	75
4.7	The formation of magnetic composite-solitons in a quenched EPP condensate.	77
4.8	Dynamically formed topological defects in a quenched EPP condensate.	78
4.9	Schematic of the Bragg spectroscopy and SG imaging sequence.	80

4.10	Bragg spectroscopy and spin separation imaging of a BEC with MCSs.	82
4.11	Singly charged vortices having magnetized cores.	83
4.12	Experimental sequence to enhance spin fluctuations in an EPP condensate.	85
4.13	The EPP-to-EAP phase transition with the spin fluctuations for $q/h = 10.4$ Hz.	86
4.14	Dynamical instability of the quenched EPP condensate with spin fluctuations.	88
4.15	Dynamically formed skyrmions and magnetic composite-solitons in a quenched EPP sample with the spin fluctuations.	89
4.16	Creation of singly charged vortices depending on the number of vacuum fluctuation seed.	91
4.17	The EPP-to-EAP phase transition for $q/h = 2.0$ Hz with slight spin fluctuation.	92
4.18	The EPP-to-EAP phase transition for $q/h = 10.6$ Hz with slight spin fluctuations.	93
5.1	Circulating BEC in an anharmonic hybrid trapping potential.	98
5.2	Generation of a circular c.m. motion of the condensate.	100
5.3	Resonant generation of c.m. motion depending on the modulation time.	101
5.4	Surface mode excitations in the circulating condensate.	103
5.5	Relaxation of the circulating condensate in the anharmonic trapping potential.	105
5.6	Thermal distillation process.	107

5.7	Spinning up the condensate by a rotating thermal cloud.	110
5.8	The evolution of vortex number, total atom number and the thermal fraction of the rotating BEC.	111
5.9	Skyrmion spin texture configuration.	113
5.10	Skyrmion spin texture configuration.	114
5.11	Gauge-field effect.	116
5.12	Generation of c.m. motion under differently polarized external modulation.	117
D.1	Trying to figure out the magnetic field gradient of the grad.z and grad.xy coils	157
D.2	Trying to observe the dynamics of Skyrmion decay.	157

Chapter 1

Introduction

Before we embark on our study-the phase transition dynamics in a spinor Bose-Einstein condensate (spinor BEC) with an antiferromagnetic interaction, we start to introduce why the phase transition dynamics has attracted attentions and what is the uniqueness of an antiferromagnetic spinor Bose-Einstein condensate.

1.1 Phase transition dynamics

The field of the out-of-equilibrium dynamic is diverse in modern many-body physics [1] from the cosmology [2] to condensed matter [3], but our understanding about the nonequilibrium system has been full of questions. This is because the free energy and the probability distribution are hard to defined in this system with, e.g., a time-dependent external driving or energy flows. Many efforts to study of the far-from-equilibrium dynamics have been made by the extension of statistical tools for the thermal equilibrium system. One of the promising achievements is *the scaling hypothesis* near the critical point in the

system relaxing toward a newly ordered state along with symmetry breaking. A quantum quench across the critical point is typical protocol to investigate the phase transition dynamics by suddenly changing the system's Hamiltonian.

1.1.1 Scaling hypothesis

For a continuous phase transition in the thermal equilibrium, the thermodynamic quantities such as an correlation length, an order parameter, free energy, and specific heat of the system have singularities near the critical point and these singularities are usually characterized by a certain power-law scaling exponent, which is well known as *the critical exponents* [4]. These critical exponents are fascinating quantities to classify the systems into *the universal classes*, exemplified by the Ising universality class. Let the relative distance as $q = \frac{Q-Q_c}{Q}$ from the critical point, Q_c , the free energy per particles as f , the magnitude of a symmetry-breaking external field b , and the order parameter ϕ . Then, the f is generalized as

$$f(q, b) = |b|^{2-\alpha} \hat{f}_{\pm}(b/|q|^{\Delta}), \quad (1.1)$$

when $q \rightarrow 0$ and $b \rightarrow 0$, where distinct scaling functions \hat{f}_+ for $q > 0$ and \hat{f}_- for $q < 0$. The scaling behavior of various thermodynamic quantities can be written as in Table 1.1.1. These critical exponents are related each other such as $\alpha + \beta(1 + \delta) = \alpha + 2\beta + \gamma = 2$ and $\gamma = \beta(\delta - 1)$ ¹.

Astonishingly, the critical scaling hypothesis of a thermally static phase transition can be extended to the dynamic scaling hypothesis with the fluctuation-dissipation theorem and the concept of a relaxation time $\tau(q) \sim \xi(q)^z \sim |q|^{-z\nu}$ (reviewed on [5, 6]). The scaling hypothesis in a system far-from-equilibrium

¹Natural question arises: What is the origin of these scalings? The answer is the divergence of the correlation length. Brief introduction is reviewed on Appendix. A.

Quantities	Singular behaviors
Specific heat	$C_{b=0} \sim -(\partial^2 f / \partial q^2)_{b=0} = C_{\pm} q ^{-\alpha}$
Order parameter	$\phi = -(\partial f / \partial q_b) = - q ^{2-\alpha-\Delta} \hat{f}'_-(b/ q ^{\Delta}) \sim \begin{cases} q ^{\beta} & \text{for } b \rightarrow 0 \\ b^{1/\delta} & \text{for } q \rightarrow 0 \end{cases}$
Susceptibility	$\chi_q \sim (\partial \phi / \partial b)_{q,b=0} = \chi_{\pm} q ^{\gamma}$

Table 1.1: Scaling of thermodynamic quantities in the thermal equilibrium.

gives a powerful tool to investigate **how a system evolves into a certain state after the phase transition**, even though it is not fully proved. One of the most well-known classical examples is a coarsening dynamics (or phase-ordering kinetics) [7].

Consider the simple classical phase transition first. Figure 1.1 shows the magnetization as a function of temperature. Suddenly, the temperature change to T_f below the critical temperature T_c and phase separation takes place, evolving into two equilibrium phases with magnetization $\pm M_0$. The locally formed domains subsequently grow and merge through a slow coarsening process as the relaxation time $\tau \rightarrow \infty$ in the vicinity of critical point. The characteristic domain size grows as $L(t) \sim t^{-z}$ according to the scaling hypothesis. Near the critical point, ξ replaces L and $\tau(q) \sim \xi(q)^z \sim |q|^{-z\nu}$. For a quantum phase transition, the situation is similar but the dynamical scaling exponent z is associated with the energy scale $\Delta \sim |q|^{z\nu}$ according to the uncertainty principle.

The scaling hypothesis provides a basis to investigate a phase transition and manifest that the universality is found not only in the thermal equilibrium but also in the far-from-equilibrium systems. In addition, it is supposed that the critical exponents depend only on the dimensionality of the system, d , and the symmetry of the order parameter, and the range of interaction, ξ .

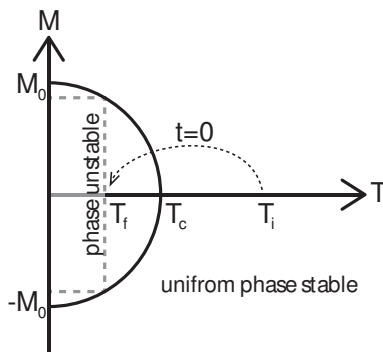


Figure 1.1: Schematic phase diagram of the Ising model depending on temperature without an external field. T_c is the critical temperature. The arrow indicates a temperature quench at time $t = 0$ from T_i to T_f .

1.1.2 Creation of Topological defects

What kind of excitations and how many excitations occurs for the dynamics across the critical point? *The Kibble-Zurek mechanism* begins from these questions and whether the excitation energy depends on the rate of the driving in the quenched system similar to figure 1.1. When Q is close to a quantum critical point, Q_c , the energy gap $\Delta \sim |q|^{z\nu}$ in the spectrum vanishes (or the relaxation time τ diverges in classical manner), leading to the violation of adiabaticity. Kibble first reveal the topological domain formation with the spontaneous symmetry breaking phase transition in the early universe [8,9], and Zurek suggested the analogy between the long-lived cosmology strings in the early universe and the vortex strings in the superfluid Helium [10]. The excitation density of the defects is described by a simple scaling with an assumption of linear change rate. Let the external parameter, in this case temperature, changes as $T = T_c - vt$ with constant velocity v .

This KZ mechanism is generalized to the crossing of a continuous quantum phase transition (reviewed on [11]). The number of topological defects

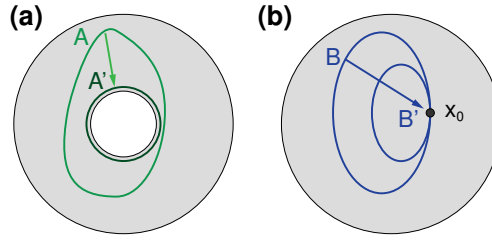


Figure 1.2: Geometric structure can be classified by a set of loop. (a) All loops, A , winding the singular hole of the disk cannot be shrunk to a point continuously. (b) Any kinds of loops, B , can be shrunk into a point, x_0 without distortion.

reflects the length scale of the excitations and the number of the quantum noise seeds.

Classification of topological excitations

The topological excitations have geometrically non-trivial structure, which are invariant under the continuous deformation of the order parameter manifolds, and they are characterized by topological charges. One of the most well-known example is a vortex having an integer phase winding in the $U(1)$ manifold. In other words, when we identify the symmetry of the order parameter manifolds, we can easily predict what kinds of topological excitations are allowed. Firstly, we introduce homotopy group [12, 13].

A loop is a continuous path whose terminal point is identical to the initial point. Every loop can be shrunk to a point without any hole as Fig. 1.2(b). If there exist a hole in a space, the loop of Fig. 1.2(a) cannot be shrunk to a point through the continuous deformation. So, it is very natural that the two spaces in Fig. 1.2 are characterized by a set of loops. In mathematical description, a loop is a continuous map defined as $l : [0, 1] \rightarrow Y$ such as $l(0) = l(1) = x_0$, where Y is a topological space.

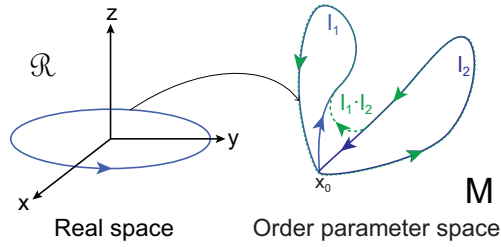


Figure 1.3: Loops l_1 and l_2 mapping from a real space \mathfrak{R} onto the order parameter manifold M . Only mapping of l_1 is described. Green dashed loop also can be the product of l_1 and l_2 .

Let's consider two continuous maps f, g from X to Y , where X and Y are topological spaces. f and g are homotopic equivalent, if the image $f(X)$ is continuously deformed to $g(X)$ in M^2 . The homotopy class of f is denoted as $[f]$. Generally, X is chosen to be well defined topological spaces such as the n -sphere, denoted S^n , where the n -sphere is the generalized $n + 1$ -dimensional surface satisfying $x_1^2 + x_2^2 \cdots x_n^2 = 1$.

Then, we can consider the homotopy classes of loops, $[l_1]$ and $[l_2]$, mapping from a real space \mathfrak{R} to the order parameter manifold M . The product of two homotopy classes is defined as $[l_1] \cdot [l_2] = [l_1 \cdot l_2]$, where $[l_1 \cdot l_2]$ is a homotopy class in which l_1 is traversed and then l_2 is traversed [Fig. 1.3]. With the definition of the product, a set of homotopy classes form a group, called as the first homotopy group, is written as $\pi_1(M, x_0)$ or simply $\pi_1(M)$.

Extends the idea into the higher dimensions. A closed surface in real space \mathfrak{R} is defined with the n -sphere and it is regarded as loops above³. Then,

²Mathematically, f and g are homotopic, if there exist a continuous mapping $F(x, t) : X \times [0, 1] \rightarrow Y$, satisfying $F(x, 0) = f(x)$ and $F(x, 1) = g(x)$. The homotopic equivalent relation satisfies reflexive $f \sim f$, symmetric (if $f \sim g$, then $g \sim f$), and transitive (if $f \sim g$ and $g \sim h$, then $f \sim h$).

³It can be regarded as a map from S^n to a M that a map from an n -dimensional cube $I^n = \{(t_1, t_2, \cdots, t_n) | 0 \leq t_i \leq 1, (1 \leq i \leq n)\}$ to a M whose boundary $\partial I^n = \{(t_1, t_2, \cdots, t_n) | t_i = 0 \text{ or } 1\}$ is shrunk to a base point.

we can consider a group of the homotopy equivalent classes, which consists of the maps from S^n to the manifold, M .

π_n	Defects	Solitons
π_0	Domain walls	Dark solitons
π_1	Vortices	Nonsingular domain walls
π_2	Monopoles	2D Skyrmions
π_3		Skyrmions, Knots
π_4		Instantons

Table 1.2: Topological excitations described by the homotopy group.

The possible topological defects are determined by the n -th homotopy group of the order parameter manifolds. For example, a superfluid system is invariant under the $U(1)$ gauge transformation and $\pi_1(U(1)) \cong \mathbb{Z}$. Therefore, a non-trivial geometrical structure is allowed with the integer winding number - the number of singularities in a loop. The non-trivial topological defect is a quantized vortex line. The homotopy classification of topological excitations is summarized as in Table. 1.2.

1.2 Spinor Bose-Einstein condensates

In case of a many-body quantum system, the generic time-evolution ($|\psi(t)\rangle = \exp^{-iH't/\hbar}|\psi(0)\rangle$) is extremely complicated under the quench through phase transition ($H \rightarrow H'$ at $t = 0$) and the unitary time-evolution in quantum mechanics confuses us not allowing thermalization of a quantum system. Therefore, many experimental attempts have been made. Over the past few years, ultracold atomic systems offered us good experimental platforms with sufficiently long coherent time and the tunability of the system [17] since in 1995 [15, 16], when a BEC was firstly realized. These properties of the ultracold atomic clouds

allow us to contact intriguing physics such as a history of early universe [18]. In this section, we will briefly introduce our experimental platform, spinor Bose-Einstein condensate, one of the ultracold atomic systems possessing the spin degree of freedom.

1.2.1 Scalar vs Spinor BECs

In the limit of zero temperature, the ensemble of dilute and identical bosonic particles forms a new phase, called a Bose-Einstein condensate (BEC), accompanying $U(1)$ symmetry breaking. A BEC can be simply understood by the following description: A particle is usually described by a localized wave packet with its size given by the thermal de Broglie wavelength, $\lambda_{\text{dB}} = \frac{h}{\sqrt{2\pi mk_B T}}$, where h is the Planck's constant, k_B is the Boltzmann constant, and T is the temperature. As temperature lowers toward zero temperature, the spatial extent of atoms increases and eventually λ_{dB} becomes comparable to the inter-particle distance. The wave packets of indistinguishable bosonic particles overlap ending up with a gigantic matter wave of $\Psi(\mathbf{r}_1, \mathbf{r}_2, \dots, \mathbf{r}_N) = \prod_{i=1}^N \psi(\mathbf{r}_i)$, where $\psi(\mathbf{r}_i)$ is a single particle wave function [19]. The formation of macroscopic matter wave begins when phase space density $\lambda_{\text{dB}}^3 \sim 1$. Penrose and Onsager suggested a generalized criterion [20], which is given as

$$\lim_{|x-x'| \rightarrow \infty} \langle \hat{\Psi}^\dagger(x) \hat{\Psi}(x') \rangle = f^*(x) f(x'), \quad (1.2)$$

where $\hat{\Psi}(x) = \psi(x)e^{i\theta}$ is the BEC order parameter, $f(x)$ is a non-zero function. The new thermodynamic properties of Bosons or Fermions can be explained by the off-diagonal long range order of the density matrix [21].

The Hamiltonian of a BEC is given as

$$H = \sum_{i=1}^N \left[-\frac{\hbar^2}{2m} \nabla_i^2 + V_{\text{trap}}(\mathbf{r}_i) \right] + \sum_{i < j} V_{\text{int}}(\mathbf{r}_i - \mathbf{r}_j), \quad (1.3)$$

where V_{trap} and $V_{\text{int}}(\mathbf{r}_i - \mathbf{r}_j)$ is the external potential and the interaction energy between i^{th} and j^{th} atoms, respectively. Because the density of ultracold atoms is extremely dilute, we consider the simplest contact interaction neglecting van der Waals interaction and three-body interaction [22]. In a low energy limit, the two-body interaction is written as

$$V_{\text{int}}(\mathbf{r}_1 - \mathbf{r}_2) = g\delta(\mathbf{r}_1 - \mathbf{r}_2), \quad (1.4)$$

where $g = 4\pi a_s \hbar^2 / m$ is the effective interaction strength and a_s is the s -wave scattering length. The condensate wave function, $\Psi(\mathbf{r}) = \sqrt{N}\psi(\mathbf{r})$, satisfies the Gross-Pitaevskii equation, which is derived from the non-linear Schrödinger equation with the particle number conservation:

$$-\frac{\hbar^2}{2m} \nabla^2 \psi(\mathbf{r}) + V_{\text{ex}}(\mathbf{r})\psi(\mathbf{r}) + g|\psi(\mathbf{r})|^2\psi(\mathbf{r}) = \mu\psi(\mathbf{r}), \quad (1.5)$$

where $\mu = \partial E / \partial N$ is the chemical potential of the system [23].

A single-component BEC is known as a scalar BEC. With the internal hyperfine spin states for neutral atoms, a BEC have an extra spin degree of freedom. Thus, a special multi-component BEC, which consist of the spin components, is called as spinor BEC. In contrast to the conventional multi-component BEC, a spinor BEC allows the spin-exchange collision among the spin states. Spinor BEC shows rich physics with the coupling between the superfluidity and spin ordering. I shall restrict the case of $F = 1$ spinor BEC in my dissertation.

Similar to the dynamics in a scalar BEC, the low energy dynamics in a spinor BEC are also well described by the pairwise-interaction. This contact

interaction preserves the individual atom hyperfine spin and it is invariant under the hyperfine spin rotation [24, 25]. For two indistinguishable spin- \mathbf{F} bosonic particles, the total spin becomes $\mathbf{F}_{\text{tot}} = \mathbf{F}_1 + \mathbf{F}_2$ with $F_{\text{tot}} = 0, \dots, 2F - 1, 2F$. Only the even F_{tot} -channels are allowed, because the statistical symmetry for two identical bosons does not change the spatial wave function⁴ and we only consider the s -wave scattering. Then, the interaction in the Hamiltonian is written as

$$V_{\text{int}}(\mathbf{r}_1 - \mathbf{r}_2) = \delta(\mathbf{r}_1 - \mathbf{r}_2) \sum_{F=0,2} g_F \mathbf{P}_F, \quad (1.6)$$

where $g_F = \frac{4\pi\hbar^2 a_F}{m}$ with a_F is the scattering length for total spin- F channel, and $\mathbf{P}_F = \sum_{m_F} |F_{\text{tot}}, m_F\rangle \langle F_{\text{tot}}, m_F|$ is the projection operator, satisfying the completeness relation of $\mathbf{1} = \sum_{F=0, \text{even}}^{2F} \mathbf{P}_F$. After simple algebra using $\mathbf{F}_1 \cdot \mathbf{F}_2 = \frac{F_{\text{tot}}(F_{\text{tot}}+1) - 2F(F+1)}{2}$, the interaction for spin-1 bosons is given as

$$V_{\text{int}} = \delta(\mathbf{r}_1 - \mathbf{r}_2)(c_0 + c_2 \mathbf{F}_1 \cdot \mathbf{F}_2), \quad (1.7)$$

where the c_0 and c_2 is the spin-independent and the spin-dependent interaction coefficient, respectively, with

$$\begin{aligned} c_0 &= \frac{g_0 + 2g_2}{3} = \frac{4\pi\hbar^2 \bar{a}}{m} \\ c_2 &= \frac{g_2 - g_0}{3} = \frac{4\pi\hbar^2 \Delta a}{m}, \end{aligned} \quad (1.8)$$

and $\bar{a} = \frac{2a_{F=2} + a_{F=0}}{3}$, $\Delta a = \frac{a_{F=2} - a_{F=0}}{3}$ ⁵. Therefore, we find that the total Hamil-

⁴ $(-1)^{2F} = (-1)^{2f} \times (-1)^{F+L}$ should be satisfied for the many-body wave function, where F is the total spin and L is the relative orbital angular momentum of the two identical particles. For the s -wave scattering, $L = 0$.

⁵The spinor system can be described as a multi-spin component mixture of BECs. Then, the interaction between two BECs in hyperfine sublevels m_F and m'_F are characterized as the s -wave scattering lengths of $a_{1,1} = a_{-1,-1} = \bar{a} + \Delta a = a_{F=2}$, and $a_{1,-1} = \bar{a} - \Delta a = \frac{1}{3}(a_{F=2} + 2a_{F=0})$

tonian for a spin-1 spinor BEC is

$$H = \sum_{i=1}^N \left[-\frac{\hbar^2}{2m} \nabla_i^2 + V_{\text{ex}}(\mathbf{r}_i) \right] + \sum_{i<j} \delta(\mathbf{r}_i - \mathbf{r}_j) (c_0 + c_2 \mathbf{F}_i \cdot \mathbf{F}_j). \quad (1.9)$$

The mean field order parameter of the spin-1 spinor BEC is represented by as a three-component order parameter, $\Psi(\mathbf{x}) = \sqrt{n(\mathbf{x})} [\psi_1(\mathbf{x}), \psi_0(\mathbf{x}), \psi_{-1}(\mathbf{x})]^T$, where the magnitude of the vector is normalized. It is not difficult that the order parameter is invariant under the $U(1)$ gauge transformation and the $SO(3)$ spin rotation transformation. The mean field energy functional is given as

$$E = \int d\mathbf{x} \left[\frac{\hbar^2}{2m} |\nabla \Psi|^2 + (V_{\text{ex}}(\mathbf{x}) - \mu) n(\mathbf{x}) + \frac{n^2}{2} (c_0 + c_2 \langle \mathbf{F}^2 \rangle) \right]. \quad (1.10)$$

We can recognize that the spin dynamics in a spinor BEC is determined by the last term of Eqn. 1.10. The ground state of a spin-1 condensate depends on the sign of c_2 : for $c_2 < 0$, ferromagnetic ($|\mathbf{F}| = 1$), exemplified by Rb atoms [27] and antiferromagnetic (or polar, $\mathbf{F} = 0$), exemplified by Na atoms [26] for $c_2 > 0$. The manifolds of order parameters are given by $SO(3)$ for a ferromagnetic and $[U(1) \times S^2]/\mathbb{Z}_2$ for an antiferromagnetic spinor Bose gases, respectively.

1.2.2 Phase diagram of $F = 1$ spinor BEC

With an external magnetic field, the rotational symmetry is broken and the lowest energy level is changed by the Zeeman shift. Simply, consider the system with spatially homogeneous magnetic field of $\mathbf{B} = B\hat{z}$. Then, the Hamiltonian for a spin-1 BEC is given as

$$\begin{aligned} H &= H_{\text{KE}} + V_{\text{trap}} + H_Z + V_{\text{int}} \quad (1.11) \\ &= \int d\mathbf{r} \sum_{m=-1}^1 \hat{\Psi}_m^\dagger(\mathbf{r}) \left[\left(-\frac{\hbar^2 \nabla^2}{2M} \right) + V_{\text{trap}}(\mathbf{r}) + (pm + qm^2) + V_{\text{int}}(\mathbf{r}) \right] \hat{\Psi}_m(\mathbf{r}), \end{aligned}$$

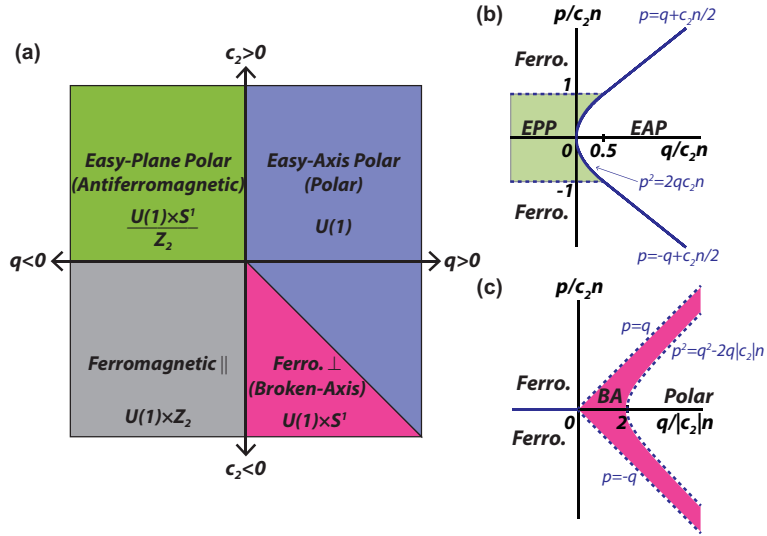


Figure 1.4: (a) Phase diagram for $F=1$ spinor BEC with the external magnetic field based on the mean-field theory from [28]. Ground states for spin-1 BEC with (b) antiferromagnetic ($c_2 > 0$) and (c) ferromagnetic ($c_2 < 0$) s-wave scattering based on the energy per particle [12, 14]. The dotted lines indicate the second-order phase boundaries.

where H_{KE} is the kinetic energy, V_{trap} is the trapping potential, H_Z contains the linear (p) and quadratic (q) Zeeman energies, and V_{int} is the interaction energy of Eqn. 1.6. The strength of the quadratic Zeeman energy is given by $p = g\mu_B B$ and $q = (g\mu_B B)^2/E_{\text{hf}}$, where g_F is the Landé g -factor, and μ_B is the Bohr magneton, and E_{hf} is the hyperfine energy splitting. For sodium, $p = h \times 700 B_0$ kHz/G and $q = (E_{+1} + E_{-1} - 2E_0)/2 \approx h \times 277 B_0^2$ Hz/G², where E_{m_F} is the energy shift of hyperfine sublevel m_F . Then, the total energy functional is expressed as

$$E_S = \int d\mathbf{x} n \left(\frac{c_2 n}{2} \langle \mathbf{F}^2 \rangle + p \langle F_z \rangle + q \langle F_z^2 \rangle \right). \quad (1.12)$$

The ground state obtained by the energy per particle is displayed in Fig. 1.4 (b) and (c) for ferromagnetic and antiferromagnetic spinor BECs, respectively.

Under the magnetization conservation of $M_z = \int d\mathbf{x} n \langle F_z \rangle$, we can write

$\delta E_S - \lambda \delta M_z = 0$ minimizing the quantity $E_S - \lambda M_z$ at fixed λ , where the λ is the Lagrange multiplier, and $\lambda = p$. Thus, we can regard this spinor BEC system in rotating frame with Larmor frequency, and the linear Zeeman energy term is compensated by the magnetization conservation. This means the spin dynamics is affected only by the competition of the spin-dependent interaction, $c_2 n$, and the quadratic Zeeman energy, q .

Figure 1.4 displays the phase diagram for a uniform $F = 1$ spinor BEC in the presence of the external magnetic field based on the mean-field theory. With antiferromagnetic interaction ($c_2 > 0$) corresponding to Na atom case, the atoms are in either the $m_F = 0$ state or the superposition of the $m_F = \pm 1$ states. The former state is called the easy-axis polar (EAP) state and is preferred when $q > 0$. The latter state is called the easy-plane polar (EPP) state, preferred when $q < 0$. The EAP state is effectively same with the scalar BEC, having only $U(1)$ gauge symmetry. On the other hand, for the EPP state, the spin rotation is broken along the z -axis and the EAP has $[U(1) \times S^1]/\mathbb{Z}_2$. In simple description, the ground states for an antiferromagnetic spinor BEC is easily represented by the nematic director, denoted as \mathbf{d} : for the EAP state, $\mathbf{d} \parallel \hat{z}$, and for the EPP state, $\mathbf{d} \perp \hat{z}$, where \hat{z} is the direction of the background magnetic field. \mathbf{d} indicate the $|m_F = 0\rangle$ states along the quantization axis. We will discuss the details of the order parameters and the nematic director in the next section. In case of $c_2 < 0$, a condensate prefers the magnetized states of $m_F = 1$ or $m_F = -1$. Both aligned and anti-aligned states are immiscible. See Ref. [29–33] and reviews [12, 14] if you want to know more about the ferromagnetic spinor BEC system.

1.2.3 The manifolds of order parameter of $F = 1$ spinor BEC

A spin-1 BEC has both superfluidity and the spin degree of freedom. Thus, the full symmetry of a spin-1 BEC is $U(1) \times S^2$. It means that the a general order parameters of a spin-1 BEC is given by

$$\Psi^{\text{Ferro}} = \sqrt{n}e^{i\theta}D(\alpha, \beta, \gamma) \begin{bmatrix} 1 \\ 0 \\ 0 \end{bmatrix} = \sqrt{n}e^{i\theta-\gamma} \begin{bmatrix} e^{-i\alpha} \cos^2 \frac{\beta}{2} \\ \frac{1}{\sqrt{2}} \sin \beta \\ e^{i\alpha} \sin^2 \frac{\beta}{2} \end{bmatrix} \quad (1.13)$$

$$\Psi^{\text{AF}} = \sqrt{n}e^{i\theta}D(\alpha, \beta, \gamma) \begin{bmatrix} 0 \\ 1 \\ 0 \end{bmatrix} = \sqrt{n}e^{i\theta} \begin{bmatrix} -\frac{e^{-i\alpha}}{\sqrt{2}} \sin \beta \\ \cos \beta \\ \frac{e^{i\alpha}}{\sqrt{2}} \sin \beta \end{bmatrix}, \quad (1.14)$$

where $D(\alpha, \beta, \gamma)$ is a rotation operator with Euler angles, α, β , and γ . The order parameter of an antiferromagnetic (or polar) spin-1 BEC does not depend on γ , yielding to the S^1 symmetry around the $\mathbf{d} = (\sin \beta \cos \alpha, \sin \beta \sin \alpha, \cos \beta)$ [see Fig. 1.5]. This \mathbf{d} is the nematic director aforementioned in previous section. The nematic director seems unchanged under the rotation about the x or y -axis. This is because the single-valuedness of Ψ^{AF} is satisfied under the gauge transformation by π ($\theta \rightarrow \theta + \pi$) combined with a spin rotation about the x or y -axis by π ($\mathbf{d} = -\mathbf{d}$). Therefore, the order-parameter manifold of an antiferromagnetic spinor condensate has discrete symmetry of \mathbb{Z}_2 and is given by $[U(1) \times S^2]/\mathbb{Z}_2$ [34].

Topological objects in $F = 1$ spinor BEC

In section 1.1.2, the symmetry of the order parameter determines the types of possible topological excitations. One can easily predict the different topologi-

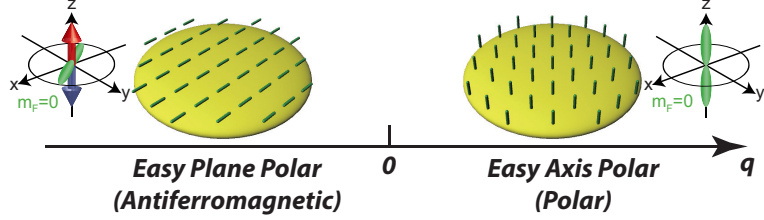


Figure 1.5: The alignment of the nematic directors in an antiferromagnetic spinor BEC based on the mean-field description. Green rods indicate the nematic directors and yellow pancake-shaped object indicate a BEC. For the EPP phase, each nematic director can be randomly aligned in plane.

cal objects are allowed in antiferromagnetic and ferromagnetic spinor BECs. The order parameter manifold of spinor condensates and their homotopy group is displayed in Table 1.2.3. We can predict that there exist singular line structures

	\mathcal{M}	π_1	π_2	π_3
Scalar BEC	$U(1)$	\mathbb{Z}	0	0
Ferromagnetic spin-1 BEC	$SO(3)$	\mathbb{Z}_2	0	\mathbb{Z}
Antiferromagnetic spin-1 BEC	$\frac{S^2 \times U(1)}{\mathbb{Z}_2}$	\mathbb{Z}	\mathbb{Z}	\mathbb{Z}

Table 1.3: The order parameter manifold of spinor condensates and their homotopy group.

from $\pi_1(\mathcal{M}^{\text{AF}}) \cong \mathbb{Z}$, non-singular monopole-like structure from $\pi_3(\mathcal{M}^{\text{AF}}) \cong \mathbb{Z}$, and a Skyrmion-like structure from $\pi_3(\mathcal{M}^{\text{AF}}) \cong \mathbb{Z}$ in an antiferromagnetic spinor BEC. For example, the singular line structure is a quantum vortex, having a half quanta of $h/2M$ ⁶. When $\alpha = \theta = n_{\text{wind}}\phi/2$ and $\beta = \pi/2$, the order parameters

⁶The unit quantization $h/2M$ is half of a circulation for a singly-charged quantum vortex in a scalar BEC.

are written as

$$\Psi^{\text{HQV}} = \sqrt{\frac{n}{2}} \begin{bmatrix} -1 \\ 0 \\ e^{in_{\text{wind}}\phi} \end{bmatrix} = \sqrt{\frac{n}{2}} e^{i\phi_n} \begin{bmatrix} -e^{-i\phi_s} \\ 0 \\ e^{i\phi_s} \end{bmatrix}, \quad (1.15)$$

where n_{wind} is an integer, ϕ_n and ϕ_s are the superfluid phase and spin orientation in the xy -plane, respectively. This is the order parameter of a half-quantum vortex (HQV) confined in xy -plane and $\frac{\phi_n \pm \phi_s}{2\pi}$ should be integer because of the single-valuedness of order parameter⁷. HQVs are unique and energetically stable structures for an antiferromagnetic spinor condensate, allowed by the discrete \mathbb{Z}_2 symmetry [35, 41]. Hedgehogs, Dirac monopoles, Shanker Skyrmions, and quantum knots can also be created in a spin-1 BEC with antiferromagnetic interaction. A hedgehog is energetically unstable and deformed into an Alice ring [42]. Dirac monopoles [36, 37] and quantum knots [38] are created based on the theoretical suggestions [39, 40].

In 2-dimensional antiferromagnetic spinor condensate, which we have typically performed our experiments, we observe 2D Skyrmion [43], and half-quantum vortices [41, 44], experimentally.

1.3 Look over quantum phase transition studies in spinor BECs

Based on the theoretical suggestions [24], the ground state of a Na spinor condensate and its metastability were first investigated in 1998 [26], and the

⁷In simple description, only one spin component either $m_F = 1$ or $m_F = -1$ has a circulation and other component is stationary.

ground state of a Rb BEC were observed in 2004 [27]. Since then, various spin dynamics arising under rapid quantum phase transition has been investigated.

Quantum phase transition dynamics arises due to the amplification of the vacuum fluctuations. The excitations of spin modes has been observed in small condensates, where all spin states are regarded to have identical spatial dependence [45, 46]. This assumption is known as the single-mode approximation (SMA) and one can ignore the spatial variance of wave function. The phase diagram of spin-1 Na condensate with finite magnetization has been experimentally studied under SMA [47]. The amplification of the spin fluctuations in one-direction reduces the uncertainty of the spin fluctuations in other-direction, which is an example of spin-squeezing phenomena. This spin-squeezing is measured with the quenched spinor BEC [48].

For a condensate larger than the spin healing length, the spin dynamics accompanies spatial variance beyond the SMA. In 2006, the spin-domain coarsening dynamics and polar-core vortices were observed in a quenched ferromagnetic spin-1 condensate through the polar-to-BA phase transition [49], and by extending this experiments, the vacuum fluctuations has been measured in terms of the dependence of the quench depth [50]. After microwave dressing technique has been developed [51], the deeper transition dynamics from the polar phase to the ferromagnetic phase [52] has been conducted by changing the quadratic Zeeman energy to negative. In case of an antiferromagnetic spinor condensate, the instability rate and the spatial ordering has been measured in quenched 1D spinor condensates with $F = 2$ Rb [53] atoms and with $F = 1$ Na atoms [54–56]. Recent researches on the quenched spinor BECs have been extended to a spinor BEC in an optical lattice [57, 58]. Using the methods of optical lattice shaking or tuning the contact interaction by Feshbach resonance,

the spin-domain coarsening dynamics has been measured with the pseudo-spin states in terms of the universal scaling and its exponents [59–61].

In our experiments with a Na BECs, we focus on how the intrinsic time-space scaling of the initial dynamics near the critical point is inherited and transformed in the subsequent evolutions. In addition, we explore what kinds of topological excitations are created during the phase transition dynamics in spin-wise 2D condensate.

1.4 The outline of the thesis

This thesis is organized as follows. In chapter 2, the methods of spin order manipulation are introduced, including the apparatus to control background magnetic fields.

Chapter 3 focuses on the spin turbulence generation and decay in a quenched spinor Bose-Einstein condensate through the easy-axis polar phase to the easy-plane polar phase transition (the EAP-to-EPP phase transition) in terms of the scaling on the quench depth, the quadratic Zeeman energy. After reviewing the Bogoliubov dispersion relations in the EAP phase, the spin-wave excitation and the emergence of spin turbulence are described. Interestingly, the late-time dynamics beyond the mean-field description shows the same scaling behavior with the dynamics in the early stage. When the spin turbulence decays, half-quantum vortices can be identified.

In case of the easy-plane polar phase to the easy-axis polar phase transition (the EPP-to-EAP phase transition), the initial dynamics also depends on the quadratic Zeeman energy. Without any spin fluctuations, the quenched EPP condensate coherently recovers its first state once. Then, the system evolves in

complex way. When the EPP condensate is prepared to have the spin fluctuations via the gapless magnon excitation, the coherent oscillation disappears. In addition, the instability rate of the quench dynamics is affected by the amplitude of the spin fluctuations. In the complex evolution stage, solitons terminated by half-quantum vortices (HQVs) are identified. We investigate the unique soliton by measuring the mass flow around the endpoint and its spin textures. For a long hold time, singly charged vortices are created as a result of the EPP-to-EAP phase transition. This results are introduced and discussed in chapter 4.

Chapter 5 describes the simple method to create vortex lattice in the rotating Bose-Einstein condensate (BEC) with the anharmonicity of the trapping potential. The transferring procedure from the circular center-of-mass motion of BEC to the angular momentum of the BEC is studied. Then, the chirality of the gauge potential, which is induced by the Skyrmion spin texture, is measured with this rotating methods.

Finally, in chapter 6, the conclusions and the future outlooks are discussed.

Chapter 2

Spin Manipulation & Imaging

Various coil pairs are needed for performing spinor condensate experiments, especially for controlling the magnitude, orientation, and inhomogeneity of background magnetic fields. Most of techniques are also discussed on S.W. Seo's thesis.

2.1 Coil configuration

Throughout the thesis, we define the x , y , and z -axes as described in Fig. 2.1. Following this convention, there exist the 3 Helmholtz coil pairs constructed around the main chamber in x , y , and z -directions for compensation of the magnetic field of the Earth. We call these coil pairs as comp.x, comp.y, and comp.z coils each. The comp.z coils generate ~ 0.7 G/V and ~ 1.1 A/V.

On the top and bottom of the main chamber, we build 4 coil pairs of the Feshbach coils for producing $F = 2$ Na and performing Li experiments, the quadrupole coil pairs for magneto-optical trap (MOT) and magnetic trap, the bias coil pairs for controlling z -directional bias magnetic field, and the grad.z

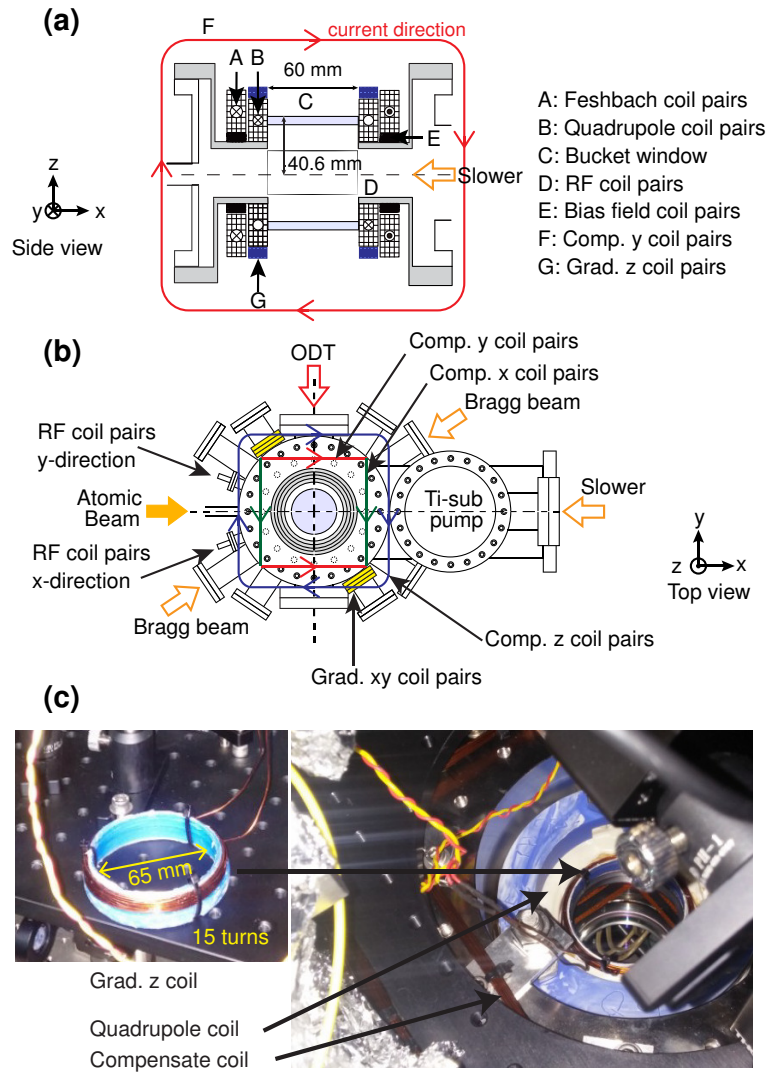


Figure 2.1: (a) Side and (b) top view of coils around the main chamber. Recessed bucket windows allow us to implant various coils close to the main chamber. A blue colored pair of anti-Helmholtz coils is placed on the top and the bottom, and another yellow colored pair of anti-Helmholtz coils is placed in the front and the rear of the main chamber to reduce the DC magnetic field gradient. We name these coils as the gradient z - and xy -coils, respectively. Two pairs of Helmholtz coil pairs are placed inside the chamber, connected to the two electrical feed through the port, which are named as radio-frequency coil pairs. (c) A photo of the 15-turn gradient z -coil on the top of the main chamber. The gradient z -coils are fixed on the plastic frame with non-magnetic epoxy. The original figure of coil configuration is adopted from J. Choi's publications [62, 63] and S.W. Seo's thesis [64]

coil pairs for canceling out the residual magnetic field gradient. The Feschbach coils generate 4.3 G/V and the quadrupole coils generates field gradient of 1.5 G/(cm A) along the z -axis. The grad. z coil pairs are anti-Helmholtz coil pairs wound by 15 turns with circular nonmagnetic frame [Fig. 2.1 (c)] and generate 33 mG/(cm A) and 17 mG/(cm A) along the z - and residual directions. Another anti-Helmholtz coil pairs to cancel out the magnetic field gradient are wound along the xy -direction (yellow coil pairs), which named as grad. xy coils.

Radio-frequency evaporation coils are placed inside the chamber, which are called as x -directional RF coils (shortly RF coils). These RF coil pairs are also used for spin manipulation within the hyperfine manifold $F = 1$. In the y -direction, there exist another Helmholtz coils are placed for AC field generation and used for microwave dressing technique. These y -directional RF coils are usually called as microwave coils.

2.2 Magnetic DC & AC fields control

No matter how well we build the coil configurations, it is not possible to control magnetic fields uniformly. Thus, the magnetic fields is expanded as

$$\vec{B} = \begin{bmatrix} B_{0,x} \\ B_{0,y} \\ B_{0,z} \end{bmatrix} + \begin{bmatrix} B_{xx} & B_{xy} & B_{xz} \\ B_{yx} & B_{yy} & B_{yz} \\ B_{zx} & B_{zy} & B_{zz} \end{bmatrix} \begin{bmatrix} x \\ y \\ z \end{bmatrix}, \text{ where } B_{ij} = \hat{x}_i \cdot \frac{\partial \vec{B}}{\partial x_j}. \quad (2.1)$$

Maxwell's equation requires $\nabla \cdot \vec{B} = 0$ and $\nabla \times \vec{B} = 0$, yielding $\sum_{i=x,y,z} B_{ii} = 0$ and $B_{ij} = B_{ji}$. In our experiment, the spin dynamics is freezed in z -direction ($R_z \ll \xi_s$) and we ignore the z -directional field gradient. Without loss of generality, let the magnetic field is oriented in plane such as $B_{0,y} = B_{0,z} = 0$ and $B_{0,x} = B_0$.

For $B_0 \gg B_{ij}x_j$, Eqn. 2.1 is simplified as

$$\begin{aligned} |\vec{B}| &= \sqrt{(B_0 + B_{xy}y + B_{xz}z)^2 + (B_{yx}x + B_{yz}z)^2 + (B_{zx}x + B_{zy}y)^2} \quad (2.2) \\ &\approx B_{0,x} + B_{xx}x + B_{xy}y + O\left(\left(\frac{B_{ij}x_j}{B_0}\right)^2\right). \end{aligned}$$

Firstly, we calibrate the DC and AC magnetic fields. Then, we discuss the methods to measure the field inhomogeneity and how we remove the field gradients.

2.2.1 Magnetic field calibration

The calibration of the magnetic fields is done by measuring the Rabi oscillation. Typically, Na BEC is prepared in the $|F = 1, m_F = -1\rangle$ state [Fig. 2.2.1(a)]. When we apply an oscillating electromagnetic field at a constant amplitude, atoms are transmuted into the other hyperfine sublevels in time. Consider a three level atomic system with the DC magnetic field, $B\hat{z}$, and AC field, $B_0 \cos(\omega t)\hat{x}$. In the rotating wave approximation, the dressed-state Hamiltonian is expressed as

$$\hbar \begin{pmatrix} -\delta & \Omega/\sqrt{2} & 0 \\ \Omega/\sqrt{2} & q & \Omega/\sqrt{2} \\ 0 & \Omega/\sqrt{2} & \delta \end{pmatrix}, \quad (2.3)$$

where $\hbar\delta = \hbar(\omega - \omega_0)$, $\hbar\omega_0 = \frac{1}{2}\mu_B|B|$, q is the quadratic Zeeman energy, and $\hbar\Omega = \frac{1}{2}\mu_B|B_0|$ is the Rabi frequency.

Approximately, above the three-level system can be regarded as the two-level system with effective Rabi frequency, $\Omega_{\text{eff}} = \sqrt{\Omega^2 + \delta^2}$. Ω_{eff} is extracted from the temporal evolution of populations. For example, the number of the $m_F = -1$ component oscillates as $N_{-1} \propto (1 - \cos(\Omega_{\text{eff}}t))$. To precisely calibrate the background magnetic fields, one should find the minimum Ω_{eff} [32]. However,

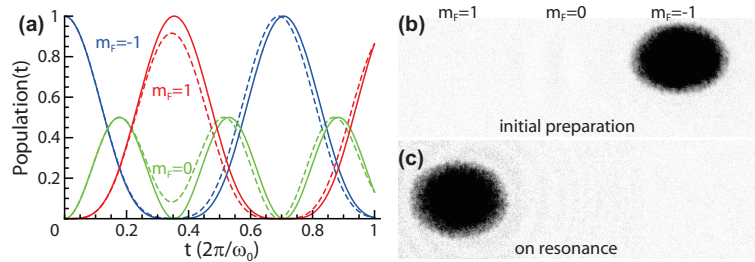


Figure 2.2: (a) Rabi oscillation within the hyperfine manifold $F = 1$ with (b) initial state, $(\rho_1, \rho_0, \rho_{-1}) = (0, 0, 1)$. Red, green, and blue lines represent the populations of $m_F = 1, 0,$ and -1 , respectively. We set the resonant Rabi frequency as $\Omega = \sqrt{2}\omega_0$. The solid and dashed lines display resonant and off-resonant ($\delta = 0.3\omega_0$) oscillations, respectively. (c) A BEC image with resonant π -pulse.

atoms are perfectly transferred into the $|F = 1, m_F = 1\rangle$ state from the $|F = 1, m_F = -1\rangle$ state for π -pulse only on resonance [Fig. 2.2.1(b,c)]¹.

We calibrated the background magnetic fields along the y, z -axes on August 2017, displayed in Fig. 2.2.1 by applying the x -directional AC field (See Fig. 2.1): 0.72 G/V along the y -axis and 0.67 G/V along the z -axis². The background magnetic fields become 0 V at Word Generator voltage of 0.15 V and 5.01 V in y - and z -directions, respectively.

2.2.2 Field inhomogeneity control

Calibrating the magnetic field gradient

The Ramsey interferometry allow us to precisely measure relative phase from the magnetic resonance by interfering two-separately evolved interacting

¹When you prepare atoms in the $|F = 1, m_F = 0\rangle$ state and apply $\pi/2$ rf pulse, 100% of the population can be transferred into the superposition of the $|F = 1, m_F = \pm 1\rangle$ with the off-resonant frequency.

²For $F = 1$ sodium, the Larmor frequency is $\omega_L = g_F \mu_B |\vec{B}|/\hbar = 2\pi \times 0.70 \text{ MHz/G} \times |\vec{B}|$.

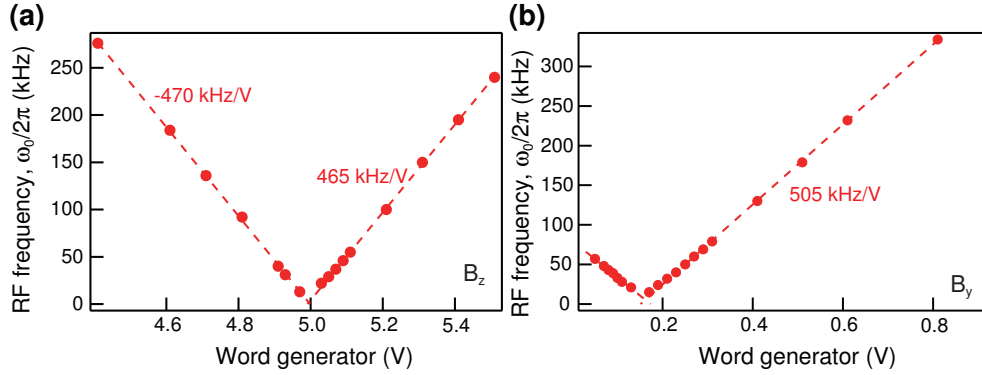


Figure 2.3: Background DC magnetic field calibration using Rabi oscillation along (a) the y-direction and (b) z-direction.

zones, and we use the method to calibrate the DC magnetic field inhomogeneity [65, 66]. Figure 2.2.2(a) displays the Ramsey interferometry sequence. The states of atoms are illustrated with the nematic director, \mathbf{d} .

Atoms are prepared in the $|F = 1, m_F = 0\rangle$ state by using the Landau-Zener sweep sequence³ [29, 64] and the state is written as $\vec{\zeta}_i = [\zeta_1, \zeta_0, \zeta_{-1}]^T = [0, 1, 0]^T$. At this time, \mathbf{d} aligns to z -axis (either $\pm\hat{z}$ direction). A $\pi/2$ pulse rotates the nematic director around y -axis and the atoms are in the $\frac{1}{\sqrt{2}}[1, 0, 1]^T$ states. The nematic director freely evolve for a time τ with an Larmor frequency $\omega_L = g_F\mu_B B/\hbar$. Because the magnetic field, $B(\mathbf{r})$, varies in space, the atoms have position-dependent phases of $\phi(\mathbf{r})$ s and the atomic states are given as $\frac{1}{\sqrt{2}}[1, 0, e^{i\phi(\mathbf{r})}]^T$. Finally, we apply $\pi/2$ pulse and atoms in the $|F = 1, m_F = \pm 1\rangle$ states interfere [Fig. 2.2.2(b)].

You can easily estimate the number of fringe patterns $\sim \frac{\omega_L}{2\pi}\tau \frac{dB_y}{dy} (2R_y)$ from $\delta\phi \propto \omega_L\tau \propto \frac{dB_y}{dy}y\tau$, when the patterns aligned in the y -direction, because the phase changes 2π across the nearest two density-holes (or density-peaks).

³From Eqn. 2.3, the avoided crossings occur at $\delta \approx \pm q$ and $\delta = 0$ with $\Omega_{-1,0} = \hbar\Omega\sqrt{2}$ and $\Omega_{-1,1} = \hbar\Omega^2/q$, respectively.

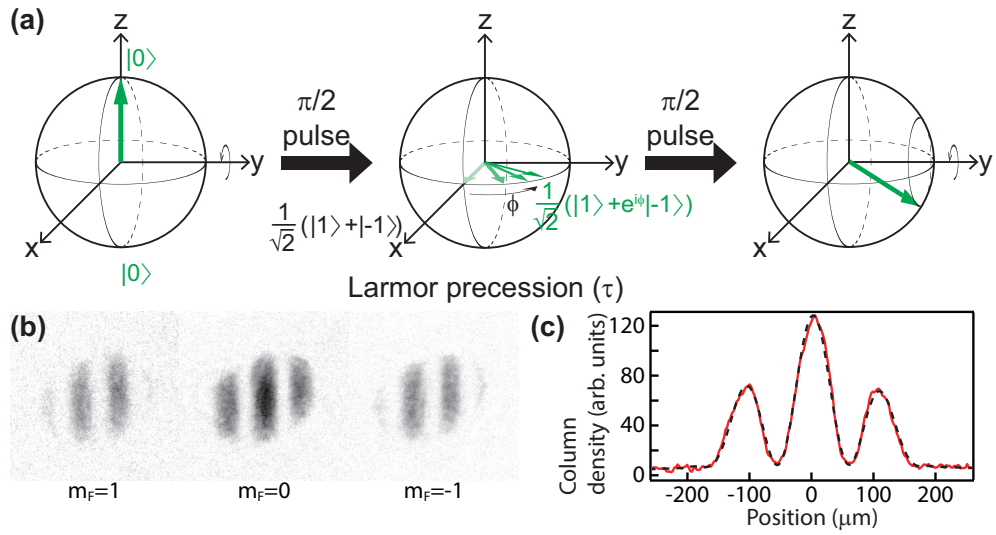


Figure 2.4: Calibration of the DC magnetic field inhomogeneity. (a) Schematic diagram of a Ramsey interferometry. Spin evolution is displayed on the Bloch Sphere. The green arrows indicate the nematic directors. (b) Ramsey fringe pattern with $\tau = 10$ ms and $B' = 6.2$ mG/cm. (c) The red solid line is the 1D column density of $m_F = 0$ spin component in (b). The blue dashed line is the fitting curve by Eqn. 2.6.

Using the matrix algebra, consider a rotation operator $D(\alpha, \beta, \gamma)$, where α , β , and γ are the Euler angles [67]. Then, $\pi/2$ rotation is described as $D_{\pi/2} \equiv D(\alpha = 0, \beta = \pi/2, \gamma = 0)$ such as

$$D_{\pi/2} = \begin{bmatrix} \frac{1}{2}(1 + \cos \beta) & -\frac{1}{\sqrt{2}} \sin \beta & \frac{1}{2}(1 - \cos \beta) \\ \frac{1}{\sqrt{2}} \sin \beta & \cos \beta & -\frac{1}{\sqrt{2}} \sin \beta \\ \frac{1}{2}(1 - \cos \beta) & \frac{1}{\sqrt{2}} \sin \beta & \frac{1}{2}(1 + \cos \beta) \end{bmatrix}_{\beta=\pi/2}, \quad (2.4)$$

and the Larmor precession during τ is given as $D(\alpha = \phi(\mathbf{r}), \beta = 0, \gamma = 0)$ whose matrix elements are $D(\phi, 0, 0)_{m_F, m'_F} = \exp(-im_F \phi(\mathbf{r})) \delta_{m_F, m'_F}$ with $\phi = g_F \mu_B (B_0 + B'y) \tau / \hbar$. For the initial $\vec{\zeta}_i = [0, 1, 0]^T$ state, the atomic density as a result of the Ramsey interferometry is

$$|\vec{\zeta}_f| = |D_{\pi/2} D(\phi, 0, 0) D_{\pi/2}|^2 = \begin{bmatrix} \frac{1}{2} \sin^2(\phi_0 + g_F \mu_B B' y \tau \hbar) \\ \cos^2(\phi_0 + g_F \mu_B B' y \tau \hbar) \\ \frac{1}{2} \sin^2(\phi_0 + g_F \mu_B B' y \tau \hbar) \end{bmatrix}, \quad (2.5)$$

where $\phi_0 = (g_F \mu_B B_0) \tau / \hbar$. The condensate is captured in the harmonic optical dipole trapping potential. Thus, the density profile of the Ramsey fringe is given as

$$\begin{aligned} \tilde{n}_{1D}(x, y) &\sim \cos^2(\phi_0 + g_F \mu_B B' y \tau \hbar) \times \left(1 - \left(\frac{x}{R_x}\right)^2\right)^2 \quad \text{and} \quad (2.6) \\ \tilde{n}_{2D}(x, y) &\sim \cos^2 \phi(x, y) \times \left(1 - \left(\frac{x}{R_x}\right)^2 - \left(\frac{y}{R_y}\right)^2\right)^{3/2}, \end{aligned}$$

in case of 1D and 2D, respectively. An example of the gradient calibration is displayed in Fig. 2.2.2.

Cancelling out the magnetic field gradient

Using the grad.z and grad.xy coil pairs, we cancel out the field gradient according to Eqn. 2.2. Ironically or luckily, the quadrupole zero-field points of

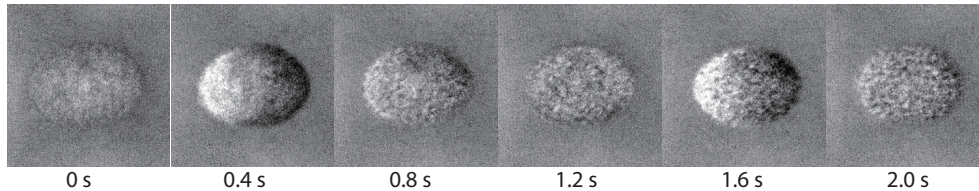


Figure 2.5: Dipole oscillation of an EPP condensate in the harmonic optical dipole trapping potential induced by $B' < 0.5$ mG/cm.

the grad.z and grad.xy coil pairs are not placed the exact the center of the coils, which allow us to remove the magnetic field gradient⁴.

With the Ramsey method, it is not able to measure the extremely small field inhomogeneity less than 0.3 mG/cm due to the limitation of $\tau \leq 100$ ms. In our experiment, spin-dependent interaction is ~ 10 Hz and unwanted spin dynamics is possible to come in for long Larmor precessing time over 100 ms. Therefore, we use spin-dipole oscillation [68, 69] to remove the magnetic field gradient more completely. Figure 2.2.2 shows the spin-dipole oscillation with the frequency of $\omega_{\text{SD}} \approx 2\pi \times 0.8 \approx 0.2\omega_x$ [69] under the field gradient $B' < 0.5$ mG/cm. We can confirm that the field gradient is removed, when there is no spin-dipole oscillation and the $m_F = \pm 1$ condensates completely overlap at 600 ms.

Another way to calibrate the field gradient is measuring the dynamical instability via the EAP-to-EPP phase transition. For low magnitude of $|q|$, the influence of the field gradient is great [56]. We confirm this experimentally [Fig. 3.4].

⁴The position quadrupole zero-field point can be adjust by the changing the bias fields. We were trying to figure out the magnetic field gradient generated by the grad.z and grad.xy coils. But, before that, we empirically cancel out the field inhomogeneity by tuning the bias field and controlling the currents of both anti-Helmholtz coils (Appendix. D).

2.3 Microwave dressed fields

The hyperfine sublevels of a spin- F atom split due to the linear and quadratic Zeeman energies (Eqn. 1.11). The competition of the linear and quadratic Zeeman energies allow many researchers to investigate various spinor dynamics such as spin-mixing dynamics-quantum pendulum [70]- and phase transition dynamics [45–47, 49, 50]. In a DC magnetic field, q is typically positive. Thanks to the microwave dressing technique, one can contact negative q region. According to the Breit-Rabi formula [71], the energy for each sublevels is given as

$$E_{F,m_F} = \frac{E_{\text{hf}}}{2(2I+1)} - g_I \mu_B m_F B + (-1)^F \frac{E_{\text{hf}}}{2} \sqrt{1 + \frac{4m_F \alpha}{2I+1} + \alpha^2}, \quad (2.7)$$

where $\alpha = \frac{g_J \mu_B - g_I \mu_I}{E_{\text{hf}} B}$, E_{hf} is the hyperfine splitting, and g_I , g_J are the Landé g-factors for a nuclear and a valence electron, respectively. From Eqn. 2.7, we can get

$$q_{\text{DC}} = \frac{E_{1,1} + E_{1,-1} - 2E_{1,0}}{2} \approx \frac{(g_J \mu_B - g_I \mu_I)^2}{16E_{\text{hf}}} \times B^2, \quad (2.8)$$

ignoring higher orders. Under a DC magnetic field, q is typically positive. Thanks to the microwave dressing technique, one can contact negative q region.

The microwave dressing technique use the AC stark effect. Consider the simplest system consists of the ground state $|g\rangle$ and the excited state $|e\rangle$. When we apply an AC field with an magnetic field magnitude $|\vec{B}|$ and frequency, detuned by δ from the resonance frequency, we have the dressed-Hamiltonian,

$$H_{\text{D}} = \frac{\hbar}{2} \begin{pmatrix} \delta & -i\Omega \\ i\Omega & -\delta \end{pmatrix}, \quad (2.9)$$

where $\vec{\mu}$ is a magnetic moment of the atom, and $\Omega = |\vec{\mu} \cdot \vec{B}|/\hbar$ is the Rabi frequency. Then, according to the 2nd-order perturbation theory, the energy of

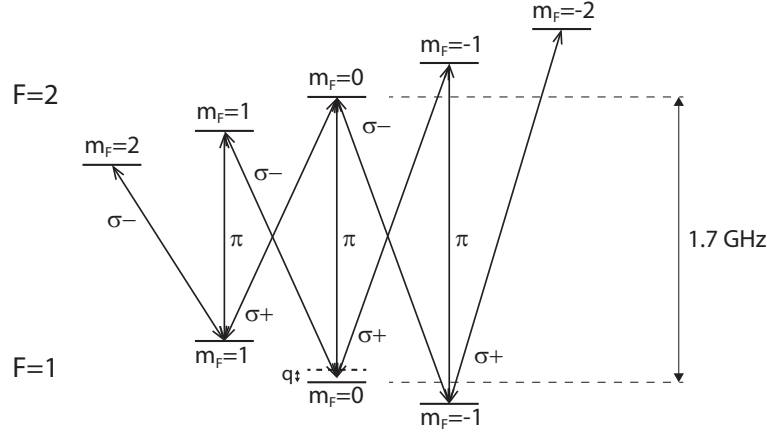


Figure 2.6: Hyperfine structures of $3^2S_{1/2}$ level of ^{23}Na atoms with an external magnetic field. The magnetic sublevels of $F = 1$ and $F = 2$ states split by the linear Zeeman shift. Allowed transitions depends on the polarization of an AC fields. The dotted level is the energy of $(E_1 + E_{-1})/2$. Energy is not scaled.

$|g\rangle$ is shifted as

$$\delta E = \frac{|\langle e | -\vec{\mu} \cdot \vec{B} | g \rangle|^2}{E_e - E_g} = \frac{\hbar \Omega^2}{4\delta}, \quad (2.10)$$

where $\vec{\mu}$ is a magnetic moment of the atom.

Expands above idea to Na atoms with $F = 1$ and $F = 2$ hyperfine states. Let a microwave dressing field $V_\mu = -\vec{\mu} \cdot \vec{B}_\mu \cos(\omega_\mu t) = \frac{1}{\hbar} g_F \mu_B \vec{F} \cdot \vec{B}_\mu \cos(\omega_\mu t)$. Applying the 2nd-order perturbation, the energy shift is derived as

$$\begin{aligned} \delta E_{m_F} &= \sum_{m'_F} \frac{|\langle F = 2, m'_F | V_\mu | F = 1, m_F \rangle|^2}{E_{m'_F} - E_{m_F}} \\ &= \frac{\hbar}{4} \sum_{m'_F} \frac{\Omega_{m_F, m'_F}^2}{\delta_{m_F, m'_F}}, \end{aligned} \quad (2.11)$$

where Ω_{m_F, m'_F} s are the Rabi frequencies between $|F = 1, m_F\rangle$ and $|F = 2, m'_F\rangle$ and δ_{m_F, m'_F} is the detuning from the $|F = 1, m_F\rangle \leftrightarrow |F = 2, m'_F\rangle$ transition. The Rabi frequency Ω_{m_F, m'_F} is usually determined by the intensity of the microwave

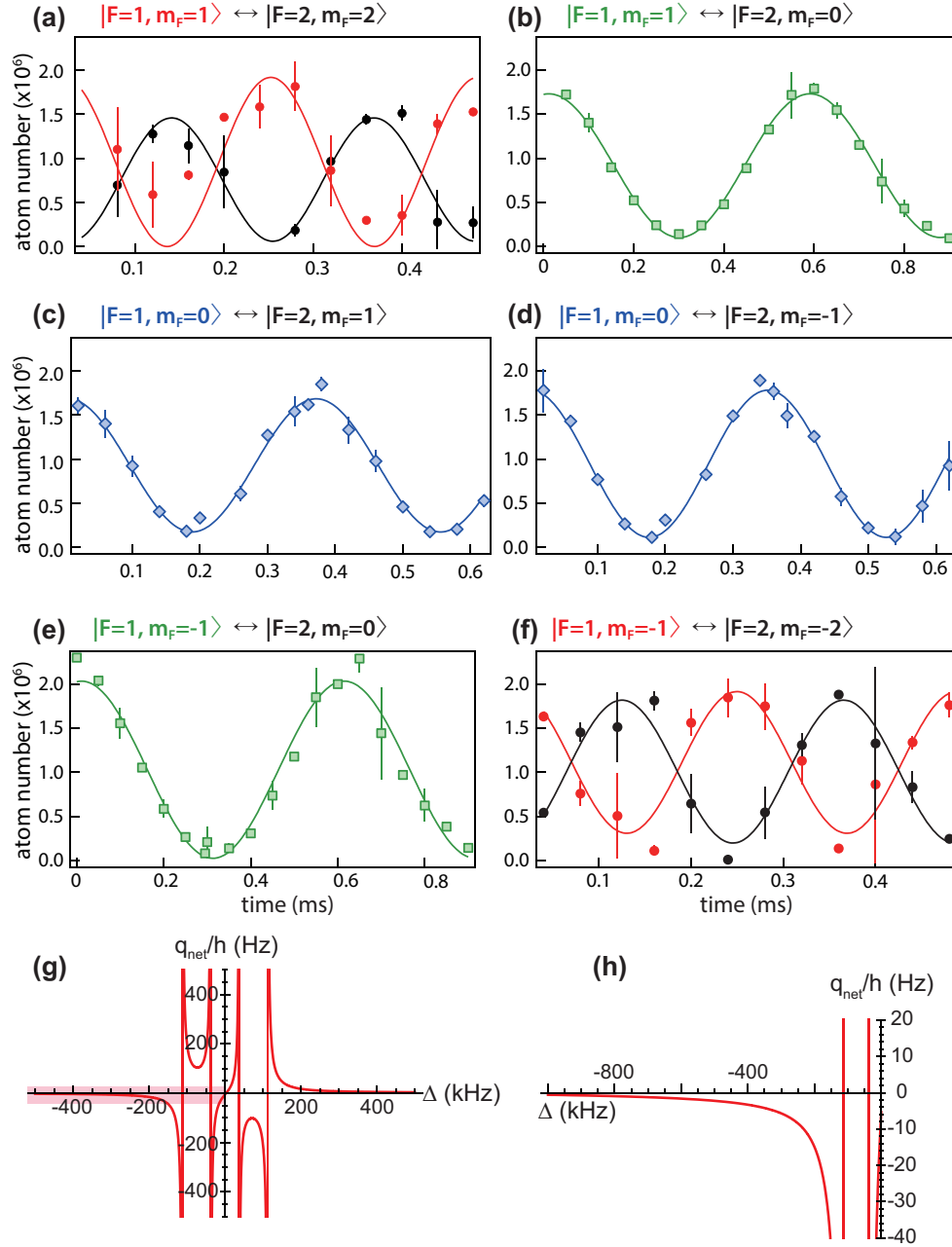


Figure 2.7: Rabi oscillations of $|F = 1\rangle \leftrightarrow |F = 2\rangle$ transition. The measured Rabi frequencies, Ω_{m_F, m'_F} are (a) 4.3 kHz, (b, e) 1.7 kHz, (c) 2.7 kHz, (d) 2.8 kHz, and (f) 4.2 kHz. (g) Calibrated quadratic Zeeman shift with above Ω_{m_F, m'_F} with 52 mG background DC field. (h) is the enlarged graph of the shaded area in (g).

pulse and the transition strength, which is represented by Clebsch-Gordan coefficient. As illustrated in Fig. 2.3, the polarization of the microwave field allows a certain transition of $|F = 1, m_F\rangle \leftrightarrow |F = 2, m_F + k\rangle$, where $k = 0$ and ± 1 for the π and σ^\pm -polarized microwave fields, respectively. The detuning δ_{m_F, m'_F} is expressed as

$$\begin{aligned}\delta_{m_F, m_F+k} &= \omega_\mu - \omega_{m_F, m_F+k} \\ &= \omega_\mu - \left[\omega_{0,0} + \frac{1}{2}[(m_F + k) - (-m_F)] \frac{g_F \mu_B B}{\hbar} \right] \\ &= \Delta - \frac{1}{2}[(m_F + k) - (-m_F)] \frac{g_F \mu_B B}{\hbar},\end{aligned}\tag{2.12}$$

where ω_{m_F, m'_F} is the resonance frequency between $|F = 1, m_F\rangle$ and $|F = 2, m'_F\rangle$ states, which can be estimated from Eqn. 2.7 as $\omega_{m_F, m'_F} = (E_{2, m'_F} - E_{1, m_F})/\hbar$. With simple calculation, the resultant quadratic Zeeman energy is given as

$$\begin{aligned}q_{\text{net}} &= q_{\text{DC}} + q_\mu \\ &= q_{\text{DC}} + \frac{\delta E_1 + \delta E_{-1} - 2\delta E_0}{2},\end{aligned}\tag{2.13}$$

$$\text{where } \delta E_{m_F} = \frac{\hbar}{4} \sum \frac{\Omega_{m_F, m_F+k}^2}{\Delta - [(m_F + k)/2 - (-m_F/2)] g_F \mu_B B / \hbar},\tag{2.14}$$

and $q_{\text{DC}} \approx hB^2 \times 277 \text{ GHz/G}^2$ for Na atoms.

We measure the Rabi frequencies, Ω_{m_F, m'_F} , by using circularly polarized microwave, which is equally mixed both σ^\pm , with frequency of 1.7 GHz. Figure 2.3 displays the q_{net} as a function of Δ .

We tune q_{net} with 0.5 Hz accuracy by using this microwave dressing technique. However, as ω_μ close to the resonant frequency, the lifetime of the condensate becomes shorter. This is because that the lifetime of $F = 2$ atoms are much shorter than $F = 1$ atoms. In addition, the coupling strength between $|F = 1, m_F = -1(+1)\rangle$ and $|F = 2, m_F\rangle$ is larger than that between

$|F = 1, m_F = +1(-1)\rangle$ and $|F = 2, m_F\rangle$ for negative(positive) detuning from the on-resonant frequency, leading to the higher $m_F = -1(+1)$ atom loss (see Fig. 3.9(f)).

2.4 Imaging Spinor Bose-Einstein condensates

We generally measure the spin dynamics appearing in quenched spinor condensate by the absorption imaging after a short spin separation and magnetization-sensitive phase contrast imaging (in short, magnetization imaging) in z -direction. In this section, we shall briefly introduce these methods.

2.4.1 Absorption imaging & Stern-Gerlach imaging

Absorption imaging is one of the easiest imaging techniques to experimentally implement and interpret the signal]s with high signal-to-ratio, because it uses resonant light to the atomic transition line. When the probing beam passes trough a BEC, the intensity of the beam is reduced by the absorption of an atom. With atomic density of n and the resonant scattering cross section $\sigma = \lambda^2/2\pi$, the imaging beam is attenuated as

$$\frac{dI}{dx} = -\sigma nI, \quad (2.15)$$

where λ is the wavelength of imaging beam and I is the intensity of the beam. Therefore, we can obtain the density information of a BEC from $n(\mathbf{r}) = -\frac{1}{\sigma} \ln(I/I_0)$.

In reality, an absorption image is taken onto the camera, containing

$$I_{\text{img}}(\mathbf{r}) = I_0(\mathbf{r})e^{-\sigma n(\mathbf{r})} + S(\mathbf{r}) + N(\mathbf{r}), \quad (2.16)$$

where $S(\mathbf{r})$ is the photon-shot noise and $N(\mathbf{r})$ represents other unwanted noises. In order to remove the noises, we additionally take a bright probing beam image without any atoms (I_{beam}) and a dark-field image (I_{dark}) without any lights:

$$I_{\text{beam}}(\mathbf{r}) = I_0(\mathbf{r}) + S(\mathbf{r}) + N(\mathbf{r}), \quad (2.17)$$

$$I_{\text{dark}}(\mathbf{r}) = N(\mathbf{r}). \quad (2.18)$$

Thus, we can measure the column density of a BEC from a CCD image as

$$n(\mathbf{r}) = -\frac{1}{\sigma} \ln \left(\frac{I_{\text{img}} - I_{\text{dark}}}{I_{\text{beam}} - I_{\text{dark}}} \right). \quad (2.19)$$

For more information of our imaging system, see S.S. Kim's publication [72] and S.W. Seo's thesis [64].

In our experiments, atoms are possible to exist in all three spin states. But, atoms in each spin state share the same space in the main chamber. Therefore, we use the Stern-Gerlach spin separation to spatially separate a condensate by the spin components. When we apply an inhomogeneous magnetic fields in plane, atom feels a force of $\mathbf{F} = \nabla(\vec{\mu} \cdot \vec{B}) = g_F \mu_B m_F \nabla(\frac{\vec{\mu}}{|\vec{\mu}|} \cdot \vec{B})$, depending on the m_F . Then, we get rid of the magnetic field gradients and take absorption images after a short time-of-flight time [Fig. 2.4.1(a)]. During the spin separation, the ODT is turned off.

We crop an image as shown in Fig. 2.4.1(a) to extract the condensate fraction by each spin. Then, the cropped images are fitted by

$$n_{2\text{D}}(\mathbf{r}) = n_c \max \left[1 - \sum_{i=1,2} \frac{x_i^2}{R_i^2}, 0 \right]^{3/2} + n_{\text{th}} \prod_{i=1,2} e^{-\frac{x_i^2}{W_i}}, \quad (2.20)$$

where n_c , n_{th} are constants, and R_i , W_i are the widths of a condensate and thermal cloud, respectively. However, the quenched condensate has spatial structures due to the spin-wave excitations, disturbing the fitting. So, we obtain 1D

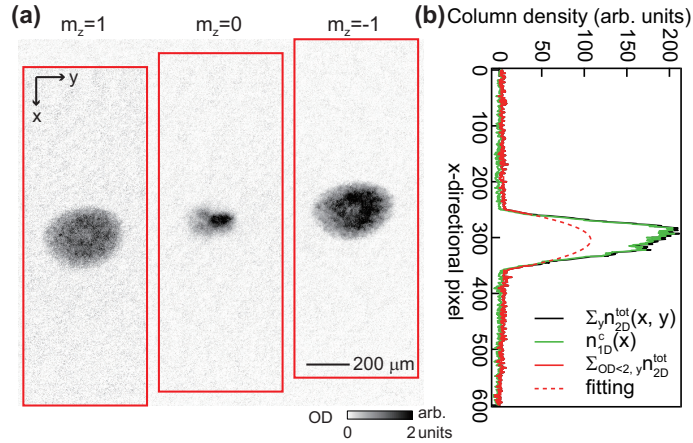


Figure 2.8: (a) Example absorption images for each spin components. (b) displays the column optical densities (ODs) for $m_z = -1$ component. Black solid line is 1D column density, n_{1D} , obtained by integrating 2D column density, n_{2D} in y -direction. Red solid line is 1D column density, obtained by summing OD value less than 2 from (a). Red dotted line is a fitting line for red solid line. Green line is extracted by subtracting thermal parts from black solid line.

column density, n_{1D}^{tot} , from Fig. 2.4.1(a) by integrating 2D column density in y -direction. Then, we cut a certain value off, which does not distort the bimodal density profile and fit it with

$$n_{1D}(x) = n_c \max \left[1 - \frac{x^2}{R_x^2}, 0 \right]^2 + n_{\text{th}} e^{-\frac{x^2}{W_x}}. \quad (2.21)$$

We can get the information of thermal gas from the 2nd term and finally, the information of the condensate such as the number and size is extracted by subtracting the thermal gas distribution from $n_{1D}^{\text{tot}}(x)$.

The Stern-Gerlach imaging is useful and simple methods to measure the spin dynamics. However, it distorts the condensate and the sizes of the condensate for each spin components varies, when the atoms are dragged. Thus, we build magnetization-sensitive phase contrast imaging.

2.4.2 Magnetization-sensitive phase contrast imaging

Magnetization-sensitive phase contrast imaging (PCI) enable us to detect spin turbulence and magnetized spin textures such as HQVs or spin turbulence. We use σ^- -polarized probe beam, detuned from the D2 atomic resonance. The detuning is 20 MHz between $|F = 1\rangle$ and $|F' = 2\rangle$ ⁵.

The magnetization-sensitive PCI is homodyne detection by interfering the scattered light from a sample with the unscattered light. Let an incident electric field of the off-resonant laser beam, $\mathbf{E}_{\text{in}} = \mathbf{E}_0$. Then, the electric field after passing a BEC is given as

$$\mathbf{E}_{\text{out}} = e^{i\phi}\mathbf{E}_0 = \mathbf{E}_{\text{scatt}} + \mathbf{E}_{\text{unscatt}} = \Delta\mathbf{E} + \mathbf{E}_0, \quad (2.22)$$

where ϕ is a phase shift due to the sample⁶. To develop the distinguishable phase contrast signal for each spin component, we place a phase dot, which causes $\pi/2$ phase shift of a light. The location of a phase dot is the lens focus prior to the imaging plane. Then, the electric field at image plane is rewritten as

$$\mathbf{E}_{\text{pc}} = \mathbf{E}_{\text{scatt}} + e^{i\frac{\pi}{2}}\mathbf{E}_{\text{unscatt}} = (e^{i\phi} - 1 + e^{i\frac{\pi}{2}})\mathbf{E}_0. \quad (2.23)$$

Depending on the states of atoms, the interference between the $\mathbf{E}_{\text{scatt}}$ and $\mathbf{E}_{\text{unscatt}}$ is either constructive [Fig. 2.4.2(b)] or destructive [Fig. 2.4.2(a)]. For a BEC in $m_z = -1(+1)$ state, we use constructive interference and get bright(dark) phase-contrast signal [Fig. 2.4.2(c)].

However, this phase-contrast imaging methods have limitations that it is difficult to distinguish the $m_z = 0$ domains from the domains, where the

⁵Unfortunately, the detuning is too close to the resonance, and we can take only one image for a single experimental sequence.

⁶ ϕ is well approximated as $\delta_{ij} + \frac{\chi_{ij}}{2}$, where χ_{ij} is the dielectric susceptibility and it represent the state-dependent phase shift. Therefore, $\mathbf{E}_{\text{out},i} = \exp(\delta_{ij} + \frac{\chi_{ij}}{2})\mathbf{E}_{\text{in},j}$.

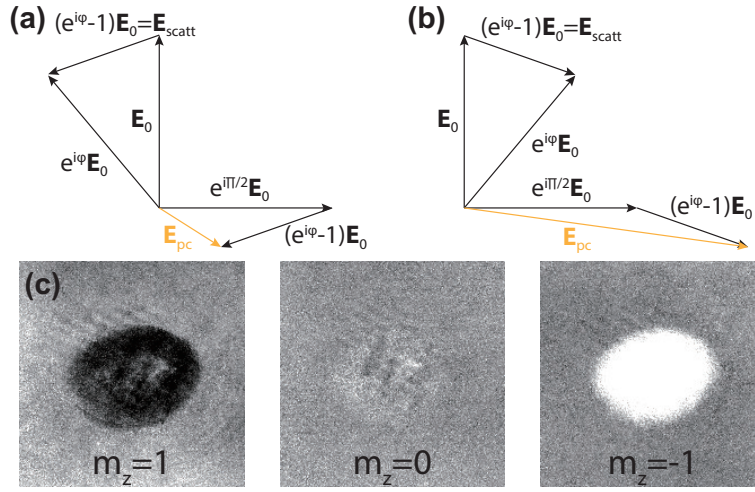


Figure 2.9: Electric field phasor diagram for (a) destructive and (b) constructive interference. (c) Magnetization-sensitive PCI signal. Raw images without any analysis. The PCI signal of $m_z = +1(-1)$ spin component is dark(bright) from the constructive(destructive) interference. The BEC in the $m_z = 0$ spin component has almost identical signal with the background.

$m_z = \pm 1$ atoms are equally populated⁷. When we obtain the magnetization distribution, the maximum magnetization is determined from the signal of HQV cores. The magnetization profile of a HQV core is measured as a Gaussian function of $M_z(r) = \pm M_{z0}e^{-r^2/r_{\text{core}}^2}$ and the peak magnetization $|M_{z0}|$ becomes maximum magnetization of 1. Then, we transform three signals of ± 1 and 0 to the magnetization by using the polynomial fit. For more information, see S.W. Seo's thesis [64].

⁷In addition, this magnetization imaging depends on the density. Thus, it does not guarantee the linearity of the signals. It is slightly brighter in the denser region of $m_z = +1$ image.

Chapter 3

The EAP-to-EPP phase transition

One of the accessible far-from-equilibrium dynamics is phase transition dynamics as aforementioned in chapter 1. A quench protocol is typically employed to explore nonequilibrium dynamics [73], where a system is prepared in a well-defined initial state and then its evolution is precisely examined after the system's Hamiltonian is rapidly changed. One of the key topics in current research activities is quantum phase transition dynamics, which addresses the important question of how a many-body system evolves into a newly ordered quantum state. Recently, it was theoretically proposed that scaling behavior occurs in the phase-transition dynamics near quantum critical points [74–79], and the existence of scaling and universality was indeed demonstrated in various experiments of quantum phase transitions [60, 61, 80, 81].

For an antiferromagnetic spinor BEC, the spin state is parameterized with a spin nematic vector $\vec{d} = (d_x, d_y, d_z)$, such that the system is in the

$|m_F = 0\rangle$ state for the quantization axis along \vec{d} . In an external magnetic field, $\vec{B} \parallel \hat{z}$, a uniaxial spin anisotropy is imposed on the system due to the quadratic Zeeman energy $E_z = q\langle F_z^2 \rangle = q(1 - d_z^2)$, and there exist two ground states depending on the quadratic Zeeman shift, q : easy-axis polar (EAP) phase for $q > 0$ [Fig. 3.2](a) and easy-plane polar (EPP) phase for $q < 0$. In this chapter, we introduce our experiments on the EAP-to-EPP phase transition in terms of scaling behavior for spin turbulence generation and the creation of topological excitations. Interestingly, the phase transition between EAP and EPP phases is 1st-order phase transition in the mean-field description, but the continuous spin-rotation symmetry in the xy -plane is spontaneously broken. Finally, topological point defects, which are half-quantum vortices (HQVs) in the EPP phase [41, 82–84], can be created in the spatially extended 2D system [Fig. 3.2(b)].

- Seji Kang, Sang Won Seo, Joon Hyun Kim, and Yong-il Shin, “*Emergence and scaling of spin turbulence in quenched antiferromagnetic spinor BECs*”, Physical Review A **95**, 053638 (2017).

3.1 Dynamic instability for the EAP phase

When the system in equilibrium changes across the critical point, the quantum fluctuations are amplified and leads to the quantum phase transition. For the weak excitations, they are described by the Bogoliubov theory.

Let the field operator for each spin as $\hat{\psi}_m = \psi_m + \delta\hat{\psi}_m$, where ψ_m is the mean-field value of condensate with zero momentum, and the deviation of $\delta\hat{\psi}_m$ is the non-condensate field with non-trivial momentum. Therefore, the

non-condensate field operator is expressed as $\delta\hat{\psi}_m = \frac{1}{\sqrt{V}} \sum_{\mathbf{k} \neq 0} \hat{a}_{m,\mathbf{k}} e^{i\mathbf{k}\cdot\mathbf{r}}$, and the field operator is written as

$$\hat{\psi}_m = \frac{1}{\sqrt{V}} \sum_{\mathbf{k}} \hat{a}_{m,\mathbf{k}} e^{i\mathbf{k}\cdot\mathbf{r}}, \quad (3.1)$$

where V is the volume of the system and $\hat{a}_{m,\mathbf{k}}$ is the annihilation operator of a boson with wave number \mathbf{k} . Substitute Eqn. 3.1 to the total Hamiltonian (Eqn. 1.11), then we get

$$\begin{aligned} H = & \sum_{m,\mathbf{k}} (\epsilon_{\mathbf{k}} - pm + qm^2) \hat{a}_{m,\mathbf{k}}^\dagger \hat{a}_{m,\mathbf{k}} \\ & + \frac{1}{2V} \sum_{m,m',l,l'} \sum_{\mathbf{k},\mathbf{p},\mathbf{q}} (c_0 \hat{a}_{m,\mathbf{p}}^\dagger \hat{a}_{m',\mathbf{q}}^\dagger \hat{a}_{m,\mathbf{p}+\mathbf{k}} \hat{a}_{m',\mathbf{q}-\mathbf{k}} + c_2 \mathbf{F}_{mm'} \cdot \mathbf{F}_{ll'} \hat{a}_{m,\mathbf{p}}^\dagger \hat{a}_{l,\mathbf{q}}^\dagger \hat{a}_{m',\mathbf{p}+\mathbf{k}} \hat{a}_{l',\mathbf{q}-\mathbf{k}}), \end{aligned} \quad (3.2)$$

where $\epsilon_{\mathbf{k}} = \hbar^2 \mathbf{k}^2 / 2M$ and \mathbf{F} is a set of the spin-1 matrices.

In case of the EAP phase, the field operator is given as

$$\hat{\Psi} = \begin{bmatrix} 0 \\ \psi_0 \\ 0 \end{bmatrix} + \begin{bmatrix} \delta\hat{\psi}_{+1} \\ \delta\hat{\psi}_0 \\ \delta\hat{\psi}_{-1} \end{bmatrix}. \quad (3.3)$$

So, the non-condensed atoms in the $|m_F = 0\rangle$ develop the density fluctuations and the atoms in the $|m_F = \pm 1\rangle$ develops the spin fluctuations. These density and spin fluctuations are completely decoupled [85]. Using the number conservation of $\hat{N}_0 \equiv \hat{N} - \sum_{m,\mathbf{k} \neq 0} \hat{a}_{m,\mathbf{k}}^\dagger \hat{a}_{m,\mathbf{k}}$, we can replace \hat{N} with a fixed scalar value. Then, the Hamiltonian of equation 3.2 is given as

$$\begin{aligned} H = & \frac{c_0 n^2 V}{2} + \sum_{\mathbf{k} \neq 0} [(\epsilon_{\mathbf{k}} + c_0 n) \hat{a}_{0,\mathbf{k}}^\dagger \hat{a}_{0,\mathbf{k}} + \frac{c_0 n}{2} (\hat{a}_{0,\mathbf{k}}^\dagger \hat{a}_{0,-\mathbf{k}}^\dagger + \hat{a}_{0,\mathbf{k}} \hat{a}_{0,-\mathbf{k}})] \\ & + \sum_{m=\pm 1} \{(\epsilon_{\mathbf{k}} + mp + q + c_2 n) (\hat{a}_{m,\mathbf{k}}^\dagger \hat{a}_{m,\mathbf{k}})\} + c_2 n (\hat{a}_{1,\mathbf{k}}^\dagger \hat{a}_{-1,-\mathbf{k}}^\dagger + \hat{a}_{1,\mathbf{k}} \hat{a}_{-1,-\mathbf{k}})], \end{aligned} \quad (3.4)$$

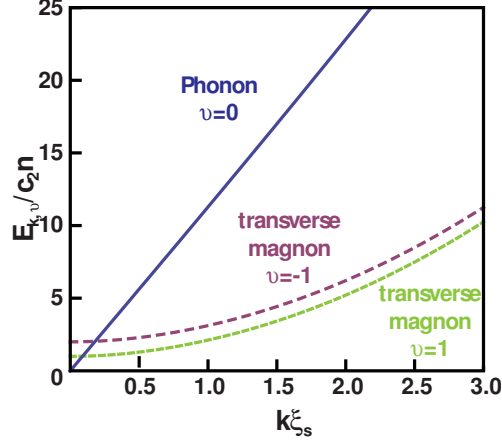


Figure 3.1: Bogoliubov dispersion relations in the EAP phase. There exist three modes of the excitation spectra—the phonon, and two transverse magnon modes. Parameters: $c_2 n = 14.0h$, $c_0 n = 882h$ and $\xi_s = 2.2 \mu\text{m}$ corresponding to our experiment conditions, and $p = 0.5c_2 n$, $q = 0.8c_2 n$.

where V is the volume of the system and $n = N/V$. To diagonalize Eqn. 3.4, apply Bogoliubov transformations:

$$\hat{a}_{0,\mathbf{k}} = h_k \hat{b}_{0,\mathbf{k}} - g_k \hat{b}_{0,-\mathbf{k}}^\dagger \quad (3.5)$$

$$\hat{a}_{\pm 1,\mathbf{k}} = u_{\pm,k} \hat{b}_{\pm,\mathbf{k}} - v_{\pm,k} \hat{b}_{\mp,-\mathbf{k}}^\dagger, \quad (3.6)$$

where $h_k, g_k, u_{\pm,k}$ and $v_{\pm,k}$ are real satisfying $|h_k|^2 - |g_k|^2 = 1$ and $|u_{\pm,k}|^2 - |v_{\pm,k}|^2 = 1$. After some calculation, we find that the Bogoliubov Hamiltonian is expressed

$$H = E_g + \sum_{\mathbf{k} \neq 0} [E_{0,\mathbf{k}} \hat{b}_{0,\mathbf{k}}^\dagger \hat{b}_{0,\mathbf{k}} + E_{+,\mathbf{k}} \hat{b}_{+,\mathbf{k}}^\dagger \hat{b}_{+,\mathbf{k}} + E_{-,\mathbf{k}} \hat{b}_{-,\mathbf{k}}^\dagger \hat{b}_{-,\mathbf{k}}], \quad (3.7)$$

where E_g is the ground-state energy and the energy spectra are given by

$$E_{0,\mathbf{k}} = \sqrt{\epsilon_{\mathbf{k}}(\epsilon_{\mathbf{k}} + 2c_0 n)} \quad \text{associated with the phonon excitations} \quad (3.8)$$

$$E_{\pm,\mathbf{k}} = \sqrt{(\epsilon_{\mathbf{k}} + q)(\epsilon_{\mathbf{k}} + 2c_2 n + q)} \pm p \quad \text{magnon excitations.} \quad (3.9)$$

The two magnon excitations are degenerate when $p = 0$. These dispersion relations are described in Fig. 3.1.

When the quadratic Zeeman energy, q becomes negative, $E_{\pm, \mathbf{k}}$ is imaginary and excites the two magnon modes, leading to the EAP-to-EPP phase transition. The number of atoms in the $|m_F = \pm 1\rangle$ grows exponentially [12] following

$$\begin{aligned} \langle \hat{n}_{\pm 1, \mathbf{k}} \rangle &= \langle \hat{a}_{\pm 1, \mathbf{k}}^\dagger(t) \hat{a}_{\pm 1, \mathbf{k}}(t) \rangle & (3.10) \\ &= f(E_{\pm, \mathbf{k}}, t) \langle \hat{n}_{\pm 1, \mathbf{k}}(0) \rangle + \left(\frac{c_2 n}{|E_{\pm, \mathbf{k}}|} \right)^2 \sinh(|E_{\pm, \mathbf{k}}|t/\hbar) \langle \hat{n}_{\mp, -\mathbf{k}}(0) \rangle + 1 \\ &\sim e^{2|E_{\pm, \mathbf{k}}|t/\hbar}, \end{aligned}$$

where the first term is related to the thermal fluctuations and the term of $\langle \hat{n}_{\mp, -\mathbf{k}}(0) + 1 \rangle$ is associated with the quantum depletion and the quantum vacuum fluctuations. For small $|q| \ll c_2 n$, the magnon modes with $k < k_q \equiv \sqrt{2|q|m}/\hbar$ are excited with an assumption that the thermal fluctuations are insignificant. The instability rate, Γ_q , is given by the most unstable magnon mode and $\Gamma_q = 2|E_{\pm, \mathbf{k}=0}|/\hbar \approx \sqrt{8|q|c_2 n}/\hbar$. Thus, we can define the time and length scales of $t_q = 2\pi/\Gamma_q \propto |q|^{-\frac{1}{2}}$ and $l_q = 1/k_q \propto |q|^{-\frac{1}{2}}$. We can expect that the scaling behavior depends on the quench depth, $|q|^{\frac{1}{2}}$.

3.2 Experimental setup & Methods

Preparation of initial condensate in the EAP state

Our experiment begins by preparing a BEC of ^{23}Na atoms in the $|F = 1, m_F = 0\rangle$ state [41]. The condensate is confined in an optical potential with trapping frequencies of $(\omega_x, \omega_y, \omega_z) = 2\pi \times (3.8, 5.5, 400)$ Hz. The condensate

contains $N^c \approx 8.0 \times 10^6$ atoms and its Thomas-Fermi radii are $(R_x, R_y, R_z) \approx (232, 160, 2.2) \mu\text{m}$. The sample preparation is carried out in a magnetic field of $B_z = 0.5 \text{ G}$ along the z direction. Initially, the sample has only $m_z = 0$ spin component and its thermal fraction is less than 10%. To initiate the transition dynamics to the EPP phase, we first adiabatically ramp B_z to 33 mG for 0.2 s and then, we suddenly turn on a microwave field to change the quadratic Zeeman energy to a negative value q [51, 86]. The residual field gradient was measured to be less than 0.1 mG/cm.

In our experiment, q/h ranges from -1.4 Hz to -20 Hz . The excitation energy of the initial state after the quench is given by $|q|$ with respect to the EPP ground state, which is much smaller than the condensate chemical potential $\mu = h \times 880 \text{ Hz}$. Therefore, the subsequent evolution of the condensate can be approximated as pure spin dynamics, not involving density excitations. For the peak atomic density n of the sample, the spin interaction energy is $c_2 n/h = 14 \text{ Hz}$ [87] and the spin healing length is $\xi_s = \hbar/\sqrt{2mc_2 n} \approx 4.0 \mu\text{m}$. Because the condensate thickness R_z is smaller than ξ_s , the spin dynamics in the oblate condensate is effectively 2D.

SG imaging

The spin texture of the condensate is examined by taking an absorption image after SG spin separation. After releasing the trapping potential, we apply a magnetic field gradient pulse along the x direction and let the three $m_z = 1, 0, -1$ spin components are spatially separated for a 24-ms time of flight. The image reveals the density distributions of the individual spin components. The applied field gradient was slightly inhomogeneous to make the $m_z = \pm 1$ spin components expand differently. We used $F = 1$ imaging and calibrated the

absorption coefficients for each spin component [Chap. 2].

Magnetization imaging

Spin-sensitive *in-situ* phase-contrast imaging is also employed to obtain further information on the spatial magnetization structure of the condensate [Chap. 2]. The probe beam frequency is tuned to give a signal proportional to the axial magnetization M_z , i.e., the density difference of the $m_z = \pm 1$ spin components. The contribution of the $m_z = 0$ spin component to the imaging signal is not significant and we interpret the phase-contrast image as the axial magnetization distribution $M_z(x, y)$ of the condensate.

Measuring the spin turbulence: Power spectrum

We first obtained a reference image by averaging over ten images that were taken for the same experiment and subtracted the reference image from individual images to remove systematic fringes not related with the spin texture of the sample. Then, the power spectrum $P(\vec{k}) = \left| \int d\vec{r}^2 e^{i\vec{k}\cdot\vec{r}} M_z(\vec{r}) \right|^2$ was obtained by averaging the squared Fourier transforms of the subtracted images and subtracting the photon shot noise level. We introduce a relative spectrum $\tilde{P}(\vec{k}) = P(\vec{k})/P_{\text{eq}}(\vec{k})$ where $P_{\text{eq}}(\vec{k})$ is the average spectrum of samples at thermal equilibrium in the EPP phase. Because P_{eq} is measured with the same imaging system, the relative spectrum \tilde{P} provides spectral information free from the systematic modifications of the imaging system. For the determination of the equilibrium spectrum P_{eq} , we selected samples for $q/h = -1.4$ Hz at $t = 5$ s, in particular, without having HQVs because HQVs can affect the spectrum due to their magnetized cores and magnon excitations generated by their collisional

motions [84]. $\tilde{P}(\vec{k})$ was isotropic and we obtained a 1D spectrum $\tilde{P}(k)$ by azimuthally averaging it over $|\vec{k}| = k$.

3.3 Emergence of Spin turbulence

Figure 3.2, 3.3 and 3.4 display image data sequences of the quenched condensate for different q values from -1.4 Hz to -20 Hz. After a short hold time, an irregular spin texture starts appearing in the condensate. It is clearly shown that the $m_z = \pm 1$ components are spatially separated from the $m_z = 0$ component [Figs. 3.2(c, e) and 3.3(c, e)], which results from the immiscibility of the $m_z = \pm 1$ components from the $m_z = 0$ component [26]. Spin domains formed by an equal mixture of the $m_z = \pm 1$ components have $\vec{d} \perp \hat{z}$, where the azimuthal direction of \vec{d} is determined by the relative phase of the two spin components. It is observed that the irregular spin texture emerges first in the center region of the condensate and expands over the whole condensate. We attribute it to the inhomogeneous density distribution of the trapped condensate because $\Gamma_q \propto \sqrt{n}$.

The appearance of the irregular spin texture is also observed in the magnetization image [Figs. 3.2(d, f) and 3.3(d, f)]. In the spin-exchanging process where two $m_z = 0$ atoms are scattered into a pair of $m_z = +1$ and -1 atoms, the quadratic Zeeman energy is converted into the kinetic energy of the $m_z = \pm 1$ atoms, imparting opposite momenta to the two atoms. Thus, spin currents are generated in the $m_z = \pm 1$ spin domains and axial magnetization develops at the domain boundaries. The irregular structure in the M_z image constitutes an observation of spin turbulence having a complex spin current pattern.

As the hold time t increases, the $m_z = 0$ spin component keeps depleting

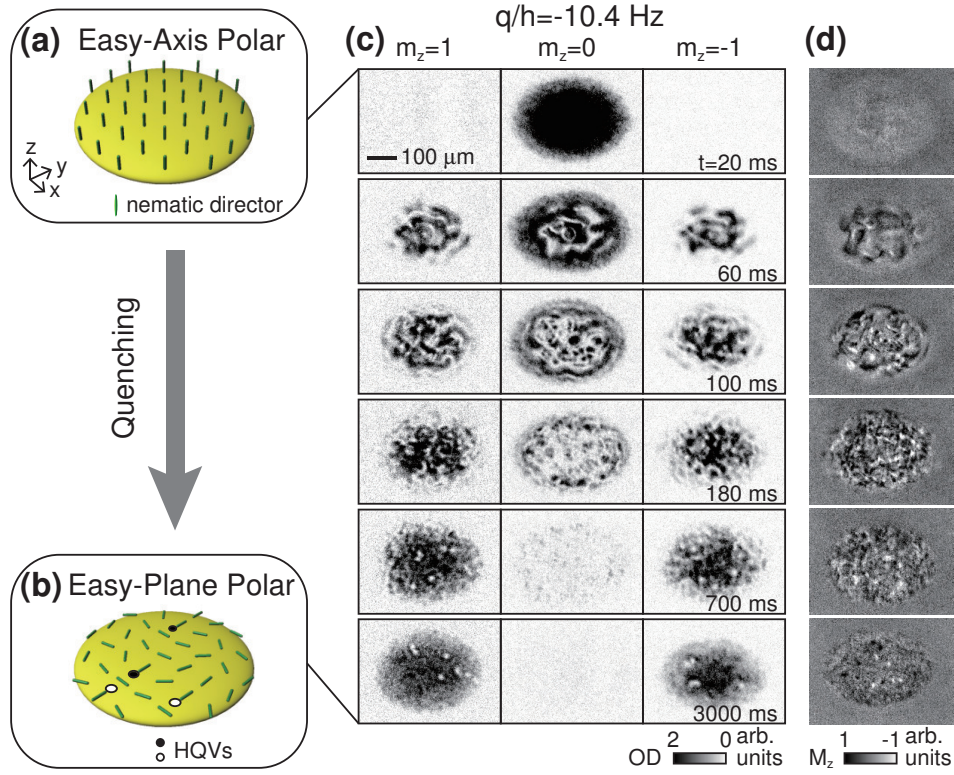


Figure 3.2: Phase transition from the EAP phase to the EPP phase of an antiferromagnetic spin-1 BEC. (a) The spin nematic director \vec{d} is initially aligned with the axial z direction, and (b) the phase transition to the EPP phase is triggered by a sudden change in the quadratic Zeeman energy, q . (c) Absorption images of the $m_z = 1, 0, -1$ spin components after 24 ms SG spin separation, and (d) *in situ* axial magnetization images $M_z(x, y)$ for various hold times t after the quench to $q/h = -10$ Hz. HQVs are identified with density-depleted holes in the SG images and their magnetized cores in the M_z images.

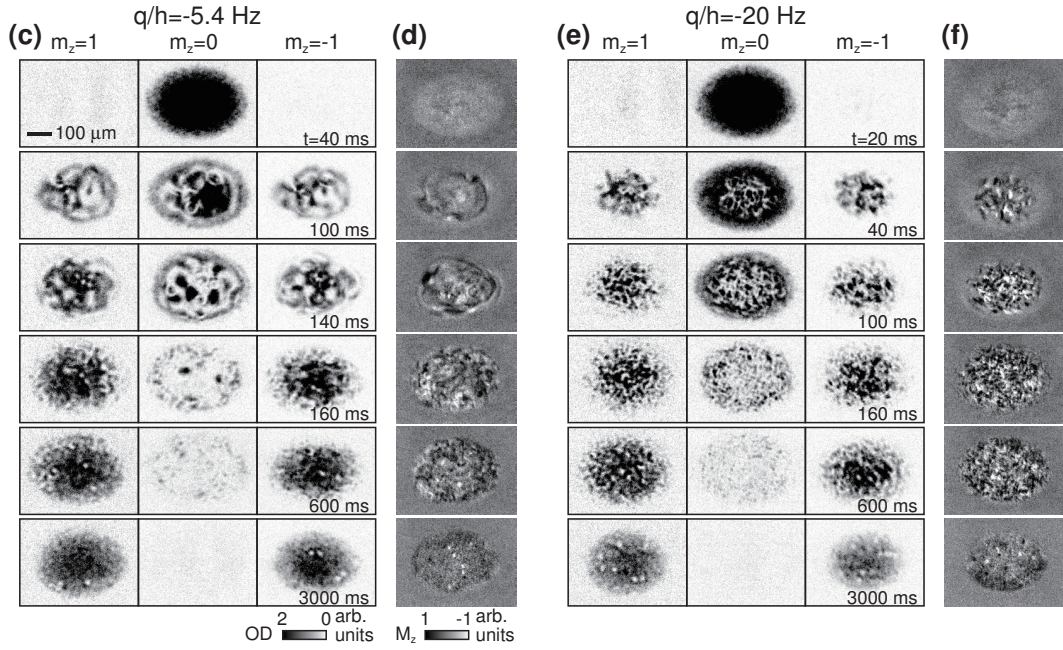


Figure 3.3: Phase transition dynamics from the EAP phase to the EPP phase of an antiferromagnetic spin-1 BEC after quench to (c) and (d) $q/h = -5.4$ Hz and (e) and (f) -20 Hz. (a) and (c) Absorption images of the $m_z = 1, 0, -1$ spin components after 24 ms SG spin separation, and (b) and (d) *in situ* axial magnetization images $M_z(x, y)$ for various hold times t .

and the spin texture becomes more complex. In particular, the length scale of the spin texture becomes smaller, implying a direct energy cascade in the spin turbulence. The condensate eventually relaxes into the EPP phase with the $m_z = 0$ component vanishing. In the final state, HQVs are observed as magnetized point defects in the M_z image [41] and also identified with density-depleted holes in the SG image.

3.3.1 Spin-wave excitation

It is apparent in the comparison between the two image data sets in Fig. 3.2 and Fig. 3.3 for $q/h = -5.4$ Hz, -10 Hz and -20 Hz that when the system is closer to the critical point, the time and length scales of the quench dynamics become slower and larger, respectively, which is consistent with the theoretical anticipation from the dynamic instability of the initial state. The length scale of the spin texture was even larger with lower $|q|$. For $|q/h| < 2$ Hz, we observed that the incipient spin texture shows a large ring-shaped pattern, which propagates toward the boundary and shortly becomes dismantled (Fig. 3.4(c,d)). The ring-shaped pattern has the same ellipticity of the trapped condensate and we believe that it corresponds to long-wavelength spin wave excitations induced by the trapping geometry of the finite-size sample [45, 46].

3.4 Characterizing the quench dynamics & spin turbulence

We first characterize the quench dynamics of the condensate by measuring the time evolutions of the fractional population, η , of the $m_z = 0$ component and the magnetization variance, $\langle \delta M_z^2 \rangle$, of the spin texture (Fig. 3.5). Here $\eta = N_0^c/N^c$ and $N^c = \sum_i N_i^c$, where N_i^c is the $m_z = i$ atom number of the condensate ($i = 1, 0, -1$) and determined from the SG absorption image [Fig. 2.4.1]. The thermal cloud contribution is subtracted using a Gaussian fit to the outer thermal wing. For the measurement of $\langle \delta M_z^2 \rangle$, we set the central $206 \mu\text{m} \times 206 \mu\text{m}$ region of the condensate as the region of interest.

The quench evolution starts with a delayed, rapid decrease of η as ex-

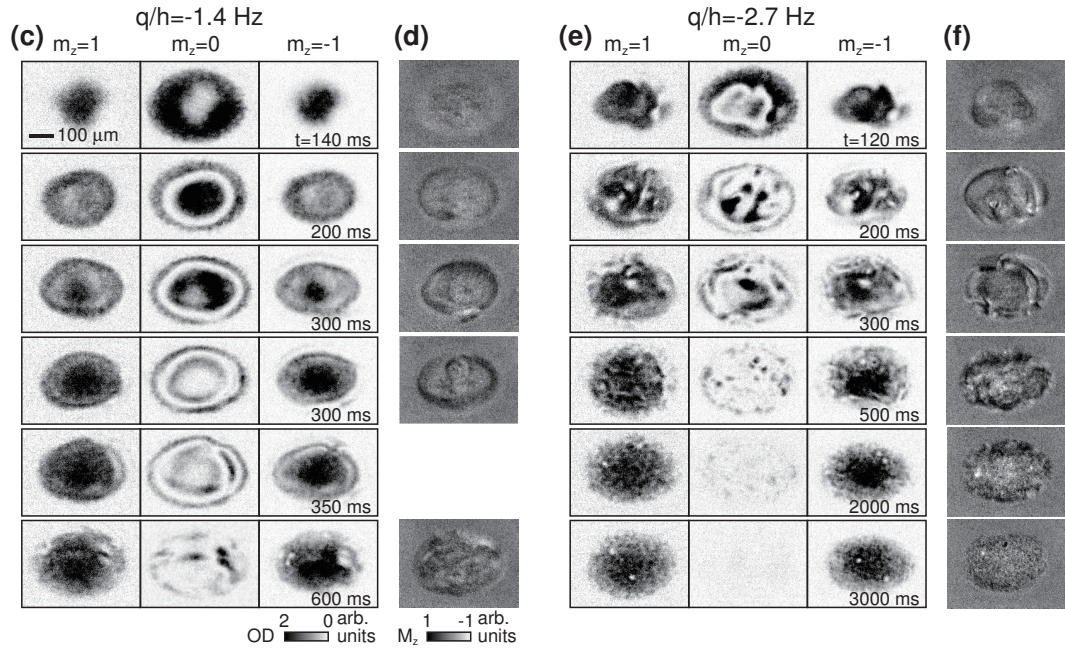


Figure 3.4: (a) and (b) Spin-wave excitations for $q/h = -1.4$ Hz. A ring-shaped oscillating spin texture appears and shortly becomes dismantled. (c) and (d) the EAP-to-EPP phase transition dynamics for $q/h = -2.7$ Hz. (a) and (c) Absorption images of the $m_z = 1, 0, -1$ spin components after 24 ms SG spin separation, and (b) and (d) *in situ* axial magnetization images $M_z(x, y)$ for various hold times t .

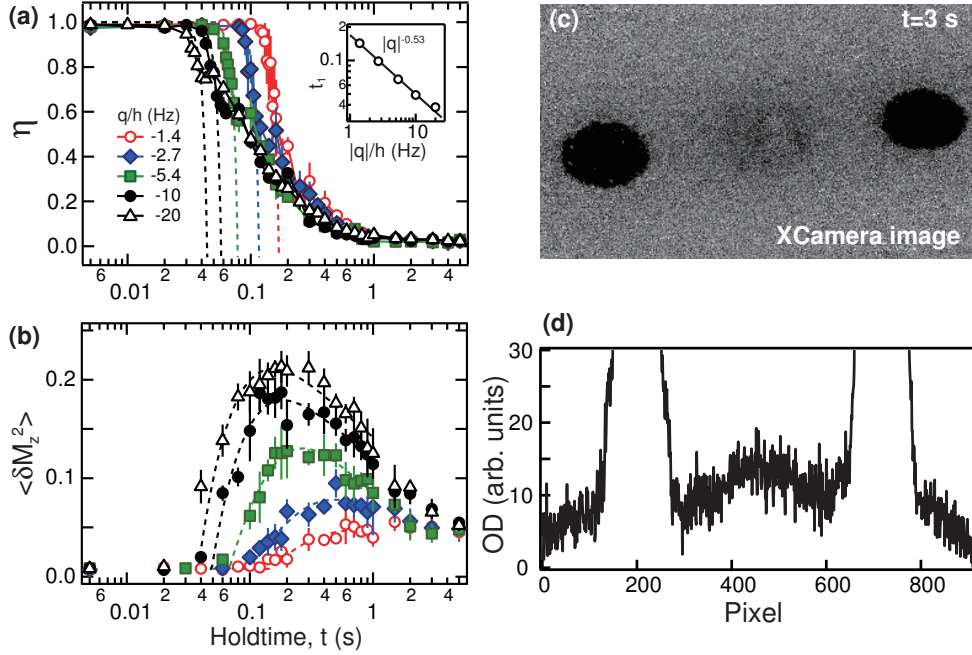


Figure 3.5: Temporal evolutions of (a) the fractional population η of the $m_z = 0$ spin component in the condensate and (b) the magnetization variance $\langle \delta M_z^2 \rangle$ for various q values. Each data point was obtained by averaging about five measurements, and its error bar denotes the standard deviation of the measurements. The dashed lines are guide lines for eyes. The inset in (a) shows the time t_1 for $\eta(t_1) = 0.8$ as a function of $|q|$. The solid line denotes a power-law fit to the data. (c) XCamera image taken for $q/h = -5.4$ Hz after hold time $t = 3$ s and (d) 1D optical density of (c).

pected from the exponential growth of dynamically unstable magnon modes. The early evolution of η is described as $\eta(t) = 1 - b \exp(\Gamma_q t)$, where b is a constant determined by the magnitude of magnetization fluctuations in the system. In the inset of Fig. 3.5(a), we display the time t_1 measured for $\eta(t_1) = 0.8$ as a function of $|q|$. A power-law fit to the experimental data gives an exponent of -0.53 ± 0.01 , which is in quantitatively good agreement with the predicted scaling of $\Gamma_q \sim |q|^{1/2}$. The measured t_1 values give $b \approx 4.6 \times 10^{-6}$, which is slightly higher than the value of $b \approx 3.3 \times 10^{-6}$ estimated for quantum depletion [See Appendix B] at our peak atomic density [88], indicating thermal enhancement in the experiment.

The rapid decay of η is halted at a certain threshold value η_{th} and after a short loitering period of a few tens of ms, η resumes its decay. Since $\langle \delta M_z^2 \rangle$ rapidly increases when η undergoes this change, it is reasonable to infer that the condensate enters a qualitatively different phase of the quench evolution, where the role of the generated spin turbulence becomes significant. The threshold value η_{th} monotonically increases from ≈ 0.4 for $q/h = -1.4$ Hz to ≈ 0.75 for $q/h = -20$ Hz [Fig. 3.9(c)].

The spin turbulence develops further with maximizing its $\langle \delta M_z^2 \rangle$ and then gradually relaxes with decreasing $\langle \delta M_z^2 \rangle$. After a long hold time, $t > 5$ s, the system is equilibrated with $\eta \simeq 0$ and stationary $\langle \delta M_z^2 \rangle$. In our experiment, the equilibrium value of $\langle \delta M_z^2 \rangle$ was insensitive to q because the final sample temperature is mainly determined by the heating from microwave field dressing and the evaporation cooling due to the finite trap depth. Note that for $q/h = -1.4$ Hz, $\langle \delta M_z^2 \rangle$ monotonically increases and saturates to the equilibrium value over time. At the equilibrium, the thermal fraction was about 30% and the sample temperature was estimated to be $T \approx 100$ nK. $k_B T \ll |q|$ and the

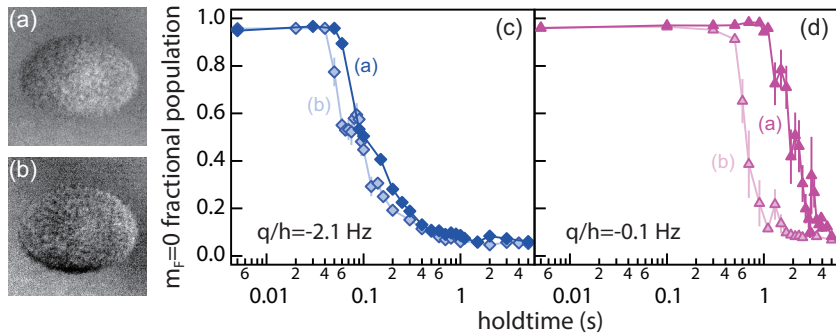


Figure 3.6: The effect of the field gradient on the dynamical instability. (a) and (b) are taken during the spin-dipole oscillation at 500 ms. (c,d) Temporal evolution of the phase transition dynamics. Darker and lighter data points are measured with the field gradients of (a) and (b), respectively. $q/h =$ (c) -2.1 Hz and (d) -0.1 Hz. The error bar is the standard error of the mean with at least 5 measurements.

thermal cloud was an equal mixture of the three spin components [89].

Interestingly, it seems that $m_z = 0$ component condensate still exist for long hold time $t = 3$ s [Fig. 3.5(c, d)]. $N_0^{\text{tot}}/N^{\text{tot}} = (N_0^{\text{c}} + N_0^{\text{th}})/\sum_{m_F}(N_{m_F}^{\text{c}} + N_{m_F}^{\text{th}}) \approx 0.1$. Because the condensate density of the $m_z = 0$ component is too dilute, it is not distinguishable from the thermal gas with the algorithm of extracting the fractional population (See section 2.4). In case of the EPP-to-EAP phase transition (Chap. 4), we observe the uneven transverse magnetization distribution in the condensate for a long hold time. The observation manifests the existence of the dilute EPP condensate. Thus, we can infer that the condensed $m_z = 0$ atoms still exist but the density is too dilute to spin-exchange collide.

Effect of the field gradient

The magnetic field gradient influences on the quench dynamics through phase transition dynamics. The field gradients, illustrated in Fig. 3.4(a) and

(b), are measured at 500 ms spin-dipole oscillating time. It seems that both field gradient is almost identical¹. But we can identify the magnitude of field gradient (a) is larger than the magnitude (b) by comparing the dynamical instability [Fig. 3.4(c,d)].

3.4.1 Time-Space scaling

To investigate the spatial structure of the generated spin turbulence, we measure the power spectrum of the magnetization distribution, $P(\vec{k}) = |\int d\vec{r} e^{i\vec{k}\cdot\vec{r}} M_z(\vec{r})|^2$. Figures 3.7(a,c) and 3.7(b,d) show the evolution of $\tilde{P}(k)$ for $q/h = -10$ Hz and -20 Hz, when $\langle\delta M_z^2\rangle$ increases and decreases, respectively. As noticed in the visual examination of the images in Figs. 3.2(d, f) and 3.3(d, f), the \tilde{P} measurement results show that the spin turbulence develops from low to high wave numbers k , i.e., from large to small length scales [Fig. 3.7(a)]. When $\langle\delta M_z^2\rangle$ decreases, the power spectrum decays towards the equilibrium level, $\tilde{P}_{\text{eq}} = 1$, where the spectral strength subsides faster in the lower- k region [Fig. 3.7(b)]. Over the whole growth and decay evolution, the spectral center-of-mass of $\tilde{P}(k)$ keeps moving towards high k and this observation suggests a direct energy cascade of spin wave excitations in the spin turbulence.

In Fig. 3.7(a), it is noticeable that when the spin turbulence is generated, the spectral slope is formed in $\tilde{P}(k)$ and propagates to high- k regions in a self-similar manner. In Fig. 3.7(c), we display $\tilde{P}(k)$ at the time when $\langle\delta M_z^2\rangle$ is maximum for various q values and we observe that the spectral slopes are

¹You might say that (b) seems to show stronger field gradient than (a). In my experience, the field gradient of (a) is stronger. In (a), $m_z = +1(-1)$ condensate is dominant in the right(left) region, manifesting there exist subtle spin-dipole oscillation. But, there is no spin-dipole oscillation in (b). The black region in (b) appears due to the higher order of the field gradient, $O((B_{ij}x_j/B_0)^2)$, from Eqn. 2.2.

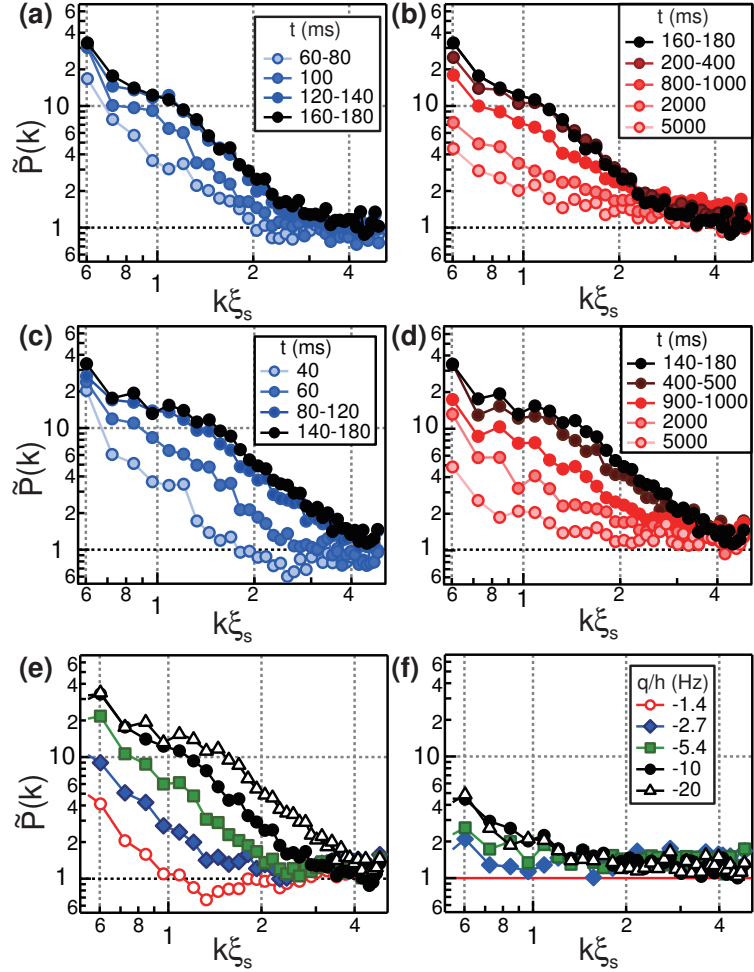


Figure 3.7: Relative power spectra $\tilde{P}(k)$ of the axial magnetization $M_z(x, y)$ of the quenched BEC. Evolution of $\tilde{P}(k)$ for (a), (b) $q/h = -10$ Hz and (c), (d) -20 Hz when $\langle \delta M_z^2 \rangle$ (a), (c) increases and (b), (d) decreases [Fig. 3.5 (b)]. $\tilde{P}(k)$ (e) at the time when $\langle \delta M_z^2 \rangle$ is maximum and (f) at $t = 5$ s when the quenched BEC is thermally equilibrated. The reference spectrum $\tilde{P}(k) = 1$ was obtained from the thermal equilibrium samples at $T \approx 100$ nK, having no HQVs.

almost identical while the characteristic wave number increases with increasing $|q|$. Power-law scalings in the spin turbulence of antiferromagnetic BECs were predicted by Fujimoto *et al.* [90, 91], but further analysis of our experimental data is limited by a lack of quantitative understanding of $P_{\text{eq}}(k)$. In Ref. [92], Symes *et al.* calculated the static structure factor of the antiferromagnetic BEC in the EPP phase at low temperatures. Our sample temperature of $k_B T / (c_2 n) \approx 150$ is too high to be extrapolated from their results.

In Fig. 3.7(d), we display $\tilde{P}(k)$ at a long hold time $t = 5$ s, when the sample is thermally equilibrated. For high $|q|$, the spectral strength in $k \leq 1/\xi_s$ is still noticeably higher than the equilibrium level $\tilde{P}_{\text{eq}} = 1$. This is due to the presence of HQVs and we confirmed it by correlating the deviation magnitude in the low- k region with the HQV number (Fig. 3.10).

Spin turbulence generation is seeded by the amplification of dynamically unstable magnon modes in the initial EAP state, in which the characteristic time and length scales are given by $t_q \sim |q|^{-1/2}$ and $l_q \sim |q|^{-1/2}$. To examine the scaling properties of the subsequent development of spin turbulence, in Fig. 5(a) we display the time evolution data of $\langle \delta M_z^2 \rangle$ as functions of the rescaled time $\tilde{t} \equiv t/t_q$. For all q , $\langle \delta M_z^2 \rangle$ starts its rapid increase at $\tilde{t}_1 \approx 1.7$ and becomes maximized in a range of $5 < \tilde{t} < 10$. In Fig. 5(b), we display the relative power spectra $\tilde{P}(k)$ for maximum $\langle \delta M_z^2 \rangle$ as functions of the rescaled wave number $\tilde{k} \equiv k/k_q$. All the spectra collapse into a single line for $1.5 < \tilde{k} < 4$. This observation demonstrates that the length scaling $l_q \sim |q|^{1/2}$ of the initial state is preserved in the subsequent turbulence generation dynamics.

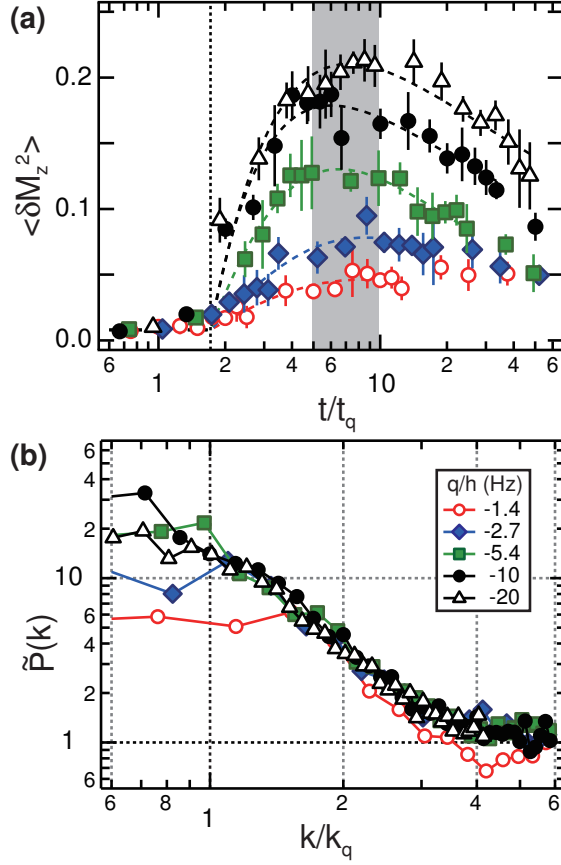


Figure 3.8: Time-space scaling in the spin-turbulence generation. (a) Evolution of $\langle \delta M_z^2 \rangle$ as a function of the rescaled time $\tilde{t} = t/t_q$, with $t_q = h\sqrt{8|q|c_2n}$. The vertical dotted line denotes the time, when $\eta = 0.8$, and the gray region indicates the time window for $\langle \delta M_z^2 \rangle$ to be maximized. (c) Relative spectra $\tilde{P}(k)$ with maximum $\langle \delta M_z^2 \rangle$ [Fig. 3.7 (d)] as functions of the rescaled wave number $\tilde{k} = k/k_q$, with $k_q = \sqrt{2|q|m/h}$.

3.5 Spin population relaxation

As the spin turbulence develops, η exhibits different decay behavior for $\eta < \eta_{th}$ [Figs. 3.9(a, b)]. In Fig. 3.9(d), we display the decay curves of η for various q values as functions of $t_d = t - t_2$, where t_2 is the starting time of the turbulence phase. η shows a nonexponential decay, where the relative decay rate $\gamma = -\frac{1}{\eta} \frac{d\eta}{dt}$ decreases as η decreases. In the turbulence phase, the $m_z = 0$ spin component, being spatially separated from the $m_z = \pm 1$ spin components, forms axial polar domains in the condensate (Fig. 3.2-3.4). Since the density of the $m_z = 0$ atoms in the spin domains is regulated by the condensate chemical potential, a local two-body decay process would result in a constant decay of η , which cannot explain the observed nonexponential decay. The inset of Fig. 3.9(d) is a log-log plot of the same data with adjusted time offsets. The exponent determination from a power-law fit to the data is not reliable due to its high sensitivity of the time offsets.

In our experiments, the decay rate γ is found to be insensitive to q , which is different from a general expectation of higher γ for higher excitation energy, $|q|$. It might be speculated that small domain size for high $|q|$ proportionally suppresses γ , or it may be due to the high thermal energy of the system, $k_B T \gg |q|$ [93, 94]. In Fig. 3.9(e), we characterize the relaxation of the thermal cloud during the turbulence phase for $q/h = -10$ Hz. The $m_z = 0$ spin fraction of the thermal cloud relaxes within 0.2 s to the equilibrium level of one third and the thermal fraction of the sample increases from $\approx 20\%$ to $\approx 30\%$. The relaxation time is compatible to $1/\gamma = 0.2 \text{ s} \sim 0.6 \text{ s}$ but the decrease of γ is not in accord with the increase of the sample temperature. The spin turbulence relaxation dynamics including the coupling to the thermal cloud [95] merits

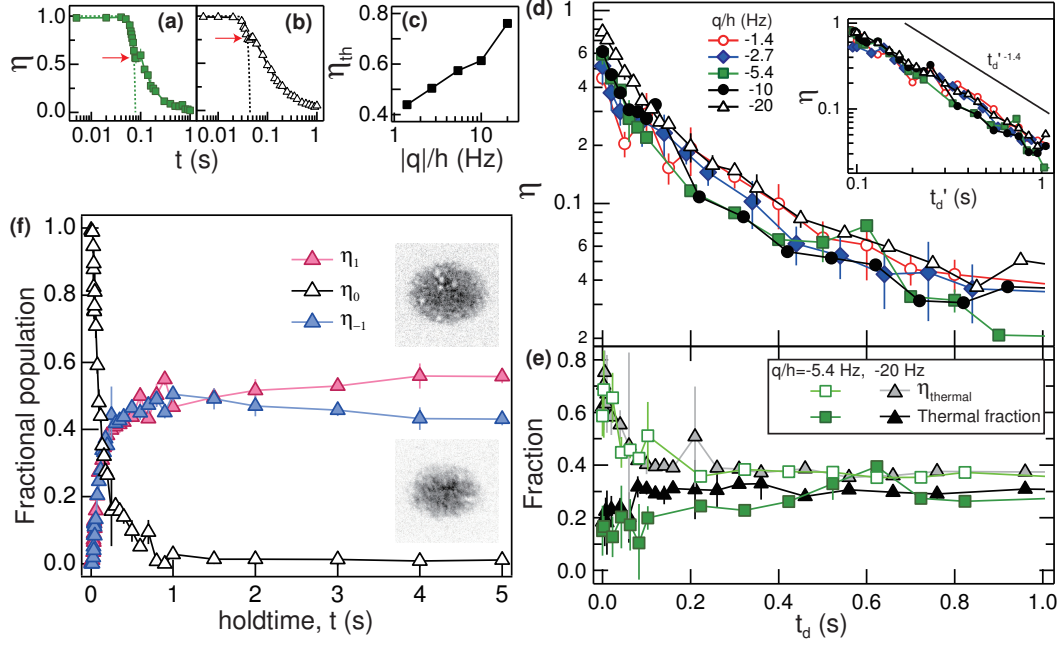


Figure 3.9: Decay of η in the turbulence phase. $\eta(t)$ for (a) $q/h = -5.4$ Hz and (b) -20 Hz; the threshold values η_{th} are indicated by the right arrows. (c) η_{th} versus $|q|$. (d) Decay curves of η as functions of $t_d = t - t_2$, where t_2 is the starting time of the turbulence phase. The inset shows the same data with adjusted time offsets, and the solid line is a power-law fit to the data. (e) Relaxation of the thermal clouds. The solid symbols denote the thermal fraction of the sample, and the open symbols denote the $m_z = 0$ spin fraction of the thermal cloud. Each data point is obtained by averaging about five measurements, and its error bar denotes the standard deviation of the measurements. (f) The population evolution of each spin components for $q/h = -20$ Hz. The inset images are absorption images of $m_z = \pm 1$ clouds for hold time 5 s.

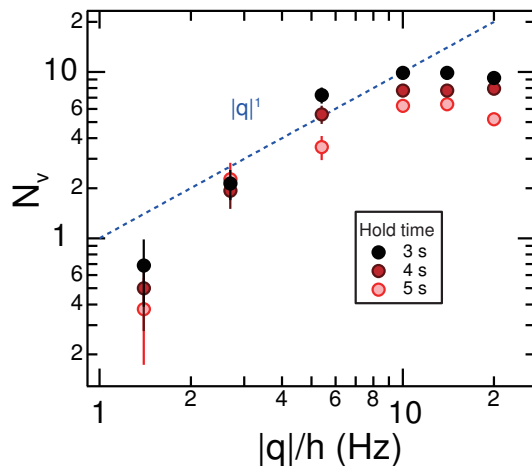


Figure 3.10: HQV number N_v versus $|q|$. N_v was measured by counting density-depleted holes in the SG images of the $m_z = \pm 1$ spin components. Each data point is the average of 15 measurements for the same experiment, and its error bars indicates the standard error of the mean. The blue dashed line denotes a power-law fit to the data in the range of $|q|/h \leq 10$ Hz for $t = 3$ s.

further investigation in future experiment.

You can recognize the different lifetime of atoms in $|m_F = \pm 1\rangle$ for large magnitude of $|q|$ due to the different coupling strength. For $t = 5$ s, the fractional population of $m_z = 1$ and -1 components are 0.56 and 0.43, respectively. The sizes of $m_z = \pm 1$ clouds in Fig. 3.4(e) are also vividly distinguishable for $t = 3$ s. The detuning $\Delta = -150$ kHz for $q/h = -20$ Hz (see section 2.3).

3.6 Topological Defects: Half-quantum vortex

At long hold times $t \geq 3$ s, when the $m_z = 0$ spin component almost vanishes in the condensate, HQVs are unambiguously identified with density-depleted holes in the SG images (Fig. 3.2). We measure the HQV number, N_v , and find that it increases with increasing $|q|$ and saturates for $|q|/h > 10$ Hz

(Fig. 3.10). When the spatial size of spin domains in the quenched condensate scales with l_q , the number of point defects created in the 2D system is expected to scale as $N_v \propto l_q^{-2}$ [7]. A power-law fit to the data for $t = 3$ s in the range of $|q|/\hbar \leq 10$ Hz gives an exponent of 1.0 ± 0.2 , which is consistent with the length scaling $l_q \sim |q|^{1/2}$ observed in the measurement results of $\tilde{P}(k)$. The saturation of N_v for high $|q|$ might indicate another length scale involving in the defect creation, such as the spin healing length ξ_s [96], but its possible effect was not observed in $\tilde{P}(k)$. Since HQVs can be pair-annihilated in the turbulence relaxation process, leading to a non-exponential decrease of N_v [97], the HQV number measured at long hold times may not linearly reflect the initial N_v of the quenched BEC.

3.7 Outlook

We can extend this work to a deeper quench regime with $|q| > 2c_2n$. In this case, the dynamic instability of the initial EAP state is driven by magnon modes with finite wave numbers centered at $k_q = \sqrt{2m(|q| - c_2n)}/\hbar$ [98]. It would be of high interest to examine how the energy injected at finite wave numbers flows in the subsequent evolution of spin turbulence [99]. Since the length scale $\sim 1/k_q$ becomes comparable to and even smaller than the spin healing length ξ_s , it might be speculated that qualitatively different turbulence states would emerge in this high $|q|$ regime. Figure 3.11 shows preliminary data for $q/\hbar = -40(2)$ Hz and $-80(10)$ Hz. The spin excitations occur in extremely small length scales and the dynamical instability for $|q| \gg c_2n$ is not measured by the mean-field theory [Fig. 3.11(b)].

Another extension of this work is to study the effects of the quench rate

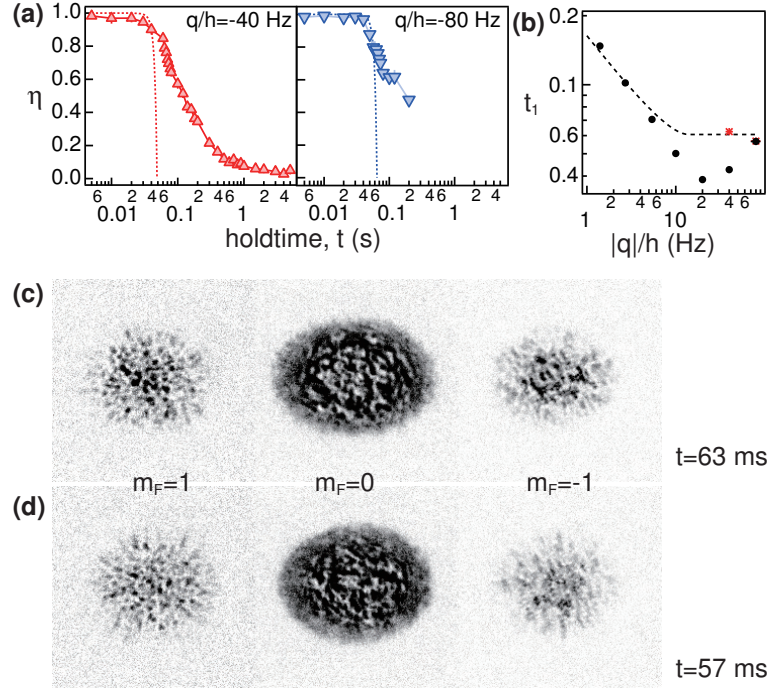


Figure 3.11: (a) Temporal evolution of η for $q/h = -40(2)$ and $-80(10)$ Hz. The dotted lines are guide lines for eyes. (b) shows the time t_1 , satisfying $\eta(t_1) = 0.8$ as a function of $|q|$. Black circles are calculated t_1 from the fitting function $1 - \eta(t) = \exp(\Gamma_q t)$ and red asterisks are experimentally measured t_1 from (a,b). The dashed line is the expected t_1 from the mean-field theory. Absorption images for each spin component at $t = t_1$ with $q/h =$ (c) 40 Hz and (d) 80 Hz, respectively.

across the critical point [81, 96, 100]. In particular, the power-law scaling of the HQV number after the quench is reminiscent of the Kibble-Zurek (KZ) mechanism [8–10]. We note that in the mean-field theory, the EAP-to-EPP phase transition is described as first order; thus, the conventional KZ mechanism, which involves a continuous phase transition, cannot be applied directly to our system. A generalization of the KZ mechanism could be studied with this system.

The turbulence of the spinor BECs represents a unique turbulence state where the mass and spin superflows are entangled. Previous turbulence studies with spinor BECs were mostly focused on the case with ferromagnetic spin interactions both experimentally [49, 52, 59, 101] and theoretically [102–104]. Our work demonstrates the peculiarities of the spin turbulence in an antiferromagnetic BEC, enabling a comparative study between the ferromagnetic and antiferromagnetic cases of the spin-1 BEC system [90, 91].

Chapter 4

The EPP-to-EAP phase transition

In this chapter, we introduce the opposite directional phase transition to the experiments in chapter 3, the EPP-to-EAP phase transition. Initially prepared multi-component BEC becomes a single component BEC through spin exchange collision losing the spin-degree of freedom, which is unique phenomenon for spinor BEC. The symmetry breaking of the nematic director in the EPP-to-EAP phase transition is similar to projected symmetry breaking in tachyon condensation [111].

We observe a composite-topological defects, which consists of a domain wall and HQVs. In this dissertation, the new type of a composite-soliton is named as a magnetic composite-soliton. Such a combined-topological defects are usually predicted to be formed in the interface of two quantum phases. During the inflation of early universe, complex interface physics can lead to complex walls bounded by strings and monopoles connected by strings [105].

It is extended to a He-3 superfluid system [106] and the experiments similar to the brane-antibrane annihilation have been performed [107]. Recently, a combined-topological defects in the interface between the ferromagnetic and the antiferromagnetic phases are suggested [109, 110].

Furthermore, according to Ref. [115], a magnetic composite-soliton mediates the KT transition from the normal gases to the exotic phase, called the paired superfluid, in an antiferromagnetic spin-1 condensate. The paired superfluid lies between the KT transition and the Ising transition. Thus, the observation of a magnetic composite-soliton is significant itself.

The magnetic composite-solitons have analogy to strings connecting point defects in the nematic liquid crystals [112] and θ -solitons combined with the spin-mass vortex in $^3\text{He-B}$ [113, 114]. The magnetic composite-solitons is allowed by the manifolds of order parameter, $[U(1) \times S^2]/\mathbb{Z}_2$, where the system is invariant under the transformation of $(\theta_n, \theta_s) \leftrightarrow (\theta_n + \pi, \theta_s + \pi)$. We focus on the structure of dynamically formed magnetic composite-soliton and its relaxation process after quench.

- Seji Kang and Yong-il Shin, “*Observation of magnetic composite-solitons in an quasi-2D antiferromagnetic spinor Bose-Einstein condensate*”, in preparation.
- Seji Kang and Yong-il Shin, “*Suppressing the amplification of the transverse spin fluctuations by the axial spin fluctuations*”, in preparation.

4.1 Dynamic instability for the EPP phase

Basics of the Bogoliubov theory is identical to section 3.1 and the instability of the initial EPP state is expected to show power-law scaling behavior of $|q|^{\frac{1}{2}}$ after the quench.

In case of the EPP phase, the field operator is given as

$$\hat{\Psi} = \begin{bmatrix} \psi_{+1} \\ 0 \\ \psi_{-1} \end{bmatrix} + \begin{bmatrix} \delta\hat{\psi}_{+1} \\ \delta\hat{\psi}_0 \\ \delta\hat{\psi}_{-1} \end{bmatrix}. \quad (4.1)$$

Due to the nature of antiferromagnetic interaction, the density fluctuation and spin fluctuations are coupled as

$$\hat{a}_{s_x, \mathbf{k}} = \hat{a}_{0, \mathbf{k}} \quad (4.2)$$

$$\hat{a}_{d, \mathbf{k}} = \frac{1}{\sqrt{2}}(\hat{a}_{1, \mathbf{k}} + \hat{a}_{-1, \mathbf{k}}) \quad (4.3)$$

$$\hat{a}_{s_z, \mathbf{k}} = \frac{1}{\sqrt{2}}(\hat{a}_{1, \mathbf{k}} - \hat{a}_{-1, \mathbf{k}}), \quad (4.4)$$

where $\hat{a}_{d, \mathbf{k}}$ describes the density fluctuation, and $\hat{a}_{s_x, \mathbf{k}}$ and $\hat{a}_{s_z, \mathbf{k}}$ describe the spin fluctuations around the x and z axes, respectively. In our experiments, we prepared the condensate with zero total magnetization ($p = 0$). So, the phonon and magnon excitations are decoupled. The Hamiltonian is expressed as

$$H = \frac{c_0 n^2 V}{2} + qN + \sum_{\mathbf{k} \neq 0} [(\epsilon_{\mathbf{k}} + c_0 n) \hat{a}_{d, \mathbf{k}}^\dagger \hat{a}_{d, \mathbf{k}} + \frac{c_0 n}{2} (\hat{a}_{d, \mathbf{k}}^\dagger \hat{a}_{d, \mathbf{k}}^\dagger + \hat{a}_{d, \mathbf{k}} \hat{a}_{d, \mathbf{k}})] \quad (4.5)$$

$$+ \sum_{\nu=s_x, s_z} \{(\epsilon_{\mathbf{k}} + c_2 n) \hat{a}_{\nu, \mathbf{k}}^\dagger \hat{a}_{\nu, \mathbf{k}} + \frac{c_2 n}{2} (\hat{a}_{\nu, \mathbf{k}}^\dagger \hat{a}_{\nu, \mathbf{k}}^\dagger)\} - q \hat{a}_{s_x, \mathbf{k}}^\dagger \hat{a}_{s_x, \mathbf{k}},$$

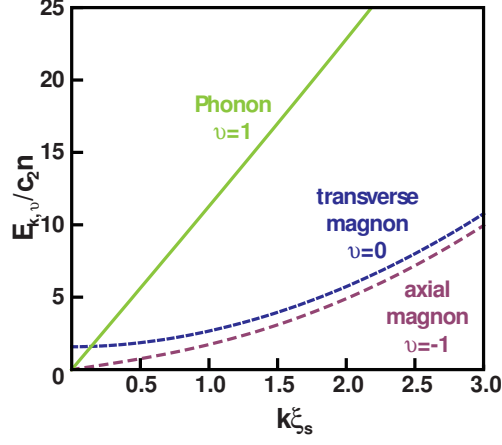


Figure 4.1: Bogoliubov dispersion relations in the EAP phase. There exist three modes of the excitation spectra-the phonon, the transverse magnon, and the axial magnon modes. Parameters: $c_2n = 14.7h$, $c_0n = 927h$ and $\xi_s = 2.0 \mu\text{m}$ corresponding to our experiment conditions, and $p = 0.5c_2n$, $q = -0.8c_2n$.

Apply a Bogoliubov transformations following

$$\hat{a}_{s_x,\mathbf{k}} = u_{0,k}\hat{b}_{0,\mathbf{k}} - v_{0,k}\hat{b}_{0,-\mathbf{k}}^\dagger \quad (4.6)$$

$$\hat{a}_{d,\mathbf{k}} = u_{+,k}\hat{b}_{+,\mathbf{k}} - v_{+,k}\hat{b}_{+,-\mathbf{k}}^\dagger \quad (4.7)$$

$$\hat{a}_{s_z,\mathbf{k}} = u_{-,k}\hat{b}_{-,\mathbf{k}} - v_{-,k}\hat{b}_{-,-\mathbf{k}}^\dagger \quad (4.8)$$

and we find that the energy spectra is given by

$$E_{+,\mathbf{k}} = \sqrt{\epsilon_{\mathbf{k}}(\epsilon_{\mathbf{k}} + 2c_0n)} \quad \text{associated with the phonon excitations} \quad (4.9)$$

$$E_{0,\mathbf{k}} = \sqrt{(\epsilon_{\mathbf{k}} - q)(\epsilon_{\mathbf{k}} + 2c_2n - q)} \quad \text{transverse magnon excitations} \quad (4.10)$$

$$E_{-,\mathbf{k}} = \sqrt{\epsilon_{\mathbf{k}}(\epsilon_{\mathbf{k}} + 2c_2n)} \quad \text{axial magnon excitations.} \quad (4.11)$$

These dispersion relation is described in figure 4.1. $E_{-,\mathbf{k}}$ is gapless. Thus, the thermal population of the axial magnon modes generate the spin fluctuations in the EPP condensate [41].

When $q > 0$, $E_{0,\mathbf{k}}$ becomes imaginary and leads to the transverse magnon excitations. The amplification of the transverse magnetization fluctuation induces the EPP-to-EAP phase transition. Because the energy spectrum of the transverse magnon mode is identical to that of the magnon modes in the EAP state (Eqn, 3.8), the instability rate $\Gamma_q = 2|E_{0,\mathbf{k}}|/\hbar \propto \sqrt{q}$. The characteristic time and length scales are also scaled as $1/\sqrt{q}$ for $q \ll c_2 n$.

4.2 Experimental setup & Methods

Preparation of initial condensate in the EPP state

The typical number of total ^{23}Na atoms are $\approx 6.8 \times 10^6$ and the fraction of normal gases is around 15%. The condensate is confined in the pancake-shaped optical dipole trap with $\omega_{x,y,z} = 2\pi \times (4.5, 6.3, 460)$ Hz and its Thomas-Fermi radii are $R_{x,y,z} = (201, 143, 2.0)$ μm . The condensate chemical potential $\mu = h \times 927$ Hz. Then, the DC magnetic field, B_z , adiabatically ramps down from 0.5 G to 52 mG. Sodium atoms are prepared in the superposition of $|F = 1, m_F = \pm 1\rangle$ states by $\pi/2$ spin rotation from the sample in the $|F = 1, m_F = 0\rangle$ state [Chap. 2]. The nematic directors are spatially co-aligned in x -direction [Fig. 4.3(a)]. We initiate the EPP-to-EAP phase transition by suddenly increasing q . Initial phase transition dynamics in the EPP sample can be explained by the mean-field theory in section 4.1. In order to keep the residual field gradient less than 0.1 mG/cm, q is tuned by the microwave dressing technique. In our experiment, q/h ranges from 1.2 Hz to 17 Hz much smaller than the condensate chemical potential and the spin healing length is $\xi_s \approx 4.5 \mu\text{m} < R_z$. Hence, the subsequent evolution after quench can be regarded as spin dynamics

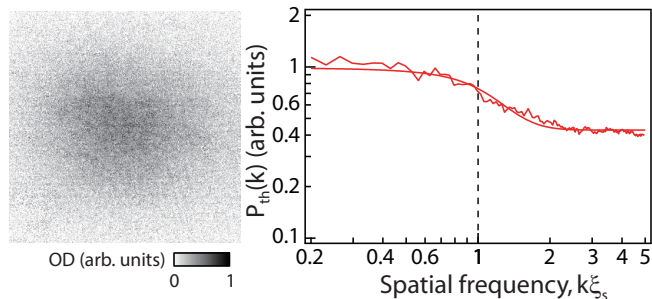


Figure 4.2: Right: Single *in situ* image of thermal gas. Left: Power spectrum of a trapped thermal gas at high temperature. The solid line is a sigmoid function fit with offset to the spectrum.

purely confined in 2 dimension.

Imaging methods

The spin texture of the condensate is examined by same methods in the former experiments of 24 ms TOF-SG imaging and spin-sensitive *in situ* phase-contrast imaging. We use the spin-sensitive phase-contrast imaging to display the axial magnetization distribution $M_z(x, y)$. In addition, by applying $\pi/2$ rf pulse, the transverse magnetization in one-direction, $M_x(x, y)$, is also taken.

Measuring the length scales of the magnon modes

We measure the power spectrum of the $m_z = 0$ density distribution, $P(k) = |\int d\mathbf{r} e^{i\mathbf{k}\cdot\mathbf{r}} \delta n_0^c(\mathbf{r})|^2$, where $\delta n_0^c(\mathbf{r}) = n_0^c(\mathbf{r}) - \bar{n}_0^c(\mathbf{r})$ is the density fluctuation of the $m_z = 0$ component. The power spectrum is obtained from at least 20 measurements. We subtract the average density distribution, $\bar{n}_0^c(\mathbf{r})$, from the column density $n_0^c(\mathbf{r})$ to remove uncontrolled modulations in the trapping potential. The power spectra for various q are extracted from the central $521 \mu\text{m} \times 521 \mu\text{m}$

regions of $m_z = 0$ absorption images, when $0.2 < 1 - \eta < 0.4$ [Fig. 4.5]. We display the power spectra in the narrow range of $k < 1/\xi_s$, where $P(k)$ s are not distorted by the limitation of our system's imaging sensitivity.

We measure the power spectrum of trapped thermal gas at high temperature [126, 127] and the noise power spectrum is displayed in Fig. 4.2. When the thermal wavelength is shorter than the imaging resolution, the noise power spectrum appear uncorrelated. Thus, the offset level in the high frequency region is determined only by the photon shot noise. However, our imaging resolution is at least $4.0 \mu\text{m}$, less than 2 pixels ($= 2 \times 2.58 \mu\text{m}$). Thus, the power spectra in the high frequency region contains not only the photon shot noise level, but also the atomic density signals.

4.3 Characterizing the quench dynamics

Figure 4.3 display image data sequences of the quenched condensate for $q/h = 10.4$ Hz. The EPP condensate becomes unstable for positive q , as the transverse magnon excited. Thus, atoms are transmuted into $m_z = 0$ spin state. In the early stage, the transition occurs coherently and the finite-size trapping geometry causes the ring-shaped transfer [45, 46]. Then, the condensate recovers close to its initial state in very short time about 60 ms. Then, the transition becomes complex. For hold time around 100 ms, very sharp domain walls and skyrmions appear and split into small scales in the subsequent evolution. At the end of the transition, singly-charged vortices are identified as the density-depleted holes in $m_z = 0$ absorption images.

The oscillatory behaviors in the early transition dynamics are not observed in the previous experiments on the EAP-to-EPP phase transition. We

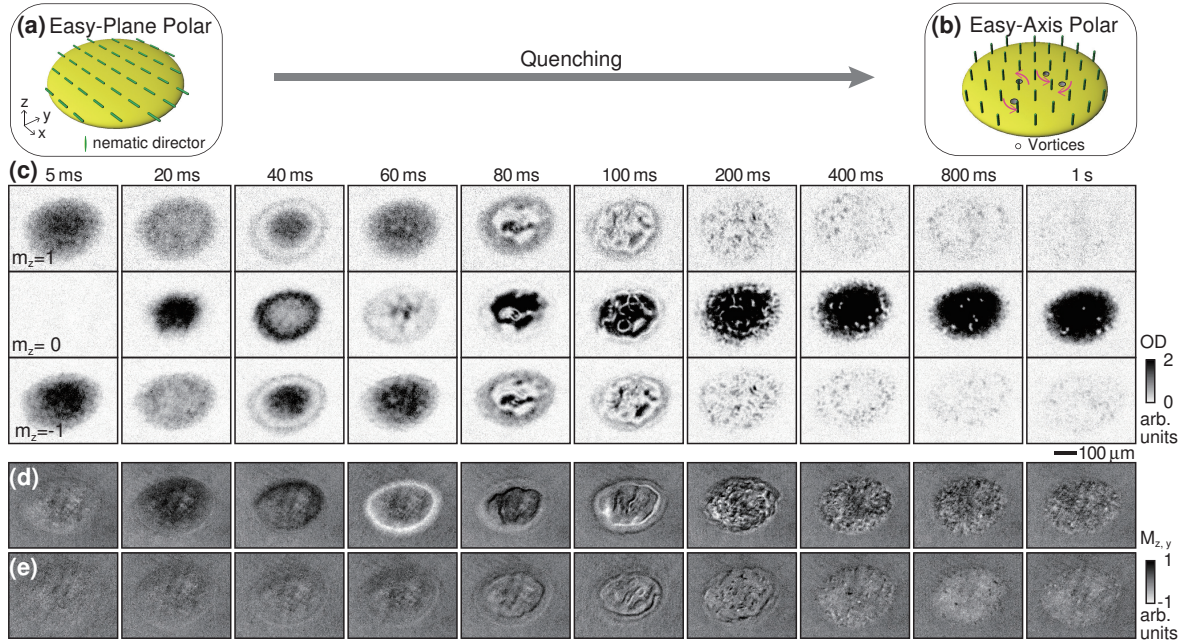


Figure 4.3: Phase transition from the EPP phase to the EAP phase of an anti-ferromagnetic spin-1 BEC. (a) The initial spin nematic director \vec{d} is coherently aligned in xy -plane and (b) the phase transition to the EAP phase is triggered by a sudden change of the quadratic Zeeman energy, q . (c) Absorption images of the $m_z = 1, 0, -1$ spin components after 24 ms Stern-Gerlach spin separation and (d) *in situ* transverse magnetization images in y -direction, $M_y(x, y)$, and (e) *in situ* axial magnetization images, $M_z(x, y)$, for various hold times t after the quench to $q/h = 10.4$ Hz. Quantum vortices with single mass circulation are identified with density-depleted holes in the $m_z = 0$ optical density images.

conjecture that the spin turbulence suppress the coherent oscillation. Instead, there exist a short loitering period at η_{th} (see section 3.4). Furthermore, when the EPP sample initially has spin fluctuations, the transition dynamics show no coherent oscillation. We will discuss this again in section 4.5.

4.3.1 Measuring the transverse magnon excitation

Small spin fluctuations in the transverse magnetization is amplified, inducing the EPP-to-EAP phase transition. These transverse magnon excitation is identified by the transverse magnetization images in Fig. 4.3(d). It is noted that the ferromagnetic spin components in the horizontal direction, M_x , are generated during the evolution. For a short time around 40 ms, the transition occurs coherently and the transverse magnetization is distributed in the ring-shaped manner. Even for long hold time over $t = 800$ ms, the transverse spin fluctuations still exist without vivid axial magnetization. This observation demonstrates that there exist sprinkled BECs in the $m_z = \pm 1$ states, where their density is too dilute to occur spin-exchange collision.

4.3.2 Time-Space scaling

We characterize the evolution of the quenched condensate by measuring the temporal evolution of the fractional population, $1 - \eta$, of the $m_z = \pm 1$ components. Here, η is the fraction of the $m_z = 0$ population, $\eta = N_0^c/N^c$, and $N^c = \sum_i N_i^c$, where N_i^c is the number of the condensate in the $m_z = i$ state ($i = 0, \pm 1$). The number of the condensate is determined from the SG images [Fig. 2.4.1].

We also measure the phase transition dynamics for extremely small $q \approx$

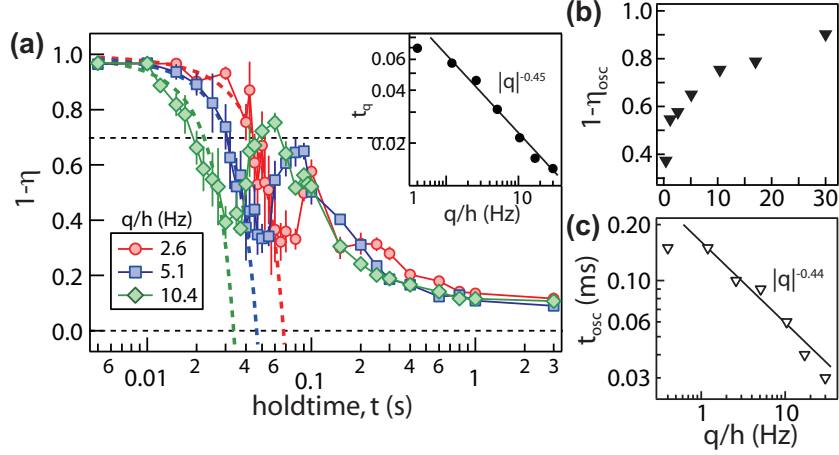


Figure 4.4: (a) Temporal evolutions of the fractional population $1 - \eta$ of the $m_z = \pm 1$ spin component in the condensate. Each data point was obtained by averaging at least five measurements, and its error bar denotes the standard error of the mean. The dashed lines are guide lines for eyes. The inset shows the time t_q for $1 - \eta(t_q) = 0.7$ as a function of q . The black line denotes a power-law fit to the data in the range of $h \times 1 \text{ Hz} < q < 2c_2n$. (b) The peak value of $1 - \eta$ oscillation and (c) its hold time are displayed as a function of q . The black solid line is a power-law fit to the data in the range of $h \times 1 \text{ Hz} < q < 2c_2n$.

$h \times 0.4 \text{ Hz}$ and for $q \approx h \times 30 \text{ Hz} \gtrsim 2c_2n$, but we analyze the data only in the range of $1 \text{ Hz} \leq q/h \leq 2c_2n$. It is predicted that the excited magnon modes for $q > 2c_2n$ have finite wave numbers and the quench dynamics might become different from that for other q values as we mentioned in previous section. For extremely small q value, the energy barrier between the $m_z = 0$ state and the superposition of the $m_z = \pm 1$ states is too low and no one knows exactly what happens near the critical point, $q = 0$. Hence, the spin dynamics near the critical point should be carefully treated.

The $1 - \eta$ decreases rapidly to ≈ 0.3 , then it increases to the peak value of $1 - \eta_{\text{osc}}$, keeping the coherence of the condensate. The early evolution of $1 - \eta$ is described by the exponential growth of the $m_z = 0$ population, represented

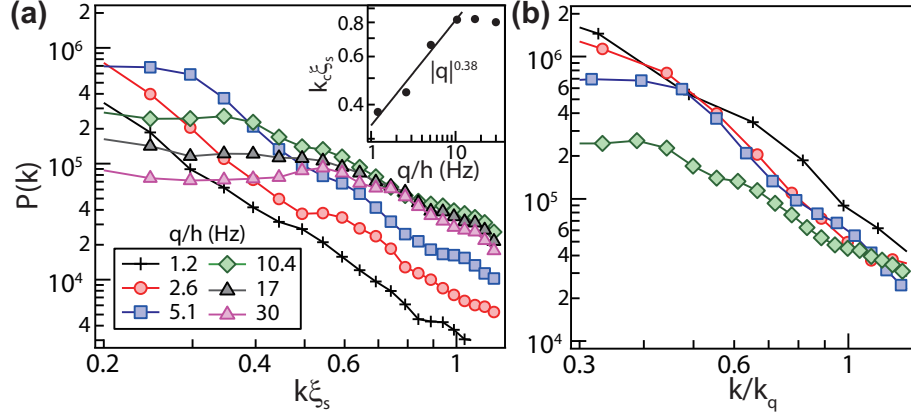


Figure 4.5: (a) Power spectra $P(k)$ of the $m_z = 0$ distribution of the quenched BEC in the range of $150 \text{ ms} \leq t \leq 250 \text{ ms}$ are displayed for various q . The inset shows the characteristic wave number, k_c , satisfying $P(k_c) = 5 \times 10^4$, as a function of q . The black line denotes a power-law fit. (b) Same power spectra to (a) are displayed as a function of rescaled k/k_q , with $k_q = \sqrt{2mq}/\hbar$ for various q .

as $\eta(t) = b \exp(\Gamma_q t)$, where b is a constant determined by the magnitude of the magnetization fluctuations.

From the excitation of the dynamically unstable magnon modes, the instability rate, Γ_q , is proportional to \sqrt{q} . We fixed $b \approx 0.0053$ from the least-squares fitting. In the inset of Fig. 4.4(a), we display the time t_q measured for $1 - \eta(t_q) = 0.7$ as a function of q . A power-law fit to the experimental data in the range of $1 \text{ Hz} \leq q/h \leq 20 \text{ Hz}$ gives an exponent of -0.45 ± 0.04 , which is in quantitatively good agreement with the predicted scaling of $1/\sqrt{q}$. The oscillatory transfer is described by the amplitude of $1 - \eta_{\text{osc}}$ and the peak time, t_{osc} . The $1 - \eta_{\text{osc}}$ increases from ≈ 0.6 for $q/h = 1.2 \text{ Hz}$ to ≈ 0.8 for $q/h = 17 \text{ Hz}$. The t_{osc} shows identical power law of -0.44 ± 0.05 to $t_{0.7}$, manifesting that the early spin dynamics is coherently sustained. Then, $1 - \eta$ decreases following a single decay curve regardless of q .

To investigate the length scales of excited magnon modes, we measure the power spectrum of the density-density correlations of the $m_z = 0$ atom clouds, $P(\mathbf{k}) = \left| \int d\mathbf{r} e^{i\mathbf{k}\cdot\mathbf{r}} \delta n_0^z(\mathbf{r}) \right|^2$, when $1 - \eta \approx 0.3$. The spectral slopes are almost identical and the characteristic wave number increases depending on the quench depth, q . The power spectra collapse into a single line with rescaled k/k_q for $q \geq c_2 n \approx 14.7$ Hz, where $k_q = \sqrt{2mq}/\hbar$. We characterize the characteristic wave number as the wave number, k_c , satisfying $P(k_c) = 5 \times 10^4$. The inset of Fig. 4.5(a) shows the scaling of k_c with the exponent of 0.38 ± 0.05 , which is marginally smaller than the predicted power-law of 0.5^1 . This might be the quenched condensate for long hold time over 100 ms contains various decay process such as the domain coarsening dynamics and the vortex-antivortex annihilation. For $q > c_2 n$, the power spectra overlaps. This is because that the spin healing length limits the minimum size of $m_z = 0$ domains [96].

4.4 Dynamically formed topological objects

Interestingly, we observe long-lived topological defects over 500 ms. Generally, the topological defects, created via the sudden phase transition, are understood by the quantum noise seeds [7, 11, 117, 118]. This explains the formation of singly charged vortices as a result of the quenched phase transition, which will be discussed in section 4.6. However, our observation is beyond the understanding of either the phase-ordering kinetics or the symmetry of an antiferromagnetic spinor BEC.

Thanks to the $[U(1) \times S^1]/\mathbb{Z}_2$, various topological defects can be formed

¹The exact exponent should be obtained without the technical issues such as the aliasing [116].

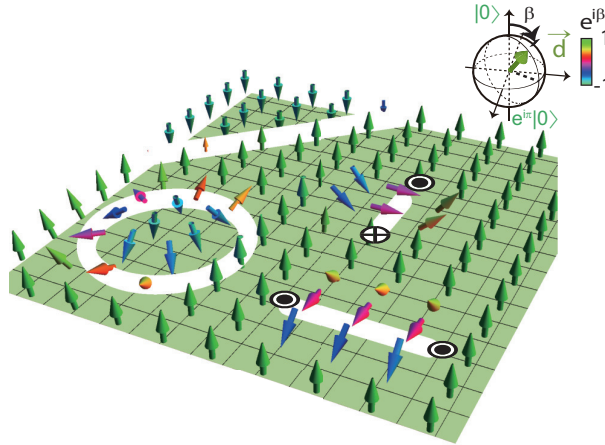


Figure 4.6: Schematic description of the topological defects such as skyrmions, line solitons and magnetic composite-solitons. The nematic directors are indicated as arrows. The tilted angle along z -axis, β , represents local spin phases. \otimes (\odot) indicates the clockwise (counterclockwise) superflow.

as in Fig. 4.4 such as skyrmions, HQVs, and domain walls. But, we also observe a new kind of topological defects, named as magnetic composite-soliton. A magnetic composite-soliton consist of two different topological defects, a domain wall and HQVs. The combined-topological defect is investigated in terms of its formation process and structure between the spatially separated two quantum phases [105, 107, 109, 110]. In our experiments, the manifolds of ferromagnetic and antiferromagnetic order parameters are mixed and a magnetic composite-soliton can be understood in the full symmetry of spin-1 BEC, which is given by $U(1) \times SO(3)$.

We can imagine that the nematic director, initially aligned in x -direction, stands vertically as $\mathbf{d} \parallel \hat{z}$, at the end of dynamics, choosing either negative or positive rotational direction. When two domains in contact have the phase difference of π , the domain walls can be created in the interface. The domain walls can be regarded as bright-dark-bright (BDB) solitons [119], where the dark

soliton resides in the $|m_F = 0\rangle$ state and the bright solitons in the $|m_F = \pm 1\rangle$ states. The BDB solitons are formed in the 2D system, which are extended from the realization of the three component solitons in 1D ferromagnetic spinor BEC [120, 121]. The solitons are allowed by the nature of antiferromagnetic interactions. Thus, the alignment of the nematic directors across a soliton changes continuously from \mathbf{d} to $-\mathbf{d}$. In principle, these solitons have no magnetization, but they are also discernible in the axial magnetization-sensitive *in situ* images. We attribute this slight phase-separation to the uncontrollable edge enhancement of phase-contrast imaging, the imperfect cancelation of magnetic field gradient and the subtle discrepancy between the $m_z = \pm 1$ atom numbers [122].

For smaller q/h , the length scale of magnon excitations, l_q becomes large as $l_q = 2\pi\hbar/\sqrt{2mq}$. Thus, we can selectively create a single soliton under the condition of $R_{xy}/l_q \approx 2.5$ [Fig. 4.7]. The possible spatial spin distributions are also displayed as cartoon images. The sharp magnetic composite-soliton and skyrmion images are taken by 1 \sim 2 out of 10 runs. When the spin fluctuations are enhanced by the excitation of the axial magnon modes in the EPP condensate (see section 4.5), magnetic composite-solitons are formed more frequently with same q/h values, satisfying $R_{xy}/l_q \approx 2.5$ (Compare to Fig. 4.15). In the future, we could investigate the stability of skyrmions.

A large BDB soliton across the whole condensate bends because of the snake instability [123–125] and splits. At the end of the soliton, there should exist HQVs, having both spin and mass currents. The existence of spin currents is easily confirmed by the sharp domain walls in the spin-separated absorption images and their spin texture in Fig. 4.4 and Fig. 4.7(g-l). To explore the mass current, we use Bragg spectroscopy techniques to the condensate, consist of the $m_z = 0$ component and discuss the result in the next section.

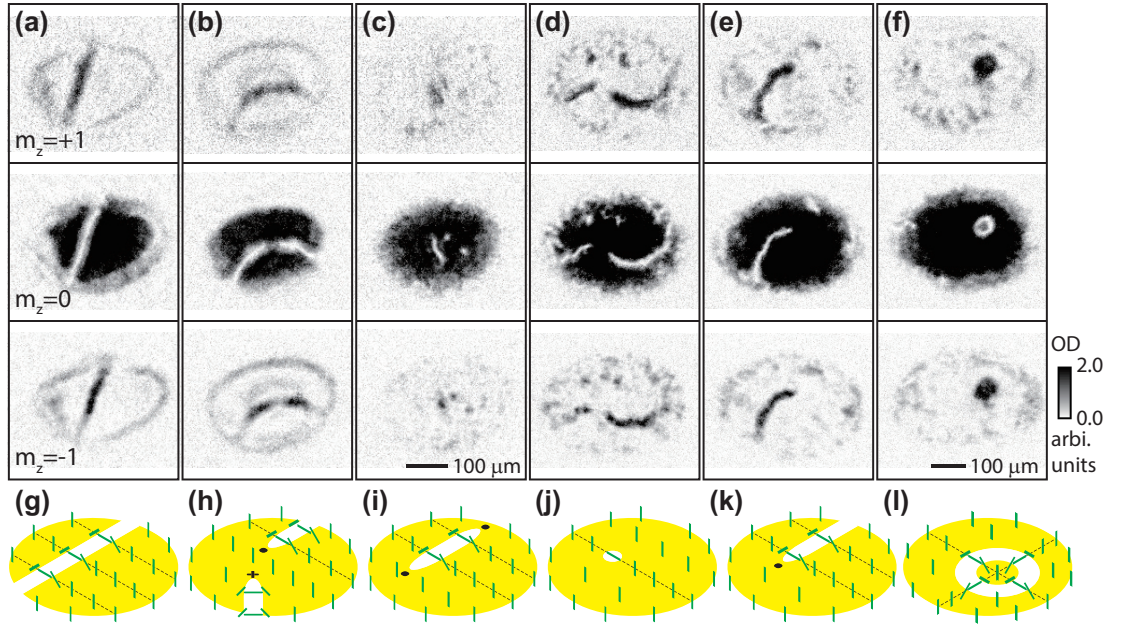


Figure 4.7: Dynamically formed (a-e) magnetic composite-solitons and (f) a skyrmion with $q/h =$ (a-c) 2.6 Hz and (d-f) 1.0 Hz. The evolution times are (a) 300 ms, (b) 200 ms, (c, f) 600 ms, and (d) 400 ms, and (e) 700 ms, respectively. Absorption images are taken after 24 ms spin separation. (g-l) Example of spin textures. Experiments conditions: (a-c) initial $\mu \approx h \times 880$ Hz, $c_2n = 14h$ and $\mathbf{R}_{TF} = (232, 160, 2.2)$ μm . (d-f) initial $\mu \approx h \times 927$ Hz, $c_2n = 14.7h$ and $\mathbf{R}_{TF} = (201, 143, 2.0)$ μm .

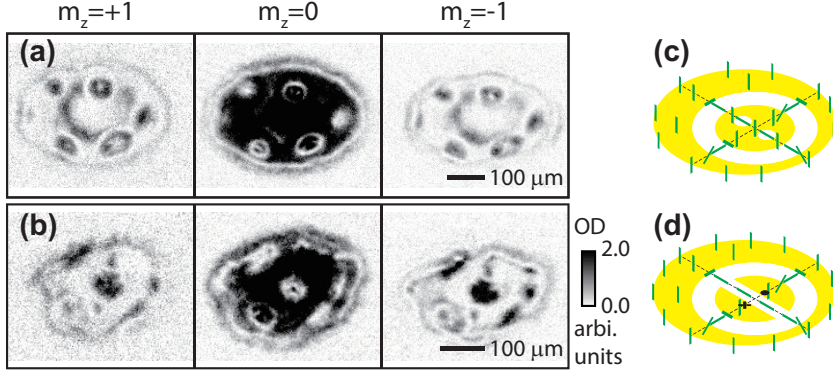


Figure 4.8: Dynamically formed hog-nosed spin structures with $q/h =$ (a) 2.0 Hz and (b) 5.1 Hz. The evolution times are 200 ms. Absorption images are taken after 24 ms spin separation. (c, d) Example of spin textures. Experiments conditions: (a-c) initial $\mu \approx h \times 880$ Hz, $c_2 n = 14h$ and $\mathbf{R}_{TF} = (232, 160, 2.2) \mu\text{m}$. (d, e) initial $\mu \approx h \times 927$ Hz, $c_2 n = 14.7h$ and $\mathbf{R}_{TF} = (201, 143, 2.0) \mu\text{m}$.

Before embark on the next section about the Bragg spectroscopy for a magnetic composite-soliton, I briefly mention about an intriguing spin structures in Fig. 4.8. Hog-nosed spin structures are formed for every single sequence under the condition of $R_{xy}/l_q \approx 5$. It is alluring results that the formation of topological objects is determined by the interwinding between the excitations of unique magnon modes and the finite size of a condensate. I describe the nematic director distribution, but it needs more theoretical works to understand these structures. For more images, see section 4.7.

4.4.1 Magnetic composite-soliton: a domain wall terminated by HQVs

Here, we concentrate on the evolution of a magnetic composite-soliton, having HQVs at the endpoints. A HQV has the fractional supercurrent circulation of $h/2m$ with the aid of the half spin-winding [Chap. 1]. In this section, we

introduce Bragg spectroscopy techniques, referred to [128], and experimental sequence. Then, we discuss about the mass current encircling magnetic-composite soliton.

Bragg spectroscopy with spin separation

When a BEC having mass flow, \vec{v} , is irradiated by a pair of counterpropagating laser beams, a two-photon process imparting moment \vec{q} and energy ε to an atom occurs under the resonant condition of $\varepsilon = \frac{q^2}{2m} + \vec{q} \cdot \vec{v}$. Here, $\vec{q} = 2\hbar k_L \hat{x}'$ and $\varepsilon = \hbar\delta$, where k_L and δ are the wave number and frequency difference of the two beams, respectively. Because of the Doppler effect, the scattering response in a BEC having a circulation is asymmetric with respect to the Bragg beam, and the vortex sign can be determined from the position of the scattering region relative to the vortex core. For supercurrent with counterclockwise half-circulation, the velocity is given by $\vec{v} = (\hbar/2mr^2)\hat{z} \times \vec{r}$, where \vec{r} is the position relative to the vortex core as the origin, the resonant condition is given by $\delta_d = \delta - \delta_0 = -(\hbar k_L y' / mr^2)$, where $\delta_0 = 2\hbar k_L / m$. See Fig. 4.9(d) and Fig. 4.10.

We spatially overlap the two laser beams with frequencies ω_L and $\omega_L + \delta$. The frequency difference δ is generated by the two independently controlled acousto-optic modulator (AOM). Two pairs of Bragg beams are the red-detuned laser beams from the $|F = 1\rangle$ to $|F = 2'\rangle$ transition. The $1/e^2$ width of each beam is $1.8 \text{ mm} \gg R_{xy}$ and each beam has intensity of $I = 2.9 \text{ mW/cm}^2$.

In order to identify the spin distribution and the mass current simultaneously, we inject Bragg beams with 15 ms spin separation. We first turn off the optical dipole trapping potential and apply a residual field gradient for $200 \mu\text{s}$. Then, a pair of counterpropagating Bragg beams is applied to the sample for

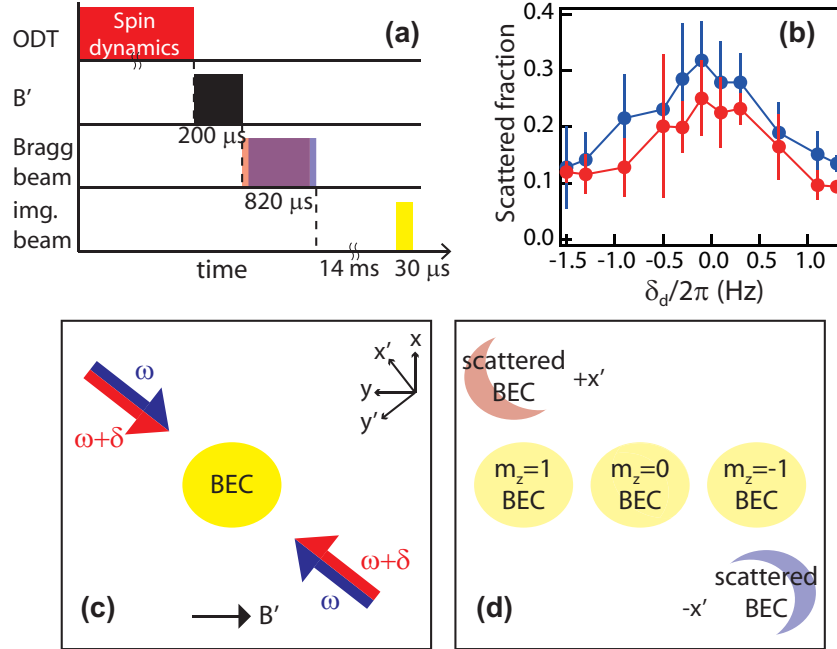


Figure 4.9: (a) Schematic of the Bragg spectroscopy and SG imaging sequence. Two atomic clouds are scattered outward from the $m_z = 0$ BEC in the $\pm x'$ directions. (b) Scattered-out atom number fractions measured for a stationary $m_z = 0$ BEC as a function of δ_d without SG imaging Sequence. $\delta_d = \delta - \delta_0$, where $\delta_0 = 99.0$ kHz. The blue and red circles denote the atom number fractions of the red and blue atom clouds in (d), respectively. (c) The directions of two pairs of counterpropagating Bragg beams (blue and red arrows), and spin separation (black arrow). (d) Schematic illustration of Bragg spectroscopy with spin separation imaging in CCD.

820 μs . After 14 ms time-of flight, an absorption image is taken. The experimental sequence is described in Fig. 4.9. The Bragg spectrum of a stationary $m_z = 0$ BEC is obtained by measuring the fractional population of the scattered clouds as a function of δ [Fig. 4.9(b)]. The center frequency is experimentally measured as $\delta_0/2\pi = 99.0$ kHz.

Measuring the mass current at the ends of MCSs

By using this methods, we can identify the position and the polarization of HQVs at the endpoints of the MCS, simultaneously. We set the detuned frequency at $\delta_d = -0.9$ kHz from the resonance frequency, δ_0 , for a stationary $m_z = 0$ condensate. A Bragg signal is constructed with the $S_B(x', y') = n_+(x', y') - n_-(x', y')$, where $n_{\pm}(x', y')$ are the $\pm x'$ -scattered densities, respectively.

Figure 4.10 displays the Bragg signals corresponding to the respective spin separated absorption images. Note that the clear counterclockwise supercurrent signal at the end of a MCS in Fig. 4.10(d). The density is dilute around the endpoint of a MCS, because atoms are scattered by the Bragg beams. In addition, there exist the opposite mass currents between the two MCSs in Fig. 4.10(e,f). This is the evidence of soliton splitting process, inferring that these two MCSs originally make up of a single BDB soliton.

A sharp endpoint of a composite-soliton, transferring mass flows, is possible to lead the rotational motion and its shape becomes spiral-like. In recent studies [129], it is suggested that a dark soliton carrying the effective fractional supercurrent can be created in a scalar BEC. Due to the mass velocity, the dark soliton becomes spiral-shaped, leading to the snake instability. One can recognize the slight curvature at the end of MCSs in Fig. 4.7(d,f) and Fig. 4.10(a-c). It

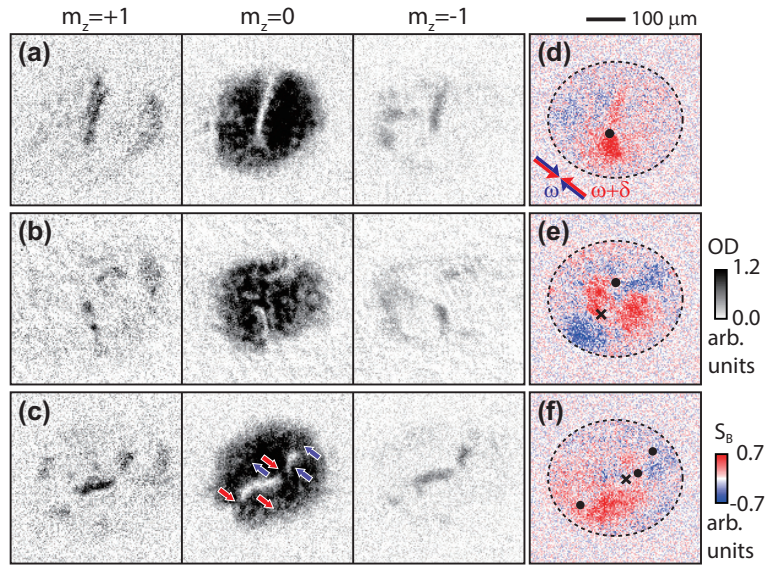


Figure 4.10: Bragg spectroscopy and spin separation imaging of a BEC with MCSs for $q/h = 2.6$ Hz for 600 ms hold time. (a-c) Absorption images for each spin components and (d-f) the corresponding Bragg signals $S_B(x', y') = n_+ - n_-$, where n_+ and n_- are the density distributions of the $+x'$ - and $-x'$ -scattered atom clouds, respectively. $\delta_a/2\pi = -0.9$ kHz. The circles and crosses denote the sign of mass flow. Small arrows in (c) represent the direction of supercurrents.

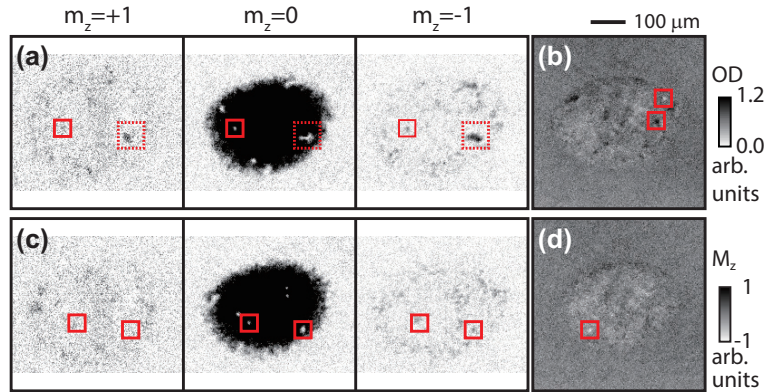


Figure 4.11: Singly charged vortices having magnetized cores. (a,c) Spin separated absorption images and (b,d) *in situ* are taken after (a,b) 800 ms and (c,d) 1 s hold times. The final q values are $q/h =$ (a,b) 5.1 Hz and (c,d) 10.4 Hz, respectively. Red boxes mark quantum vortices with magnetized cores. Dotted boxes mark a domain wall with unbalanced spin population.

is natural to derive the conclusion that the orientation of mass current is counterclockwise for Fig. 4.7(f). We also conjecture that the mass flows between MCSs in Fig. 4.7(d) are identical to that in Fig. 4.10(e).

Singly charged quantized vortex with a magnetized core

At the end of phase transition, singly charged quantum vortices are identified with density-depleted holes in the density of the $m_z = 0$ atoms. Quantum vortices are mainly formed by the phase differences in the interface of local domains. The scaling of HQVs are mentioned in section 4.6.

Interestingly, some of quantum vortices have vivid ferromagnetic cores. We can recognize these quantized vortices in both absorption images for each spin components and axial magnetization images [Fig. 4.11]. The formation of a quantized vortex with a magnetic core which are not fully explained by local quantum seeds. One possible scenario is that the shrinking of a soliton

possessing imbalanced $m_z = \pm 1$ spin populations in its domain wall part. When the winding of the supercurrent encircling both edges of the soliton is 2π , the MCS is able to become a singly charged vortex. The example is displayed in Fig. 4.10(c,f).

Most of singly charged vortices have either empty cores or cores, which is filled with the equal the $m_z = \pm 1$ populations. This is because that we prepared the sample with zero magnetization. We attribute the imbalanced spin population in a vortex core to the discrepancy of the coupling strength of the microwave fields for each spin state. In our experiments, the lifetime of the $m_z = +1(-1)$ atom is usually shorter than that of the $m_z = -1(+1)$ atoms for blue-detuned(red-detuned) frequency from the $|F = 1\rangle \leftrightarrow |F = 2\rangle$ transition. Spin phase separation, induced by a slight magnetic field gradient, might be another reason.

In Fig. 4.11(a,c), a MCS has both spin components, but magnetic core-vortices have either $m_z = 1$ or -1 spin population in its cores. This might be because the system avoids the $m_z = \pm 1$ states and the spin-exchange collision occurs lowering the system's energy. As the same reason, a quantum vortex with a ferromagnetic core would be expelled in the boundary region of a condensate.

4.5 Suppression of dynamical instability by the axial spin fluctuations

In contrast to the EAP condensate, the EPP condensate can be thermally excited from the thermal population of the magnon modes. Right after the spin

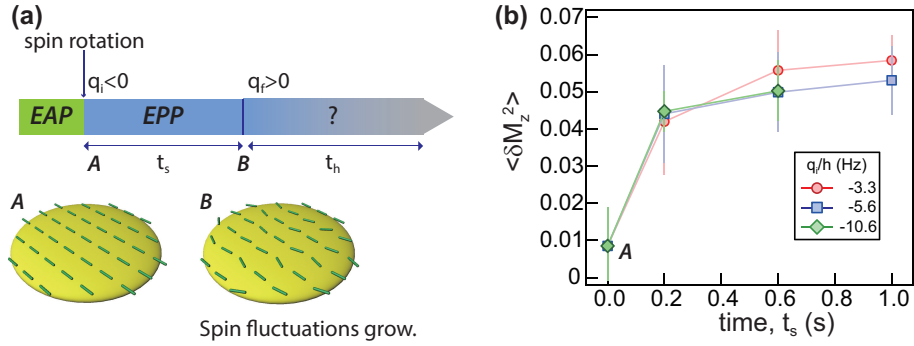


Figure 4.12: (a) Experimental sequence to enhance spin fluctuations in an EPP condensate. **A**: An EPP condensate is prepared by the spin rotation. **B**: Spin fluctuations arise for t_s from the thermal population of axial magnon modes with $q_i < 0$. Then, we change the final quadratic Zeeman energy, q_f , to the positive value. (b) Variance of the axial magnetization, $\langle \delta M_z^2 \rangle$, as a function of t_s . $\langle \delta M_z^2 \rangle$ is measured from the $157 \mu\text{m} \times 157 \mu\text{m}$ center region of *in situ* magnetization images. The error bars are the standard deviation of more than 5 measurements. The growth of spin fluctuations are independent to the magnitude of q_i .

rotation, the nematic directors are co-aligned to the x -direction as in Fig. 4.12 **A** with zero temperature. We call the EPP condensate without any spin fluctuations as an either uniformly-aligned or coherent EPP condensate. The spin fluctuations develop with the gapless magnon excitations. We characterize the spin fluctuations by the axial magnetization variance, $\langle \delta M_z^2 \rangle$ [Fig. 4.12(b)]. The growth rates are irrelevant to the quadratic Zeeman energy, $q_i < 0$, which is obvious result. Then, the nematic directors tremble in xy -plane [Fig. 4.12 **B**]. We call the EPP condensate at **B** as a faltering EPP condensate. Because our system is in the spin-wise 2D, the spin fluctuations could be more enhanced. It might be done by building a true 2D trapping potential and overcoming the limitation of the condensate's short lifetime due to the heating of the microwave dressing.

We explore the properties of 2D spin dynamics by enhancing the spin

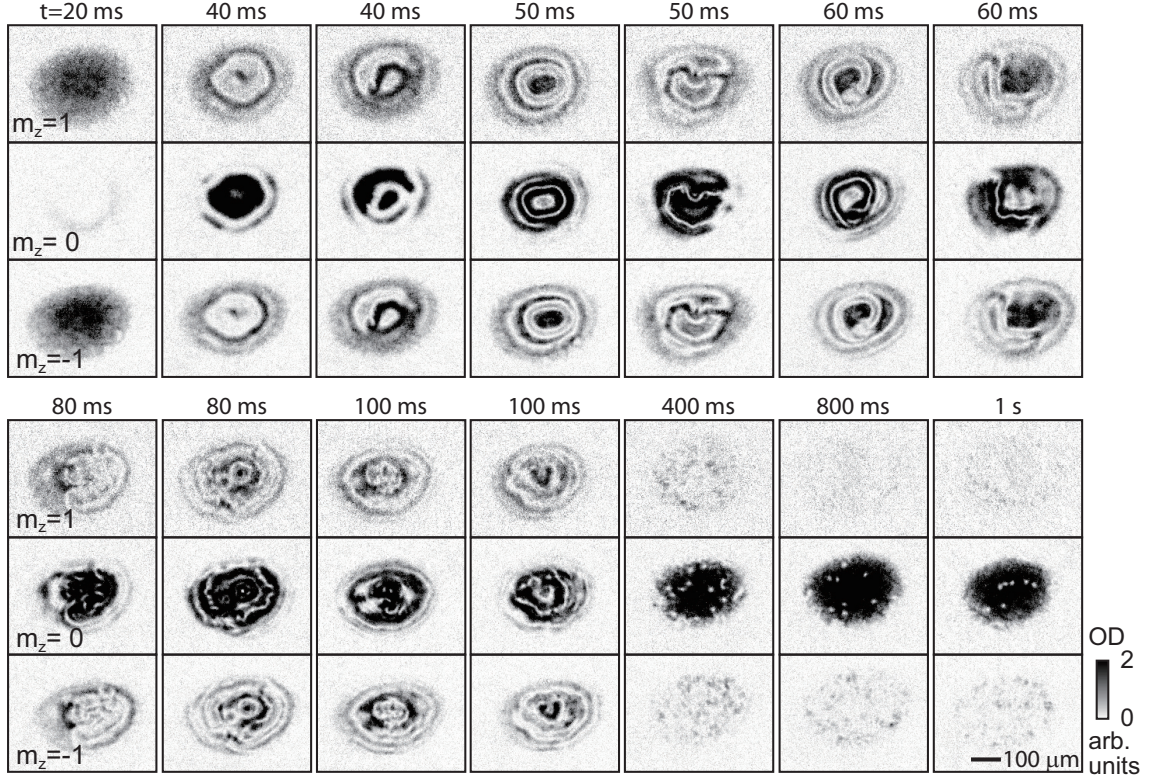


Figure 4.13: Temporal evolution of the quenched EPP condensate with the spin fluctuations for $q/h = 10.4$ Hz. (a) The initial spin nematic director \vec{d} is coherently aligned in xy -plane and (b) the phase transition to the EAP phase is triggered by a sudden change of the quadratic Zeeman energy, q . (c) Absorption images of the $m_z = 1, 0, -1$ spin components after 24 ms Stern-Gerlach spin separation and (d) *in situ* transverse magnetization images in y -direction, $M_y(x, y)$, and (e) *in situ* axial magnetization images, $M_z(x, y)$, for various hold times t . Quantum vortices with single mass circulation are identified with density-depleted holes in the $m_z = 0$ optical density images.

fluctuations and measuring the dynamical instability of the EPP-to-EAP phase transition. We generate the spin fluctuations in the EPP condensate for t_s , then suddenly change the quadratic Zeeman energy from $q_i < 0$ to $q_f > 0$. The jump from q_i to q_f is implemented within 1 ms (for more information, see Appendix C), which is much shorter than the spin-interaction time of $1/c_2n \approx 68$ ms.

In an intuitive thinking, one might assume that a faltering EPP condensate becomes more dynamically unstable at $q_f > 0$, because its temperature is higher than that of a coherent EPP condensate. In addition, the number of quantum noise seeds might be larger for a faltering EPP condensate. Figure 4.13 shows the temporal evolution of a quenched EPP condensate with the spin fluctuations for $q/h = 10.4$ Hz. We recognize that the characteristic length of the transverse magnon modes is shorter and the widths of solitons become sharper, compared to Fig. 4.3. In addition, the coherent ring-shaped transfer is not clear as in Fig. 4.3. This manifests that the number of local EAP domains increase in case of a fluctuating EPP condensate at positive q_f . However, the delay time of the early dynamics increases as more spin fluctuations are generated in a EPP condensate, where the first assumption appears to be wrong.

The suppression of the transverse magnon excitation is described by the change of the fractional population in Fig. 4.14. The coherent oscillation is clearly suppressed. Instead, the rapid decay of $1 - \eta$ is halted at a certain $1 - \eta_{\text{th}} \approx 0.5$. Then, it follows a single decay line regardless of the condensate's initial condition. This behavior of $1 - \eta$ is much similar to the evolution of the fractional population through the EAP-to-EPP transition in Fig. 3.5. In addition, the dynamic instability is diminished for a faltering EPP condensate. Recent study, referred to Ref. [130], suggests that the dynamical instability can

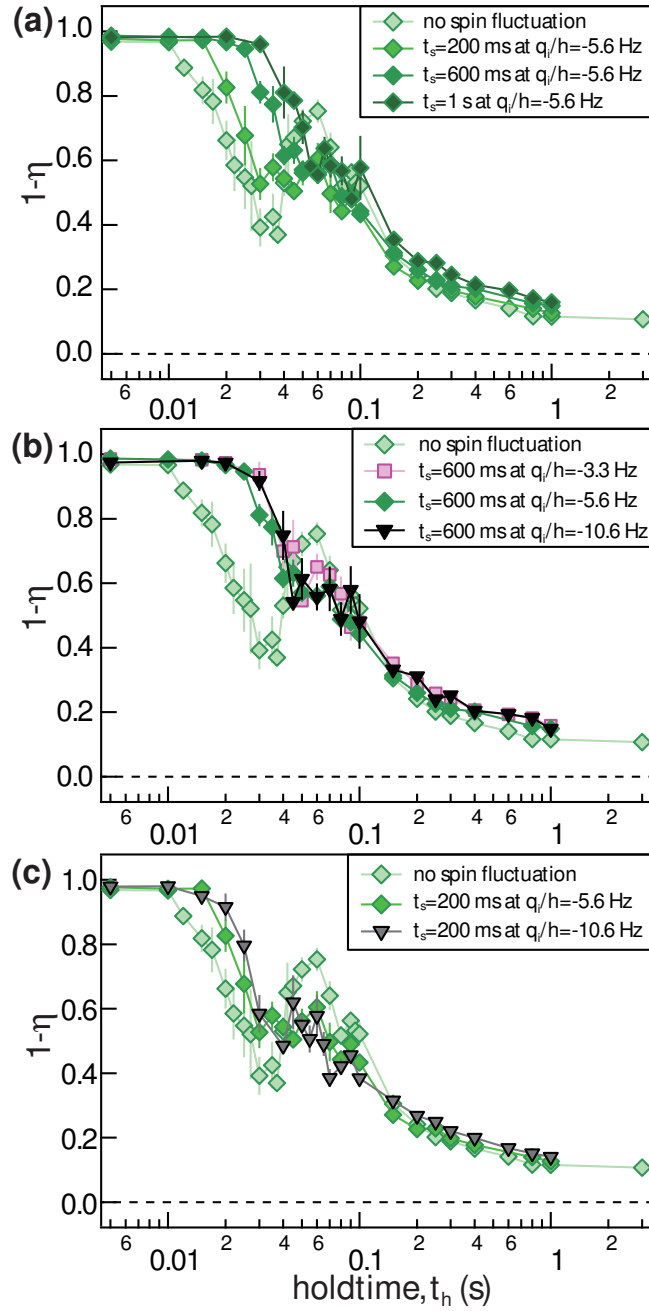


Figure 4.14: Quantum vortex number, N_v , versus q . N_v was measured by counting density-depleted holes in the SG images of the $m_z = 0$ spin components. Each data point is the average of 13 measurements for the same experiment and its error bars indicates the standard error of the mean. The blue dashed line is a power-law fit to the data.

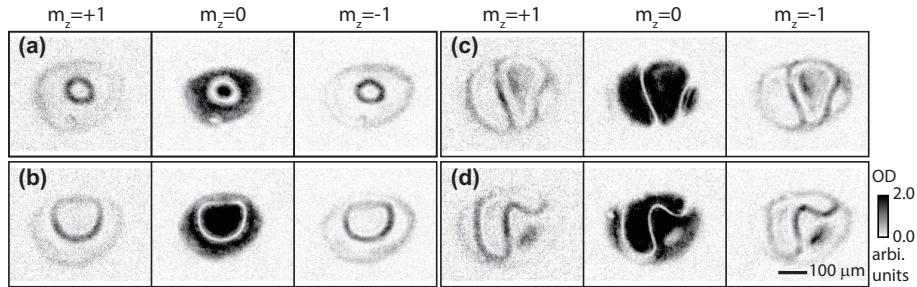


Figure 4.15: Dynamically formed (a,b) skyrmions and (c,d) magnetic composite-solitons with $q/h = 2.6$ Hz. The spin fluctuation is enhanced for 600 ms and the evolution times after quench are 150 ms. Absorption images are taken after 24 ms spin separation. Experiments conditions: initial $\mu \approx h \times 927$ Hz, $c_2 n = 14.7h$ and $\mathbf{R}_{\text{TF}} = (201, 143, 2.0)$ μm .

be tuned by the spin-squeezing. However, in our experiments, the transverse magnon modes are totally independent to the axial magnon modes. Instead, it infers that the coherent EPP state is not a true ground state for many-body quantum system, even the coherent EPP condensate is well described by the mean-field theory. Based on the inference, intriguing questions naturally arise: what is the true ground state for the many-body antiferromagnetic spin-1 Bose system at negative q , and whether the dynamic instability lessens infinitely or not near the critical point. We hope to find the theoretical and experimental ways to answer the above questions in the future.

4.6 Creation of singly charged vortices

Because the coherence over the whole sample does not exist with the spin fluctuations, a magnetic composite-soliton is formed more frequently in a faltering EPP condensate across the EPP-to-EAP transition: skyrmions and domain walls are formed for every experimental run. From the comparison of

Fig. 4.15 to Fig. 4.7(a-d), we recognize that the domain walls are bendy and narrow. The formation of MCS and skyrmions are influenced by the quantum fluctuation seeds, in other words, the population of non-condensed $m_z = 0$ component.

The topological defects, created as a result of a phase transition, reflect the number of the quantum noise seeds. At long hold times, $t \geq 1$ s, a singly charged vortices are vividly identified with the density-depleted holes in the $m_z = 0$ absorption images. We measure the number of quantized vortices, N_v [Fig. 4.16]. When we prepare the uniformly aligned EPP condensate, N_v increases with increasing $q \lesssim c_2 n$ with the power-law exponent of 1.3 ± 0.2^2 , which is predicted from $N_v \propto l_q^{-2}$ and the spatial size of the magnon modes, $l_q \propto \sqrt{q}$. For $q > c_2 n$, N_v slowly increase with q [96]. When we prepare the faltering EPP condensate, the number of quantum vortices is saturated for $q \leq 5.1$ Hz, supporting that the temperature of a condensate increases the number of quantum noise seeds.

4.7 Sad history

When I firstly conducted experiments about the EPP-to-EAP phase transition dynamics, the number of a condensate was about 8.0×10^6 and the thermal fraction was less than 10 %. Thus, the sample size was large enough to contains a lot of dynamically formed topological defects, including magnetic composite-solitons as displayed in Fig. 4.17 and Fig. 4.18. The life-time of a condensate was long enough to measure the decay dynamics of quantized vortices for long

²It can be regarded as the quadratic Zeeman energy is converted into the kinetic energy of a condensate via the spin-change collision.

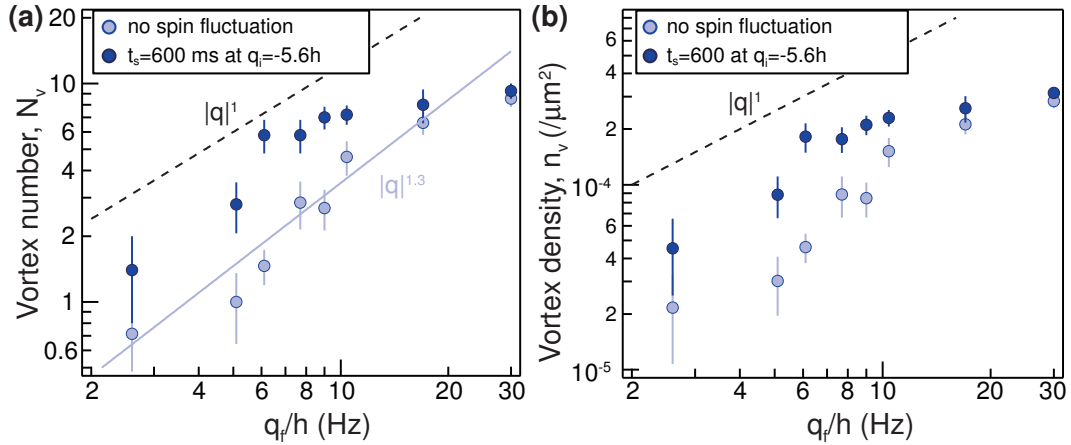


Figure 4.16: Quantum vortex number, N_v , versus q . N_v was measured by counting density-depleted holes in the SG images of the $m_z = 0$ spin components. Each data point is the average of 13 measurements for the same experiment and its error bars indicates the standard error of the mean. The black dashed line is a power-law guide line and the blue solid line is a power-law fit to the light blue data for $q/h \leq 17$ Hz.

hold times, $t_h = 5$ s.

However, the control switch, connecting between the microwave function generator and RF coils, was malfunctioning and unwanted microwave dressed fields disturbs the preparation of the uniformly aligned EPP condensate. So, I did not know the amplitude of the spin fluctuations and these images show the temporal evolutions of a quenched EPP condensate with the axial spin fluctuations. It was the reason why the sample contains a lot of quantized vortices.

Unfortunately, after I realized and fixed the switch problem, the number of a BEC decreased and the lifetime became shortened for some reasons. I wish I knew the reasons.

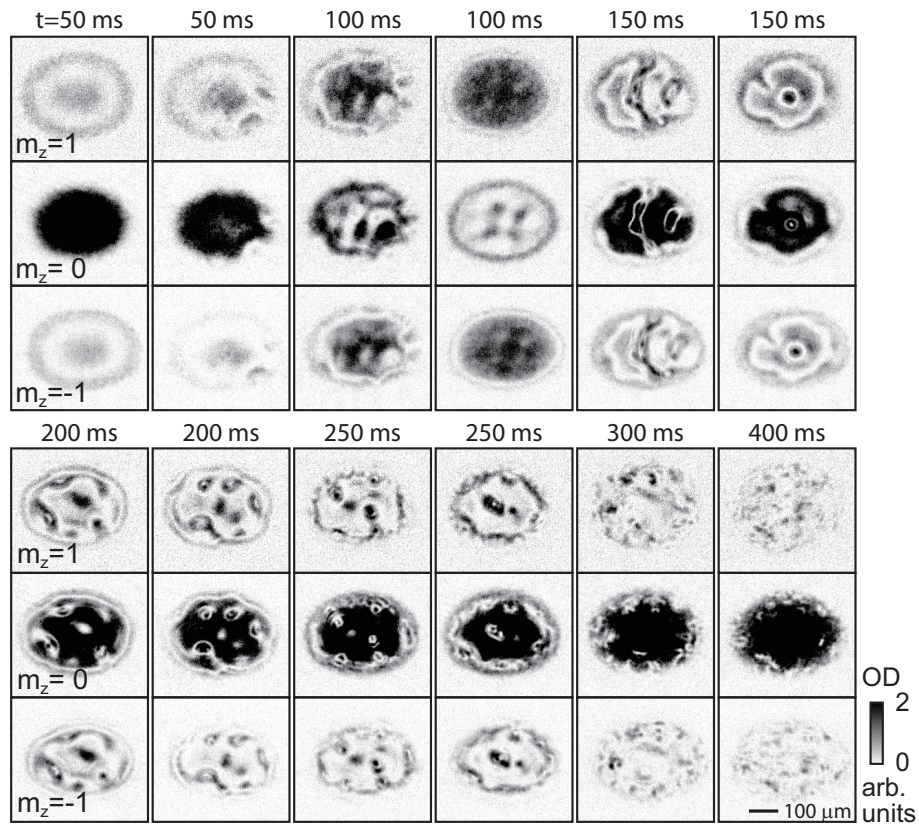


Figure 4.17: Phase transition from the EPP phase for $q/h = 2.0$ Hz. Absorption images of the $m_z = 1, 0, -1$ spin components after 24 ms Stern-Gerlach spin separation.

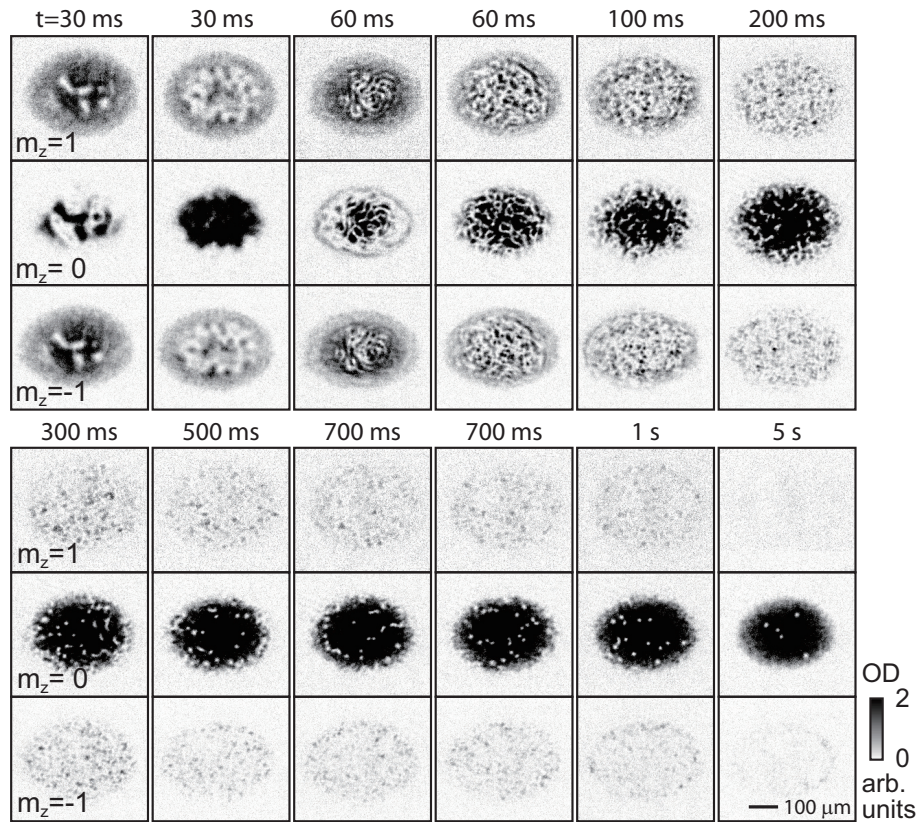


Figure 4.18: Phase transition from the EPP phase for $q/h = 10.6$ Hz. Absorption images of the $m_z = 1, 0, -1$ spin components after 24 ms Stern-Gerlach spin separation.

4.8 Outlook

The quenched EPP condensate across the EPP-to-EAP phase transition provides us an awesome platform to access the fascinating, but still uncharted physics area such as the formation and the evolution of a composite-topological defects and the suppression of the dynamical instability. By using the dynamic imaging such as absorptive spin-sensitive *in situ* imaging [33], one can capture the subsequent evolution of a MCS. When the true 2D system is built, a paired superfluid, having singlet pair superfluidity without spin ordering [115], can be observed by amplifying the spin fluctuations.

Chapter 5

Rotating Bose-Einstein condensate

In this chapter, we present the another type of non-equilibrium dynamics: the relaxation dynamics for a circulating BEC. Being irrotational, a superfluid shows a unique response to rotation, which involves quantized vortices. Since its first realization, a BEC under rotation has been of great interest for the study of superfluidity and various vortex dynamics have been investigated in different rotation regimes [131]. Many experimental methods were demonstrated for rotating trapped BECs, which include phase imprinting techniques based on optical transitions [132] or spin rotation [43, 133], and applying rotating elliptical potentials [134–138]. Rotating BECs were also produced by evaporative cooling of rotating thermal gases [139]. It is anticipated that in a rapid rotation limit a rotating BEC undergoes quantum phase transitions to strongly correlated quantum Hall states [140], and there are ceaseless experimental efforts to reach the fast rotation regime [141–143].

We present an experimental method for rotating a trapped BEC in an anharmonic trapping potential. A trapped BEC can have angular momentum in two forms: the center-of-mass (c.m.) motion around the trap center and the internal motion such as surface oscillations and quantized vortices. Contrary to a condensate in a harmonic potential, the anharmonicity of a trapping potential provides the coupling between the c.m. motion and the internal motion of a trapped condensate [144–147].

- Jae-yoon Choi, Seji Kang, and Yong-il Shin, “*Observation of a Geometric Hall effect in a Spinor Bose-Einstein Condensate with a Skyrmion Spin Texture*”, Physical Review Letter **111**, 245301 (2013).
- Seji Kang, Jae-yoon Choi, Sang Won Seo, Woo Jin Kwon, and Yong-il Shin, “*Rotating a BEC by shaking an anharmonic axisymmetric magnetic potential*”, Physical Review A **91**, 013603 (2015).

5.1 Anharmonic trapping potential

Our experiment uses Bose-Einstein condensates of sodium atom in the $|F = 1, m_F = -1\rangle$ [148]. We prepare 2×10^6 sodium atoms in a pancake-shaped optical dipole trap with trapping frequencies of $\omega_{x,y,z} = 2\pi \times (3.3, 4.1, 400)$ Hz and apply to the condensate a three-dimensional quadrupole magnetic field,

$$\mathbf{B} = \frac{B_q}{2}(x\hat{x} + y\hat{y} - 2z\hat{z}) - B_x\hat{x} - B_y\hat{y} + B_z\hat{z}. \quad (5.1)$$

The position of the zero-field point is controlled by the bias field $\{B_x, B_y, B_z\}$ as $Q = \{x_0, y_0, z_0\} = \{2B_x/B_q, 2B_y/B_q, B_z/B_q\}$. The overall external potential

can be described as

$$\begin{aligned}
V_{\text{trap}}(x, y, z) &= V_{\text{ODT}} + V_{\text{Quad}} + V_{\text{gravity}} \\
&= \frac{m}{2}(\omega_x^2 x^2 + \omega_y^2 y^2 + \omega_z^2 z^2) \\
&\quad + \frac{\mu_B B_q}{4} \sqrt{(x - x_0)^2 + (y - y_0)^2 + 4(z - z_0)^2} - mgz,
\end{aligned} \tag{5.2}$$

where m is the atomic mass, μ_B is the Bohr magneton, and g is the gravitational acceleration. The axial field gradient is set to be $B_q = 7.6$ T/m [63], almost compensating the gravitational sag in the optical trap, and the position of the zero-field point is placed at $Q = \{0, 0, 32(2)\}$ μm [Fig. 5.1 (a)]. The transverse trapping frequency at the center of the hybrid trap is $\omega_0 = \sqrt{\frac{\mu_B B_q}{8mz_0} + \omega_{x,y}^2}$. For dipole oscillations with small amplitude of 16 μm , the trapping frequency is measured to be $\omega_0 = 2\pi \times 42.5$ Hz. The trap anisotropy due to the weak optical potential is estimated to be less than 0.2%. For the oblate condensate which is confined to the $z = 0$ plane, we approximate the radial trapping potential as

$$V_{\text{rad}}(r) = 2m\omega_0^2 z_0 \sqrt{r^2 + z_0^2}, \tag{5.3}$$

where $r = \sqrt{x^2 + y^2}$. This potential behaves linear for large $r \leq z_0$, representing a highly anharmonic, axisymmetric trap for the condensate [Fig. 5.1 (b)]. The Thomas-Fermi radius $R_{\text{TF}} \approx 40$ μm , which is comparable to z_0 .

5.2 Generation of circular c.m. motion

In order to generate a circular c.m. motion of the condensate, we apply a rotating bias field as $\{B_x(t), B_y(t)\} = \delta B(\sin(\omega_m t), \cos(\omega_m t))$. The trap center correspondingly circulates around the origin as $\mathbf{d}(t) = \{(x_0(t), y_0(t))\} =$

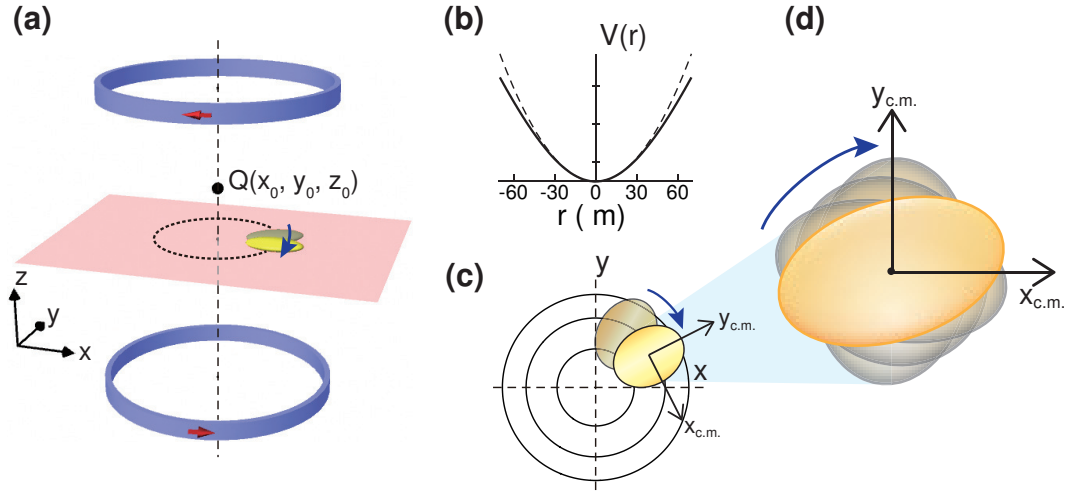


Figure 5.1: (Color online) Circulating Bose-Einstein condensate in an anharmonic magnetic potential. (a) Schematic of the experimental setup. A condensate (yellow ellipsoid) is confined in an optical sheet (red plane) and a quadrupole magnetic field is generated by a pair of coils (blue rings). The red arrows indicate the current directions and Q is the zero-field point. (b) Anharmonic radial trapping potential from the quadrupole magnetic field. The dashed line shows a harmonic potential having the same curvature at the trap center. (c) At an off-center position, the local curvatures of the anharmonic trapping potential are different for the radial and azimuthal directions. When the condensate circulates around the trap center, it experiences a rotating anisotropic potential. The center-of-mass motion (c.m.) of the condensate is coupled to its internal motion. (d) The deformation of the condensate in the center-of-mass frame.

$d\{\sin(\omega_m t), \cos(\omega_m t)\}$ with $d = 2\delta B/B_q$. The turn-on sequence of the field modulations is displayed in terms of the trap position in Fig. 5.2(a). In the reference frame of the circulating magnetic trap, the equation of motion for an atom in the $z = 0$ plane is given as

$$m \frac{d^2 \mathbf{r}'}{dt^2} = -\frac{dV_r(r)}{dr'} + m\omega_m^2 \mathbf{d}(t) + \frac{d\mathbf{r}'}{dt} \times \mathbf{B}_z^e, \quad (5.4)$$

where $\mathbf{r}' = (x - x_0, y - y_0)$, \mathbf{B}_z^e is the effective magnetic field in z -direction due to the Skrymion spin texture and the second term is the inertial force due to the trap shaking. The last term is due to the Lorentz force by the \mathbf{B}^e (See sec. 5.4). In the case of a harmonic trap with $V_r(r) = \frac{1}{2}m\bar{\omega}^2 r^2$, this rotating force will drive the atom to have a circular motion, whose radial position oscillates as $r' = \frac{2\omega_m^2 d}{(\bar{\omega}^2 - \omega_m^2)} \sin(\frac{\bar{\omega} - \omega_m}{2} t)$. The angular momentum can be resonantly injected into the system. This is indeed analogous to what we typically do to rotate liquid in a glass without a spoon. This method is very simple, requiring no sophisticated technique such as dynamically deforming the trapping potential.

Figure 5.2(b) shows the temporal evolution of the c.m. position of the condensate for $\omega_m = 2\pi \times 39.5$ Hz and $d = 3 \mu\text{m}$. An *in-situ* absorption image was taken every 4 ms of the driving and the c.m. position was determined from a two-dimensional Gaussian fitting. The condensate develops a circular c.m. motion and the radius of the circular motion oscillates with a period of 400 ms. For $t_d = 200$ ms driving, the radial position of the condensate increases up to about $65 \mu\text{m}$ and the external angular momentum per particle, associated with the c.m. motion, increases as large as $|L_z| \approx 350\hbar$, where \hbar is the Planck constant divided by 2π . We see that the measured c.m. trajectory is reasonably accounted for by the single-particle simulation using Eqn. Eq:RotMotion [Fig. 5.2(c)]. The deviation for later time is understandable because the c.m.

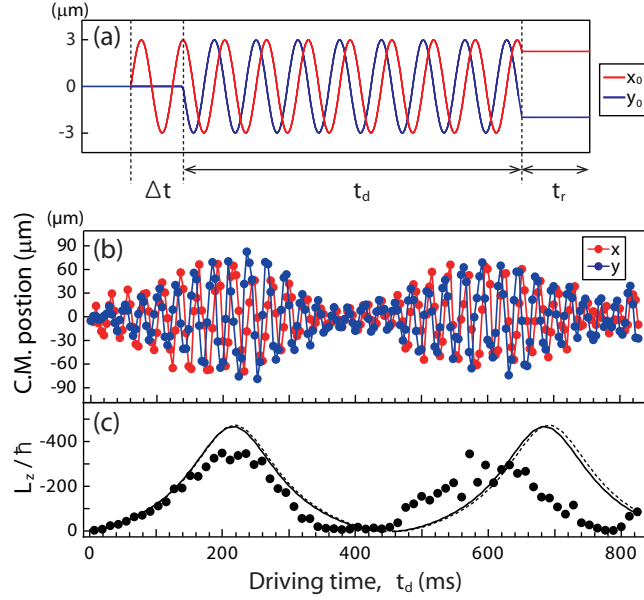


Figure 5.2: Generation of a circular c.m. motion of the condensate. (a) The trapping potential is circularly shaken by applying a rotating bias field. The driving frequency is $\omega_m = 2\pi \times 39.5$ Hz close to the trapping frequency at the trap center $\omega_0 = 2\pi \times 42.5$ Hz. (b) The temporal evolution of the c.m. position of the condensate (single measurements for every 4 ms) and (c) the external angular momentum per particle, L_z , of the condensate. The c.m. velocity was determined from the position data in (b) and L_z is displayed with 16 ms binning. The solid line denotes the numerical result from the single-particle simulation using Eqn. (4) and the dashed line shows the numerical result including the effective Lorentz force (see Chap. 5.4).

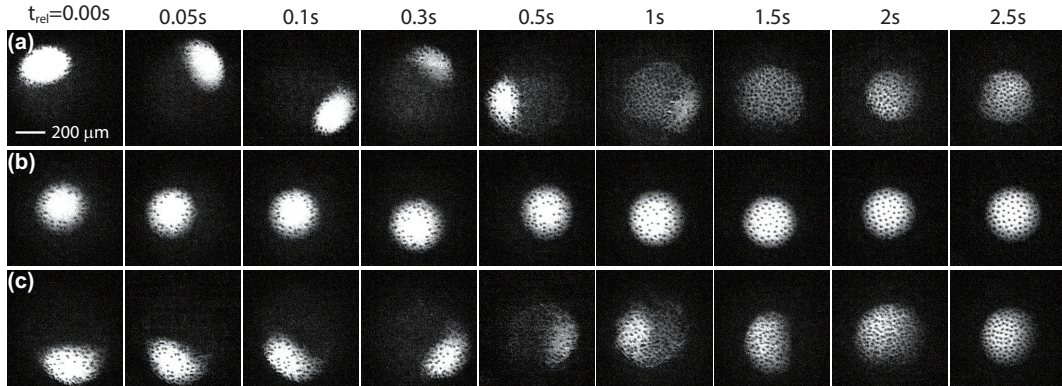


Figure 5.3: (a-c) The whole development of vortex nucleation in a spinor condensate relaxed in a stationary anharmonic trap, after the condensate is modulated circularly. Absorption images after 10 ms time-of-flight after various relaxation times t_{rel} . The modulation times are $t_d =$ (a) 200 ms, (b) 400 ms, and (c) 1000 ms, respectively.

motion of the condensate having a finite spatial extent cannot be separable from its internal motion in the anharmonic potential [145–147]. In the following experiment, we employ the same driving procedure.

5.3 Relaxation of the circulating Bose-Einstein condensate

Figure 5.3 show the temporal evolution of the circulating condensate having different angular momentum, L_z by varying t_d : (a, c) maximum $|L_z| \approx 350\hbar$, and (b) minimum $L_z \approx 0\hbar$. The relaxation of the circulating condensate is characterized by the shape deformation, the fraction of BEC, and angular momentum or vortex numbers. We count the number of vortices by using computer algorithm well described by Choi’s thesis [63].

5.3.1 Surface mode excitation

At an off-center position in the anharmonic trapping potential, the local curvature of the potential is not isotropic. For the external potential in Eqn. 5.3, the local trapping frequencies along the radial direction and the azimuthal direction are given as

$$\begin{aligned}\omega_r &= \sqrt{\frac{1}{m} \frac{\partial^2 V_r}{\partial r^2}} = \omega_0 \left[1 + \frac{r^2}{4z_0^2} \right], \\ \omega_\theta &= \sqrt{\frac{1}{mr} \frac{\partial V_r}{\partial r}} = \omega_0 \left[1 + \frac{r^2}{4z_0^2} \right],\end{aligned}\tag{5.5}$$

respectively, and the local trap anisotropy $\epsilon = \frac{(\omega_0^2 - \omega_r^2)}{\omega_0^2 + \omega_r^2} \geq 0$. Therefore, the circulating condensate would experience a rotating anisotropic trapping potential in its c.m. reference frame [Fig. 1(c)]. As the radial position of the condensate increases under the driving, the local trap anisotropy gradually increases. The rotating anisotropic potential would cause surface mode excitations [149, 150], possibly leading to vortex nucleation [134–138, 151–158].

Figure 3(a) shows a series of in situ absorption images of the condensate for $t_d = 180 - 216$ ms. In this period, the radial position of the condensate is $r \approx 65 \mu\text{m}$, giving $\epsilon = 0.34$ with $\omega_\theta/\omega_0 = 0.84$ and $\omega_r/\omega_0 = 0.59$. We see that the circulating condensate is elliptically deformed and the axis of the deformation rotates with the same frequency of the condensate circulation [Fig. 5.4(b)]. The long axis of the condensate is found to be along the azimuthal direction, which is orthogonal to the weak confining direction of the local anisotropic trapping potential. This is consistent with the theoretical prediction for the case where the rotating frequency Ω of the elliptical potential is higher than the trapping frequencies [152], which is true in our experiment for $\Omega \approx \omega_m > \omega_{\theta,r}$. The steady-state solution for a condensate in a rotating elliptical harmonic potential predicts the aspect ratio of the deformed condensate to be 1.16 for our experimental

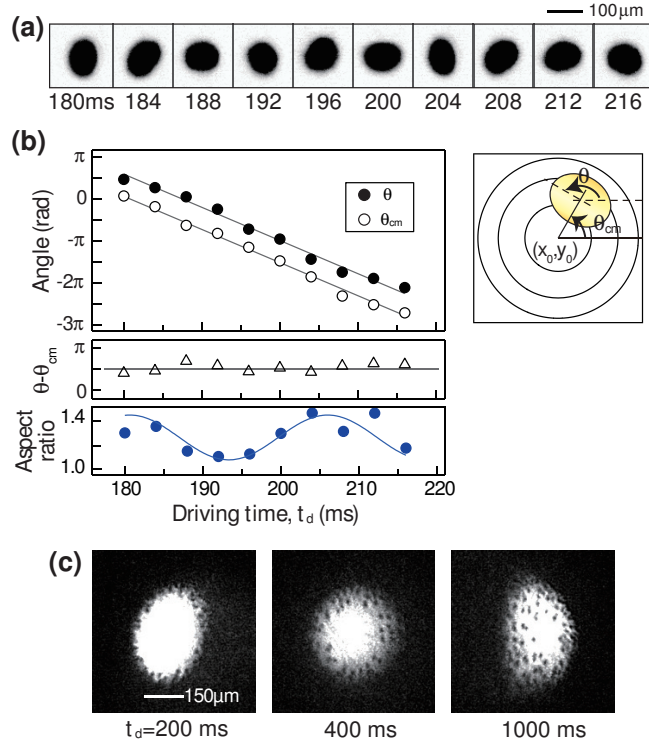


Figure 5.4: Surface mode excitations in the circulating condensate. (a) In situ absorption images of the condensates for various driving times t_d . (b) Time evolution of the shape deformation of the condensate. θ and $\theta_{c.m.}$ denote the orientation of the long axis of the condensate and the azimuthal angle of the c.m. position, respectively. The aspect ratio shows small oscillations. The solid lines are guide lines for the eye. (c) Images after time-of-flight expansion. Vortices are nucleated in the boundary region of the condensate.

condition with $\Omega/\omega_\theta \approx 1.11$ and $\epsilon = 0.3$ [152]. We observe that the aspect ratio of the circulating condensate oscillates around 1.25 [Fig. 5.4(b)], which is in reasonable agreement with the prediction.

We identify vortex nucleation in the circulating condensate by taking an absorption image after releasing the trapping potential and subsequent expansion for 16.25 ms [Fig. 5.4(c)]. We turn off the magnetic potential 6.25 ms earlier than the optical potential, which is helpful to improve the visibility of the vortex core [97]. Vortices are generated in the condensate boundary and gradually diffuse into the inner region. The vortex population increases for longer driving time. In previous experiments [134–138], which investigated condensates in rotating elliptical potentials, the vortex nucleation mechanism was mainly associated with the dynamic instability via the quadrupole surface mode resonance [152–158]. In our experiment, the rotating frequency Ω is almost two times higher than the resonance frequency of the quadrupole surface mode, $\Omega_2 \approx \sqrt{\omega_\theta^2 + \omega_r^2}/2 = 2\pi \times 21.7$ Hz, and the dynamic instability is not likely to be involved in the vortex nucleation. Furthermore, the observed oscillations of the aspect ratio of the condensate indicate that the deformed condensate is dynamically stable. This suggests that the vortex nucleation in the circulating condensate is driven by the energetic instability in the rotating potential.

5.3.2 Thermal distillation: re-condensation

After stopping the trap shaking, we investigate the relaxation of a freely circulating condensate. Figure 5.5 and figure 5.3(a) show the time-of-flight images of the condensate for various relaxation times t_r after 200 ms driving. In the early phase of the evolution, the condensate keeps circulating, maintaining

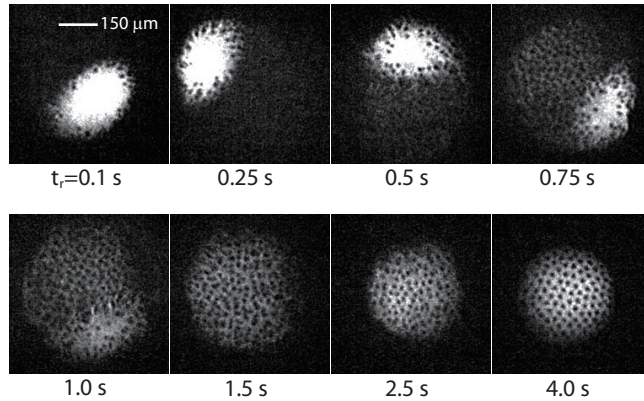


Figure 5.5: Relaxation of the circulating condensate in the anharmonic trapping potential. Time-of-flight images of the condensates for various relaxation times t_r after 200 ms driving. The circulating condensate evolves into a rotating condensate with a triangular lattice of vortices.

its elliptically deformed shape. It is known that a particle in a rotating elliptical harmonic potential is dynamically unstable for $\omega_r < \Omega < \omega_\theta$ [136, 152, 159]. Although $\Omega = \omega_\theta$ in our case for the free circulation, close to the unstable regime, the condensate remains stable without showing any turbulent behavior. Over 500 ms, more vortices are nucleated up to $N_v \approx 40$ and the radius of the c.m. motion decreases gradually to about $45 \mu\text{m}$.

As the relaxation proceeds, we observe that a faint cloud slowly forms over a large central area. The cloud grows in density and reveals a large number of vortices, which indicates that the newly formed cloud becomes a part of the condensate. This process is remarkably gentle and the elliptical region of the original circulating condensate is well preserved as a high density part. The high-density part of the condensate gradually shrinks and becomes completely dissolved at $t_r \approx 1.5$ s. At this moment, we have a large round condensate containing many vortices whose spatial distribution is disordered. The vortex number is counted up to $N_v \approx 200$. This state represents a rotating condensate

with an irregular vortex lattice.

The development of the rotating condensate might be understood as a thermal equilibrating process in the reference frame corotating with the circulating condensate (Fig. 5.6). In the rotating reference frame, the effective trapping potential is given as $V^e(r) = V(r) - \frac{1}{2}m\omega_0^2 r^2$, including the centrifugal potential. Because of the anharmonicity of $V(r)$, $V^e(r)$ has a restricted trapping region with a global potential minimum at the center. The circulating condensate is depicted to be located at the edge of the trapping region with the help of the Coriolis force [Fig. 5.6(a)]. Since the circulating condensate has an effective chemical potential higher than the potential minimum, it would thermodynamically drive thermal atoms to condense at the trap center, which would result in a rotating condensate at the trap center.

This is a kind of a thermal distillation process where a condensate in a metastable state is transferred to the true ground state via thermal atoms [94]. Note that such a distillation process would not occur in a system using a harmonic potential, where the effective external potential for a circulating condensate is flat, having no potential minimum. When a quartic potential is employed, which provides stronger confinement at a larger radius, the effective potential has a ring geometry and a circulating condensate would relax into a giant vortex state [160, 161].

In our experiment, the collision time of thermal atoms is estimated to be $\tau \sim 25$ ms for the sample temperature $T \sim 300$ nK¹ [162]. The growth of the rotating condensate happens on a time scale of $\sim 20\tau$, which is comparable to the results in previous studies on Bose condensation [163]. The formation of

¹The collision time $\tau = (n_{\text{th}}\sigma\bar{v})^{-1}$, where $n_{\text{th}} = 2.612(mk_B T/2\pi\hbar^2)^{3/2}$ is the atom density of a saturated thermal cloud, $\sigma = 8\pi a^2$ denotes the elastic collision cross section (the scattering length $a = 2.75$ nm), and $\bar{v} = 4\sqrt{k_B T/\pi m}$ is the thermal velocity.

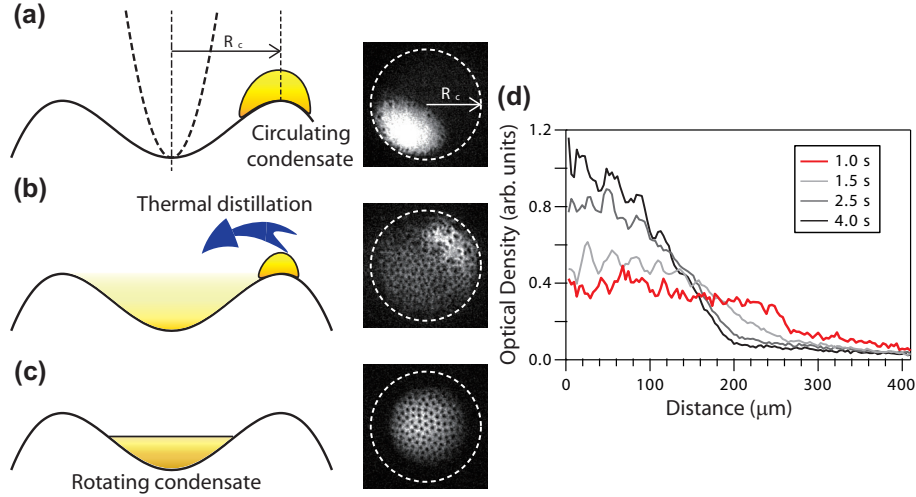


Figure 5.6: Thermal distillation process. (a) In a reference frame corotating with the circulating condensate, the condensate is located at the edge of the trapping region of the effective trapping potential (solid line). The dashed line shows the trapping potential in the laboratory frame. (b) The condensate thermodynamically drives thermal atoms to condense in the center region having the trapping potential minimum. (c) A rotating condensate is formed at the trap center. The right column displays the images corresponding to each step of the relaxation process. The dashed circles indicate the trap boundary determined by the centrifugal effect. (d) Radial density distributions of the rotating condensates, which are obtained by azimuthally averaging the images in Fig. 5.5. For $t_r = 1$ s, the high-density part, corresponding to the original circulating condensate, is excluded in the averaging. The density modulations in the center region result from density-depleted vortex cores.

the rotating condensate over a large area implies that the atomic influx from the circulating condensate is higher than the internal equilibration rate of the rotating condensate.

The round boundary of the whole condensate, which is determined by the radial position of the circulating condensate, seems to reveal the trapping radius of the effective potential in the rotating reference frame [Fig. 5.6(a)]. From $dV_r^c/dr = 0$, the trapping radius is given as $R_c = 2z_0\sqrt{(\omega_0/\omega_\theta)^4 - 1}$. When the spatial extent of a rotating condensate is limited by the centrifugal effect, the vortex number of the condensate would be

$$N_v^c \approx \frac{m}{\hbar}\omega R_c^2 = \frac{4mz_0^2}{\hbar} \frac{\omega_0^4 - \omega^4}{\omega^3}, \quad (5.6)$$

which is estimated from the circulation relation $\oint_r = R_c v_s dr = (h/m)N_v^c$, where v_c is the superfluid velocity. For $t_r = 1$ s, the in situ radius of the rotating condensate is measured to be about 50 μm , suggesting $N_v^c \approx 200$. This number is comparable to the maximum vortex number observed in the experiment. The rotating frequency of the newly formed rotating condensate is forced to be set to the circulation frequency of the initial condensate.

After the high-density part in the condensate vanishes, the rotating condensate with an irregular vortex lattice undergoes an equilibrating process. Crystallization into a triangular vortex lattice takes about 2 s, where the radial extent of the condensate decreases by about 25% and the atomic density at the center increases by a factor of 2 [Fig. 5.6(d)]. At $t_r = 4$ s, the vortex number is $N_v \approx 120$. One may expect an increase of the rotating frequency due to the reduction of the moment of inertia of the condensate, but the vortex areal density, i.e., the rotation frequency of the condensate, shows no significant change during the evolution. The thermal fraction of the sample is as high as 50% at

this phase and thus the interactions between the condensate and the thermal cloud must be important. The rotating thermal cloud might lock the condensate rotation in the equilibration process. With an initial state having a triangular lattice with about 100 vortices, the half lifetime of the vortices was measured to be 9 s.

5.3.3 Rotating thermal clouds

We present the relaxation of the condensate after 400 ms driving. This case is special in that the c.m. motion of the condensate almost stops after one oscillation of the radial position [Fig. 5.2(c) and 5.3(b)]. Right after the driving, the condensate shows a round shape and contains about 30 vortices in its boundary region. As the hold time increases, we observe that more vortices come in and migrate to the inner region of the condensate, and, finally, a triangular lattice of about 60 vortices forms after 2 s [Fig. 5.7(a)]. In the Thomas-Fermi approximation, we estimated the angular momentum per particle of the condensate as $L_z = \hbar \sum_i [1 - (r_i/R)^2]^{5/2}$, where r_i/R is the ratio of the vortex radial position to the condensate radius, which was measured for each vortex from the image [23]. Since the angular momentum of the condensate is increased during the evolution [Fig. 5.7(b)], it is obvious that the thermal cloud surrounding the condensate rotates faster than the condensate at the beginning. During the driving period, the thermal cloud is not only subject to the applied rotating force, but also dragged by the circulating condensate. We note that the time scale of the vortex lattice crystallization is similar to that in the previous case with $t_d = 200$ ms.

The equilibrium process of a condensate in a rotating thermal cloud was

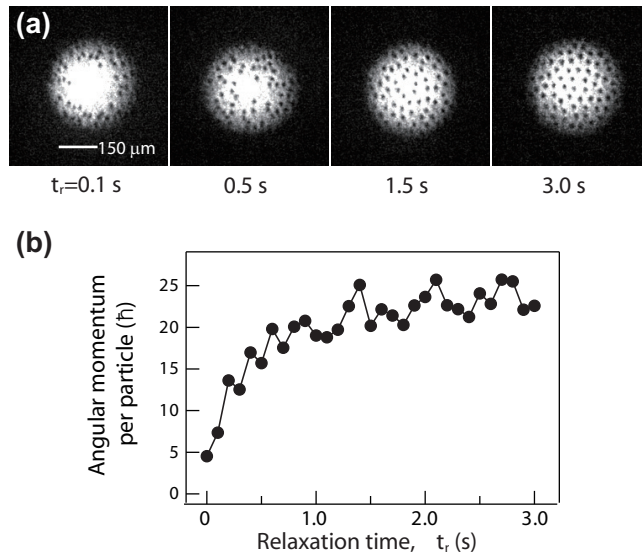


Figure 5.7: Spinning up the condensate by a rotating thermal cloud. (a) Time-of-flight images of the condensate for various hold times t_r after 400 ms driving. There is no noticeable c.m. motion of the condensate [Fig. 5.2(b)]. The number of vortices in the condensate gradually increases over the holding time and a vortex lattice forms. (b) Evolution of the angular momentum per particle, which is determined from the relative positions of vortices in the condensate.

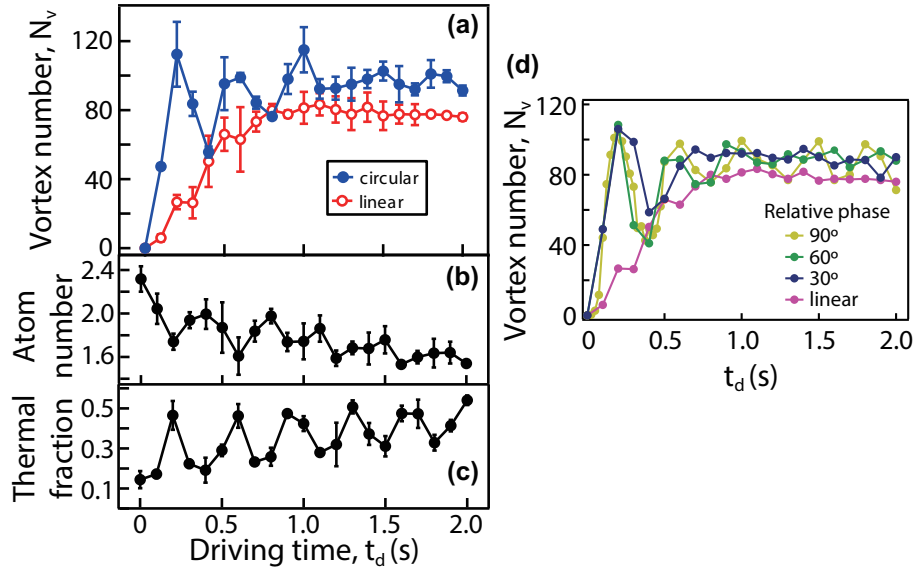


Figure 5.8: (a) Vortex number N_v vs driving time t_d . The vortex number was measured after 3 s relaxation. The open circles show the result for linear driving, where the transverse bias fields, B_x and B_y , were modulated in phase with $t = 0$ [Fig. 5.2(a)]. Each data point consists of three measurements. The corresponding evolutions of (b) the total atom number and (c) the thermal fraction of the sample. (d) Temporal evolution of vortex number under various elliptical polarized driving. The error bars are not displayed. See also section 5.4.

theoretically investigated to study the role of a thermal cloud in vortex nucleation and lattice formation [164, 165]. Our rotating method provides an experimental way to prepare a nonequilibrium state where a thermal cloud rotates faster than a condensate. We expect that the rotation frequency difference between the thermal cloud and the condensate may be controlled by the driving parameters or the anharmonicity of the trapping potential. In future, we will pursue a quantitative analysis of the equilibrium process, including measurements of the rotating frequency of the thermal cloud [137, 139].

Finally, we present the vortex number, N_v after 3 s relaxation as a function of the driving time, t_d in Fig. 5.8. As the driving time increases, the vortex

number increases and becomes saturated to $N_v = 100$ with damped oscillations. The oscillations reflect the oscillating behavior of the external angular momentum of the driven condensate [Fig. 5.2(c)]. The total atom number and the thermal fraction of the sample also oscillate accordingly due to the atom loss and heating associated with the relaxation process.

The angular momentum per particle of the stably rotating condensate with 100 vortices is about $40\hbar$, which is only 10% of the maximum external angular momentum of the circulating condensate. The poor efficiency of the angular momentum transfer to the internal rotation of the condensate is an intrinsic aspect in the evolution of an isolated system. When the energy of the system is given as $E = \frac{1}{2}L_z^2/I$, where I is the moment of inertia of the system, the energy and angular momentum conservations require that I should be preserved in the evolution. This means that when a rotating condensate forms at the trap center, generation of thermal atoms having high angular momentum is unavoidable. This argument suggests that in order to improve the transfer efficiency of the angular momentum, i.e., to obtain a faster rotating condensate, one needs to provide an additional work by dynamically deforming the trapping potential during the relaxation.

5.4 Gauge-field effect in a magnetic quadrupole field

When a particle with spin moves in a spatially varying magnetic field, the particle acquires a quantum mechanical phase associated with the adiabatic spin rotation, which is known as the Berry phase [166]. A gauge potential can

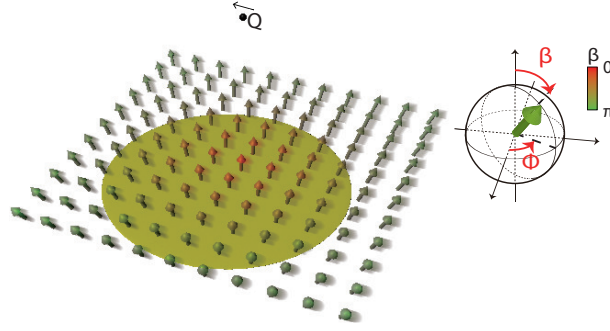


Figure 5.9: Skymion spin texture configuration. When the zero-field point moves by oscillating DC magnetic field, the skymion spin texture also moves.

be defined for the spatial distribution of the spin orientation and this results in generation of an effective magnetic field for the particle [167, 168]. When a Bose-Einstein condensate is trapped in a magnetic potential, its spin texture is imposed by the magnetic-field distribution. Because of the spin-gauge symmetry, the condensate would experience an effective magnetic field originated from the spin texture [169].

5.4.1 Skymion Spin texture

In the current setup, the condensate is radially confined by the quadrupole magnetic field. Its spin texture exhibits a fountain-like configuration, displayed in Fig. 5.9 which is often referred to as a Skymion spin texture.

With non-uniform magnetic field, the Hamiltonian of scalar BEC is given as

$$H = \frac{\mathbf{p}^2}{2m} + g_F \mu_B \mathbf{F} \cdot \mathbf{B}, \quad (5.7)$$

where $\mathbf{B}(\mathbf{r}, t)$ is spatially varying magnetic field and its direction is defined as $\hat{b} = \mathbf{B}/|\mathbf{B}|$. Consider the local unitary transformation $U = \exp(-i\beta\hat{n} \cdot \mathbf{F})$, satisfying $U(\hat{b} \cdot \mathbf{F})U^\dagger = F_z$, where $\hat{n} = \hat{b} \times \hat{z}/|\hat{b} \times \hat{z}|$ and β is tilting angle from

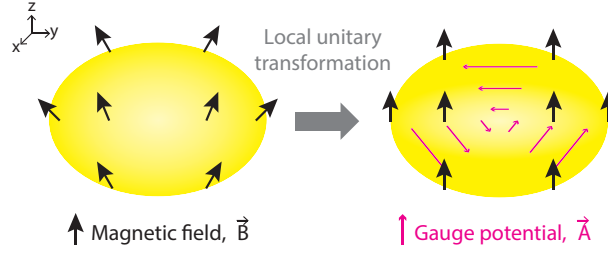


Figure 5.10: By a local unitary transformation $U(\mathbf{r})$, a spatially varying magnetic field is mapped to an effective magnetic field, where the field direction is uniform containing a gauge potential $\mathbf{A} = -iU\nabla U^\dagger$.

β to z -axis.

Using the unitary transformation, the Hamiltonian can be expressed in the $|\varphi\rangle = U|\Psi\rangle$ basis as

$$i\hbar \frac{\partial}{\partial t} |\Psi\rangle = H |\Psi\rangle \quad (5.8)$$

$$\begin{aligned} i\hbar \frac{\partial}{\partial t} |\varphi\rangle &= (UHU^\dagger - i\hbar U \partial_t U^\dagger) |\varphi\rangle = H^e |\varphi\rangle \\ &= \left(\frac{1}{2m} (\mathbf{p} + \hbar \mathbf{A})^2 - \hbar V + g_F \mu_B F_z |\mathbf{B}| \right) |\varphi\rangle, \end{aligned} \quad (5.9)$$

where the effective vector potential $\mathbf{A}(\mathbf{r}, t) = -iU\nabla U^\dagger$ and effective scalar potential $A_0(\mathbf{r}, t) = iU \partial_t U^\dagger$. \mathbf{A} comes from the non-uniform spin texture and A_0 comes from the time-varying spin texture. Then, the effective electromagnetic fields arises from Eqn. 5.4.1,

$$\mathbf{E}_i^e = -\hbar \partial_i A_0 - \hbar \partial_t A_i = -m_F \hbar \hat{\mathbf{b}} \cdot (\partial_t \hat{\mathbf{b}} \times \partial_i \hat{\mathbf{b}}) \quad (5.10)$$

$$\mathbf{B}_i^e = -\hbar \epsilon^{ijk} (\partial_j A_k - \partial_k A_j) = -\hbar \frac{m_F}{2} \epsilon^{ijk} \hat{\mathbf{b}} \cdot (\partial_j \hat{\mathbf{b}} \times \partial_i \hat{\mathbf{b}}). \quad (5.11)$$

Note that the effective Hamiltonian has same form to the Hamiltonian of a charged particle in the magnetic field. Therefore, the geometric force can exert Lorentz force to a particle moving in the system with a non-uniform magnetic field, whether the particle is charged or not.

In our setup, the resultant effective magnetic field is given as

$$\begin{aligned}\mathbf{A}(\mathbf{r}') &= -\frac{\sqrt{r'^2 + 4z'^2} + 2z'}{r'\sqrt{r'^2 + 4z'^2}}\hat{\theta}, \\ \mathbf{B}^e(\mathbf{r}') &= -\hbar\nabla \times \mathbf{A} = \frac{2\hbar}{(r'^2 + 4z_0^2)^{3/2}}(-\mathbf{r}' + z_0\hat{z}).\end{aligned}\tag{5.12}$$

This gauge field is very weak and the corresponding cyclotron frequency, $\omega_c = \hbar/4mz_0^2$, is three orders of magnitude smaller than the trapping frequency [Fig. 5.2(c)]. In our recent work [177], we succeeded in demonstrating the existence of the effective Lorentz force in the current setup by observing that a circular c.m. motion of the trapped condensate is generated with linear driving, leading to vortex nucleation [Fig. 5.8(a,d) and Fig. 5.12(a)].

5.4.2 Chirality of Gauge potential

We study the gauge-field effect by investigating the response of the condensate to the trap shaking for various elliptical polarizations of the driving. We characterize the gauge-field effect by the number of vortices nucleated through driving. In order to control the polarization of the driving in a fine manner, we reduce B_y by a factor of 6 and apply a rotating bias field as $[B_x(t), B_y(t)] = \delta B[\sin(\omega_m t), \frac{1}{6}\sin(\omega_m t + \phi)]$. The relative phase ϕ is controlled by changing the turn-on time of B_y as $\Delta t = (3\pi - \phi)/\omega_m$ [Fig. 5.2(a)].

Figure 5.11 displays the vortex number measured after 500 ms driving and 3 s relaxation as a function of the relative phase. In the result, we see a two-dome structure which is asymmetric with respect to the sign of the relative phase ϕ . The right dome with clockwise driving is relatively more enhanced than the left dome with counterclockwise driving. This is consistent with the sign of the effective magnetic field. The rotation direction of the condensate was

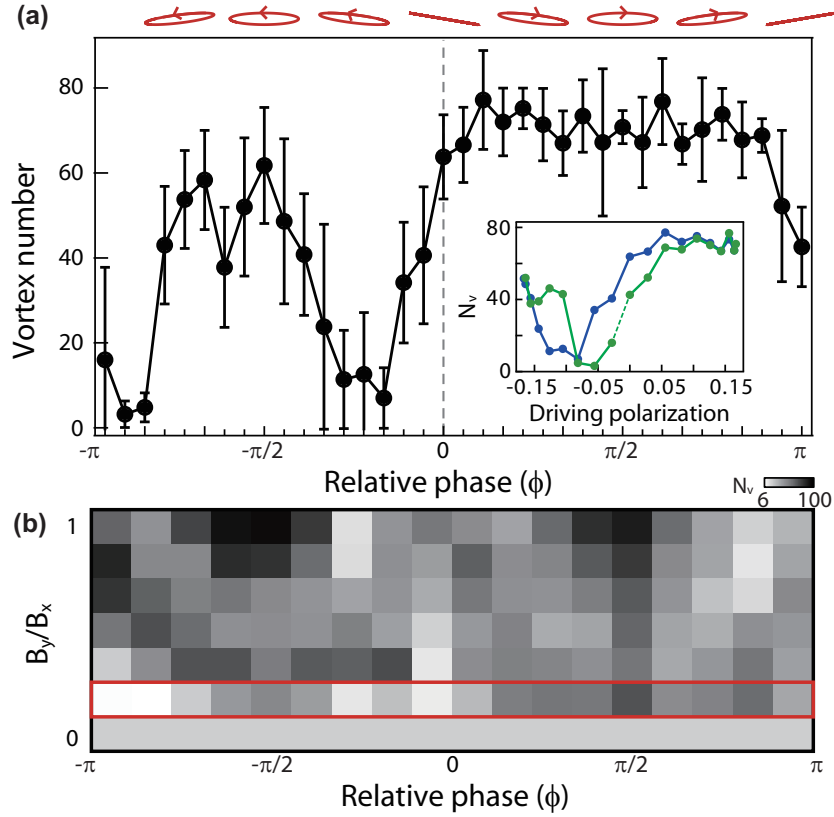


Figure 5.11: Gauge-field effect. (a) The vortex number N_v was measured after 500 ms driving and 3 s relaxation for various elliptical polarizations of the driving (see the top axis). The driving polarization is controlled by the relative phase ϕ between the modulations of B_x and B_y (see text for details). Each data point was obtained from five measurements. The inset displays the same result as a function of the elliptical polarization of the driving. The blue (green) circles denote the data with $|\phi| \leq \pi/2$ ($|\phi| > \pi/2$). (b) The vortex number is measured with various ratio of B_y/B_x (The data are measured in different day from (a)).

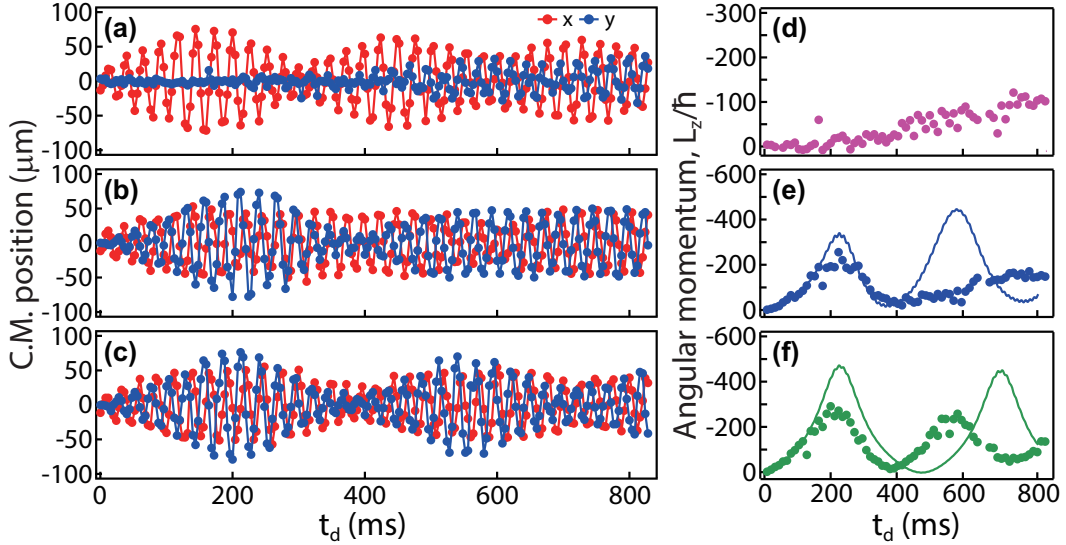


Figure 5.12: (a-c) Temporal evolution of condensate position under differently polarized external modulation of magnetic fields. The graphs are obtained data by 2D Gaussian fitting from a single in-situ image. (d-f) display external angular momentum per atom, L_z , and the data points are binned for 16 ms. L_z is measured from (a-c), each. (a,d) The condensate is modulated linearly in x -direction. The relative phases are (b,e) 60° and (c,f) 30° with $B_y/B_x = 1$, respectively. Solid lines are lines of the single-particle simulation.

confirmed to be the same as the sign of the driving polarization at $\phi = \pm\pi/2$ by measuring the precession direction of the quadrupole excitations in the rotating condensate [170, 171].

The vortex generation is almost suppressed at nonzero negative values of ϕ . An interesting question would be whether we can derive a quantitative relation between the magnitude of the gauge field and the critical driving polarization for nullifying the vortex generation. In the inset of Fig. 5.11, we replot the data as a function of the driving polarization, $\epsilon_d = \tan\left[\frac{1}{2}\sin^{-1}\left(\frac{2X_m Y_m \sin\phi}{X_m^2 + Y_m^2}\right)\right]$. In our experiment, one driving polarization can be realized with two values of ϕ and we see that the vortex numbers for two realizations are slightly different

from each other. This means that around the critical driving polarization, the condensate dynamics is sensitive to the turn-on time of B_y , i.e., the initial condition of the condensate. A more elaborated setup is desirable for a quantitative study of the gauge field with the critical polarization.

5.5 Outlook

One of the interesting extensions of this work would be introducing an additional trapping potential during the relaxation to mitigate the centrifugal effect and to increase the rotation speed of the condensate. We expect that our trapping potential might be deformed into a ring potential after the driving phase by applying an additional optical potential [172–174] or using RF-field dressing techniques [175, 176], which would result in a giant vortex state [160, 161]. Recently, Roncaglia et al. [143] showed that a giant vortex state having a large angular momentum in a ring potential is adiabatically connected to the bosonic $\nu = 1/2$ Laughlin state in a harmonic potential.

Chapter 6

Conclusions

Spinor Bose-Einstein condensates have several phases, depending on the nature of the interactions and the superfluidity, and offers scientists the opportunity to explore the unexplored worlds such as the spin turbulence and the early dynamics of universe in the feasible ways. Me and my colleagues peek in at this uncharted worlds a little through the quenched phase transition in a spin-wise 2D spinor BEC with antiferromagnetic interactions. In addition, we also observe the chirality of the gauge potential by measuring the relaxation dynamics from a circulating center-of-mass motion into the internal rotation of a BEC in an anharmonic trapping potential.

For the EAP-to-EPP phase transition, spin turbulence arises while the spin domains are generated via the spin-exchange collision. The time-space scaling is preserved in subsequent dynamics, including complex spin turbulence generation, and the spatial scaling is reflected by the number of HQVs.

Alluring phenomena happens with the EPP-to-EAP phase transition. The evolution of a quenched EPP condensate is easily affected by the initial spin fluctuations in contrast to that of a quenched EAP condensate. The thermally

excited spin fluctuations lead to the number increase of quantum noise seeds, but delay of the phase transition dynamics. Because of the sample lifetime, we cannot measure whether the dynamical instability is saturated or not. In addition, during the evolution, combined-topological defects such as magnetic composite-solitons and skyrmions are formed. We investigate the structure of a magnetic composite-soliton by using both the Bragg spectroscopy and the spin separated imaging, and observe its splitting process.

A magnetic composite-soliton might take the role of the topological order, mediating the KT-transition in 2D spin-1 system. Near the critical point, the symmetry of the order space recovers the full symmetry of the polar spin-1 order parameters, $[U(1) \times S^2]/\mathbb{Z}_2$, and thus it is quite fascinating question what quantum phenomena arise here. The paired-superfluid phase is one of the expected exotic phases [115], which is analogous to the FFLO state [178]. In addition, the evolution of a composite-topological defects are usually considered as the one of the candidates to reveal the scenario of the galaxy formation after the inflation. In the near future, one could uncover the spinor dynamics near the critical point and observe the singlet pair superfluids.

Bibliography

- [1] J. Eisert, M. Friesdorf, and C. Gogolin, “*Quantum manybody systems out of equilibrium*”, Nat. Phys. **11**, 124 (2015).
- [2] J. H. Traschen and R. H. Brandenberger, “*Particle production during out-of-equilibrium phase transitions*”, Phys. Rev. D **42**, 2491 (1990).
- [3] D. Fausti, R. I. Tobey, N. Dean, S. Kaiser, A. Dienst, M. C. Hoffmann, S. Pyon, T. Takayama, H. Takagi, A. Cavalleri, “*Light-Induced Superconductivity in a Stripe-Ordered Cuprate*”, Science **331**, 189 (2011).
- [4] R. K. Pathria and P. D. Beale, “*Statistical Mechanics, 3rd Edition*”, Butterworth-Heinemann publications, (2011).
- [5] N. Goldenfeld, “*Lectures on Phase Transitions and the Renormalization Group*”, Addison-Wesley publishing, (1992)
- [6] U. C. Täuber, “*Phase Transitions and Scaling in Systems Far from Equilibrium*”, Ann. Rev. Condens. Matt. Phys. **8**, 185 (2017).
- [7] A. J. Bray, “*The theory of phase-ordering kinetics*”, Adv. Phys. **43**, 357 (1994).

- [8] T. W. B. Kibble, “*Topology of cosmic domains and strings*”, J. Phys. A: Math. Gen. **9**, 1387 (1976).
- [9] T. W. B. Kibble, “*Some implications of a cosmological phase transition*”, Phys. Rep. **67**, 183 (1980).
- [10] W. H. Zurek, “*Cosmological experiments in superfluid Helium?*”, Nature, **317**, 505 (1985).
- [11] J. Dziarmaga, “*Dynamics of a quantum phase transition and relaxation to a steady state*”, Adv. Phys. **59**, 1063 (2010).
- [12] Y. Kawaguchi and M. Ueda, “*Spinor Bose-Einstein condensates*”, Phys. Rep. **520**, 253 (2012).
- [13] M. Ueda, “*Topological aspects in spinor Bose-Einstein condensates*”, Rep. Prog. Phys. **77**, 122401 (2014).
- [14] D. M. Stamper-Kurn and M. Ueda, “*Spinor Bose gases: Symmetries, magnetism, and quantum dynamics*”, Rev. Mod. Phys. **85**, 1191 (2013).
- [15] M. H. Anderson, J. R. Ensher, M. R. Matthews, C. E. Wieman, and E. A. Cornell, “*Observation of Bose-Einstein Condensation in a Dilute Atomic Vapor*”, Science, **269**, 198 (1995).
- [16] K. B. Davis, M. O. Mewes, M. R. Andrews, N. J. Van Druten, D. S. Durfee, D. M. Stamper-Kurn, and W. Ketterle, “*Bose-Einstein condensation in a gas of sodium atoms*”, Science, **269**, 198 (1995).
- [17] M. Greiner, O. Mandel, T. W. Hänsch, and I. Bloch, “*Collapse and revival*

- of the matter wave field of a Bose–Einstein condensate*”, Nature, **419**, 51 (2002).
- [18] C.-L. Hung, V. Gurarie, and C. Chin, “*From Cosmology to Cold Atoms: Observation of Sakharov Oscillations in a Quenched Atomic Superfluid*”, Science, **341**, 1213 (2013).
- [19] W. Ketterle, “*Nobel lecture: When atoms behave as waves: Bose-Einstein condensation and the atom laser*”, Rev. Mod. Phys. **74**, 113 (2002).
- [20] O. Penrose, and L. Onsager, “*Bose-Einstein Condensation and Liquid Helium.*”, Phys. Rev. **104**, 576 (1956).
- [21] C. N. Yang, “*Concept of Off-Diagonal Long-Range Order and the Quantum Phases of Liquid He and of Superconductors*”, Rev. Mod. Phys. **34**, 694 (1962).
- [22] H. J. Lewandowski, “*Coherences and correlations in an ultracold Bose gas*”, PhD thesis, University of Colorado (2002).
- [23] C. J. Pethick and H. Smith, “*Bose-Einstein Condensation in Dilute Gases, 2nd Edition*”, Cambridge University Press (2001).
- [24] T.-L. Ho, “*Spinor Bose Condensates in Optical Traps.*”, Phys. Rev. Lett. **81**, 742 (1998).
- [25] T. Ohmi and K. Machida, “*Bose-Einstein Condensation with Internal Degrees of Freedom in Alkali Atom Gases*”, J. Phys. Soc. Jpn. **67**, 1822 (1998).
- [26] J. Stenger, S. Inouye, D. M. Stamper-Kurn, H.-J. Miesner, A. P. Chikkatur,

- and W. Ketterle, “*Spin domains in ground-state Bose–Einstein condensates*”, *Nature*, **396**, 345 (1998).
- [27] M.-S. Chang, C. D. Hamley, M. D. Barrett, J. A. Sauer, K. M. Fortier, W. Zhang, L. You, and M. S. Chapman, “*Observation of spinor dynamics in optically trapped ^{87}Rb Bose-Einstein condensates*”, *Phys. Rev. Lett.* **92**, 140403 (2004).
- [28] S. Mukerjee, C. Xu, and J. E. Moore, “*Topological Defects and the Superfluid Transition of the $s=1$ Spinor Condensate in Two Dimensions.*”, *Phys. Rev. Lett.* **97**, 120406 (2006).
- [29] J. M. Higbie, “*First Steps toward Precision Measurements using Multi-component Bose-Einstein Condensates of ^{87}Rb* ”, PhD thesis, University of California, Berkeley (2005).
- [30] L. Sadler, “*Dynamics of a Spin 1 Ferromagnetic Condensate*”, PhD thesis, University of California, Berkeley (2006).
- [31] S. R. A. Leslie, “*On Spinor Condensates as Amplifiers, Sensors and Tunable Quantum Playgrounds for Studies of Spin*”, PhD thesis, University of California, Berkeley, 2008.
- [32] J. S. Guzman, “*Explorations of Magnetic Phases in $F = 1$ ^{87}Rb Spinor Condensates*”, PhD thesis, University of California, Berkeley (2012).
- [33] G. E. Marti, “*Scalar and Spinor Excitations in a Ferromagnetic Bose-Einstein Condensate*”, PhD thesis, University of California, Berkeley (2014).
- [34] F. Zhou, “*Spin Correlation and Discrete Symmetry in Spinor Bose-Einstein Condensates*”, *Phys. Rev. Lett.* **87**, 080401 (2011).

- [35] J. Lovegrove, M. O. Borgh, and J. Ruostekoski, “*Energetically stable singular vortex cores in an atomic spin-1 Bose-Einstein condensate*”, Phys. Rev. A **86**, 013613 (2012).
- [36] M. W. Ray, E. Ruokokoski, S. Kandel, M. Möttönen, and D. S. Hall, “*Observation of Dirac monopoles in a synthetic magnetic field*”, Nature, **505**, 657 (2014).
- [37] M. W. Ray, E. Ruokokoski, K. Tiurev, M. Möttönen, and D. S. Hall, “*Observation of isolated monopoles in a quantum field*”, Science, **348**, 544 (2015).
- [38] D. S. Hall, M. W. Ray, K. Tiurev, E. Ruokokoski, A. H. Gheorghe, and M. Möttönen, “*Tying quantum knots*”, Nat. Phys. **12**, 478 (2016).
- [39] Y. Kawaguchi, M. Nitta, and M. Ueda, “*Knots in a Spinor Bose-Einstein condensate*”, Phys. Rev. Lett. **100**, 180403 (2008).
- [40] V. Pietila, and M. Möttönen, “*Creation of Dirac Monopoles in Spinor Bose-Einstein Condensates*”, Phys. Rev. Lett. **103**, 030401 (2009).
- [41] S.W. Seo, S. Kang, W.J. Kwon, and Y. Shin, “*Half-Quantum Vortices in an Antiferromagnetic Spinor Bose-Einstein Condensate*”, Phys. Rev. Lett. **115**, 015301 (2015).
- [42] J. Ruostekoski, J. R. Aglin, “*Spin Correlation and Discrete Symmetry in Spinor Bose-Einstein Condensates*”, Phys. Rev. Lett. **91**, 190402 (2003).
- [43] J. Choi, W.J. Kwon, and Y. Shin, “*Observation of Topologically Stable 2D Skyrmions in an Antiferromagnetic BEC*”, Phys. Rev. Lett. **108**, 035301 (2012).

- [44] S. Kang, S.W. Seo, J.H. Kim, and Y. Shin, “*Emergence and scaling of spin turbulence in quenched antiferromagnetic spinor BECs*”, Phys. Rev. Lett. **95**, 053638 (2017).
- [45] C. Klempt, O. Topic, G. Gebreyesus, M. Scherer, T. Henninger, P. Hyllus, W. Ertmer, L. Santos, and J. J. Arlt, “*Multiresonant Spinor Dynamics in a Bose-Einstein Condensate*”, Phys. Rev. Lett. **103**, 312 (2009).
- [46] M. Scherer, B. Lucke, G. Gebreyesus, O. Topic, F. Deuretzbacher, W. Ertmer, L. Santos, J. J. Arlt, and C. Klempt, “*Spontaneous Breaking of Spatial and Spin Symmetry in Spinor Condensates*”, Phys. Rev. Lett. **105**, 135302 (2010).
- [47] D. Jacob, L. Shao, V. Corre, T. Zibold, L. De Sarlo, E. Mimoun, J. Dalibard, and F. Gerbier, “*Phase diagram of spin-1 antiferromagnetic Bose-Einstein condensates*”, Phys. Rev. A, **86**, 061601(R) (2012).
- [48] C. D. Hamley, C. S. Gerving, T. M. Hoang, E. M. Bookjans, and M. S. Chapman, “*Spin-nematic squeezed vacuum in a quantum gas*”, Nat. Phys. **8**, 305 (2012).
- [49] L. E. Sadler, J. M. Higbie, S. R. Leslie, M. Vengalattore, and D. M. Stamper-Kurn, “*Spontaneous symmetry breaking in a quenched ferromagnetic spinor Bose condensate*”, Nature, **443**, 312 (2006).
- [50] S. R. Leslie, J. Guzman, M. Vengalattore, J. D. Sau, M. L. Cohen, and D. M. Stamper-Kurn, “*Amplification of fluctuations in a spinor Bose-Einstein condensate*”, Phys. Rev. A **79**, 043631 (2009).

- [51] F. Gerbier, A. Widera, S. Fölling, O. Mandel, and I. Bloch, “*Resonant control of spin dynamics in ultracold quantum gases by microwave dressing*”, Phys. Rev. A **73**, 041602(R) (2006).
- [52] J. Guzman, G.-B. Jo, A. N. Wenz, K. W. Murch, C. K. Thomas, and D. M. Stamper-Kurn, “*Long-time-scale dynamics of spin textures in a degenerate $F = 1$ ^{87}Rb spinor Bose gas*”, Phys. Rev. A **84**, 063625 (2011).
- [53] J. Kronjäger, C. Becker, P. Soltan-Panahi, K. Bongs, and K. Sengstock, “*Spontaneous pattern formation in an antiferromagnetic quantum gas*”, Phys. Rev. Lett., **105**, 090402 (2010).
- [54] E. M. Bookjans, A. Vinit, and C. Raman, “*Quantum Phase Transition in an Antiferromagnetic Spinor Bose-Einstein Condensate*”, Phys. Rev. Lett. **107**, 195306 (2011).
- [55] A. Vinit, E. M. Bookjans, C. A. R. Sá de Melo, and C. Raman, “*Antiferromagnetic Spatial Ordering in a Quenched One-dimensional Spinor Gas*”, Phys. Rev. Lett. **110**, 165301 (2013).
- [56] A. Vinit and C. Raman, “*Precise measurements on a quantum phase transition in antiferromagnetic spinor Bose-Einstein condensates*”, Phys. Rev. A **95**, 011603(R) (2017).
- [57] L. Zhao, J. Jiang, T. Tang, M. Webb, and Y. Liu, “*Antiferromagnetic Spinor Condensates in a Two-Dimensional Optical Lattice*”, Phys. Rev. Lett. **114**, 225302 (2015).
- [58] J. Jiang, L. Zhao, S.-T. Wang, Z. Chen, T. Tang, L.-M. Duan, and Y. Liu,

- “*First-order superfluid-to-Mott-insulator phase transitions in spinor condensates*”, Phys. Rev. A **93**, 063607 (2016).
- [59] S. De, D. L. Campbell, R. M. Price, A. Putra, B. M. Anderson, and I. B. Spielman, “*Quenched binary Bose-Einstein condensates: Spin-domain formation and coarsening*”, Phys. Rev. A **89**, 033631 (2014).
- [60] E. Nicklas, M. Karl, M. Hofer, A. Johnson, W. Muessel, H. Strobel, J. Tomkovic, T. Gasenzer, and M. K. Oberthaler, “*Observation of Scaling in the Dynamics of a Strongly Quenched Quantum Gas*”, Phys. Rev. Lett. **115**, 245301 (2015).
- [61] L. W. Clark, L. Feng, and, C. Chin, “*Universal space-time scaling symmetry in the dynamics of bosons across a quantum phase transition*”, Science **354**, 606 (2016).
- [62] J. Choi, M.-S. Heo, and Y. Shin, “*Experimental Apparatus for producing Large ^{23}Na Bose-Einstein condensates*”, J. Korean Phys. Soc. **59**, 211, (2011).
- [63] J. Choi, “*Thermal Phase Fluctuations in a Quasi-2D Bose-Einstein condensate*”, PhD thesis, Seoul National University (2014).
- [64] S.W. Seo, “*Dynamics of Half-Quantum Vortices in a Spinor Bose-Einstein Condensate*”, PhD thesis, Seoul National University (2017).
- [65] M. Sadgrove, Y. Eto, S. Sekine, H. Suzuki, and T. Hirano, “*Ramsey Interferometry Using the Zeeman Sublevels in a Spin-2 Bose Gas*”, J. Phys. Soc. Jpn. **82**, 094002 (2013).

- [66] A. A. Wood, L. M. Bennie, A. Duong, M. Jasperse, L. D. Turner, and R. P. Anderson, “*Magnetic tensor gradiometry using Ramsey interferometry of spinor condensates*”, Phys. Rev. A **92**, 053604 (2015).
- [67] J. J. Sakurai and J. Napolitano, “*Modern Quantum Mechanics, 2nd Edition*”, Pearson Education, Addison-Wesely publishing (1994).
- [68] T. Bienaimé, E. Fava, G. Colzi, C. Mordini, S. Serafini, C. Qu, S. Stringari, G. Lamporesi, and G. Ferrari, “*Spin-dipole oscillation and polarizability of a binary Bose-Einstein condensate near the miscible-immiscible phase transition*”, Phys. Rev. A **94**, 063652 (2016).
- [69] J.H. Kim, S. W. Seo, and Y. Shin, “*Critical Spin Superflow in a Spinor Bose-Einstein Condensate*”, Phys. Rev. Lett. **119**, 185302 (2017).
- [70] C. S. Gerving, T. M. Hoang, B. J. Land, M. Anquez, C. D. Hamley, and M. S. Chapman, “*Non-equilibrium dynamics of an unstable quantum pendulum explored in a spin-1 Bose-Einstein condensate*”, Nat. Comms. **119**, 185302 (2017).
- [71] D. A. Steck, “*Sodium D-lin Data*”, available at <http://steck.us/alkalidata>.
- [72] S. Kim, S.W. Seo, H.-R. Noh, and Y. Shin, “*Optical pumping effect in absorption imaging of $F = 1$ atomic gases*”, Phys. Rev. A **94**, 023625 (2016).
- [73] A. Polkovnikov, K. Sengupta, A. Silva, and M. Vengalattore, “*Nonequilibrium dynamics of closed interacting quantum systems*”, Rev. Mod. Phys. **83**, 863 (2011).
- [74] A. Lamacraft, “*Quantum Quenches in a Spinor Condensate*”, Phys. Rev. Lett. **89**, 023608 (2007).

- [75] M. Uhlmann, R. Schützhold, and U. R. Fischer, “*Vortex Quantum Creation and Winding Number Scaling in a Quenched Spinor Bose Gas*”, Phys. Rev. Lett. **99**, 120407 (2007).
- [76] B. Damski and W. H. Zurek, “*Dynamics of a Quantum Phase Transition in a Ferromagnetic Bose-Einstein Condensate*”, Phys. Rev. Lett. **99**, 130402 (2007).
- [77] D. Rossini, A. Silva, G. Mussardo, and G. E. Santoro, “*Effective Thermal Dynamics Following a Quantum Quench in a Spin Chain*”, Phys. Rev. Lett. **102**, 127204 (2009).
- [78] E. G. Dalla Torre, E. Demler, and A. Polkovnikov, “*Universal Rephasing Dynamics after a Quantum Quench via Sudden Coupling of Two Initially Independent Condensates*”, Phys. Rev. Lett. **110**, 090404 (2013).
- [79] M. Karl, B. Nowak, and T. Gasenzer, “*Tuning universality far from equilibrium*”, Sci. Rep. **3**, 2394 (2013).
- [80] S. Braun, M. Friesdorf, S. S. Hodgman, M. Schreiber, J. P. Ronzheimer, A. Riera, M. del Rey, I. Bloch, J. Eisert, and U. Schneider, “*Emergence of coherence and the dynamics of quantum phase transitions*”, Proc. Natl. Acad. Sci. USA **112**, 3641 (2015).
- [81] M. Anquez, B. A. Robbins, H. M. Bharath, M. Boguslawski, T. M. Hoang, and M. S. Chapman, “*Quantum Kibble-Zurek Mechanism in a Spin-1 Bose-Einstein Condensate*”, Phys. Rev. Lett. **116**, 155301 (2016).
- [82] F. Zhou, “*Spin Correlation and Discrete Symmetry in Spinor Bose-Einstein Condensates*”, Phys. Rev. Lett. **87**, 080401 (2001).

- [83] F. Zhou, “*Quantum spin nematic states in Bose-Einstein condensates*”, Int. J. Mod. Phys. B **17**, 2643 (2003).
- [84] S. W. Seo, W. J. Kwon, S. Kang, and Y. Shin, “*Collisional Dynamics of Half-Quantum Vortices in a Spinor Bose-Einstein condensate*”, Phys. Rev. Lett. **116**, 185301 (2016).
- [85] S. Uchino, M. Kobayashi, and M. Ueda, “*Bogoliubov theory and Lee-Huang-Yang corrections in spin-1 and spin-2 Bose-Einstein condensates in the presence of the quadratic Zeeman effect*”, Phys. Rev. A **81**, 063632 (2010).
- [86] L. Zhao, J. Jiang, T. Tang, M. Webb, and Y. Liu, “*Dynamics in spinor condensates tuned by a microwave dressing field*”, Phys. Rev. A **89**, 023608 (2014).
- [87] A. T. Black, E. Gomez, L. D. Turner, S. Jung, and P. D. Lett, “*Spinor Dynamics in an Antiferromagnetic Spin-1 Condensate*”, Phys. Rev. Lett. **99**, 070403 (2007).
- [88] M. Melé-Messeguer, B. Juliá-Díaz, A. Polls, and L. Santos, “*Thermal spin fluctuations in spinor Bose-Einstein condensates*”, Phys. Rev. A **87**, 033632 (2013).
- [89] M. Erhard, H. Schmaljohann, M. Erhard, J. Krongjäger, K. Bongs, and K. Sengstock, “*Bose-Einstein condensation at constant temperature*”, Phys. Rev. A **70**, 031602(R) (2004).
- [90] K. Fujimoto and M. Tsubota, “*Counterflow instability and turbulence in a spin-1 spinor Bose-Einstein condensate*”, Phys. Rev. A **85**, 033642 (2012).

- [91] K. Fujimoto and M. Tsubota, “*Spin turbulence with small spin magnitude in spin-1 spinor Bose-Einstein condensates*”, Phys. Rev. A **88**, 063628 (2013).
- [92] L. M. Symes, D. Baillie, and P. B. Blakie, “*Static structure factors for a spin-1 Bose-Einstein condensate*”, Phys. Rev. A **89**, 053628 (2014).
- [93] H.-J. Miesner, D. M. Stamper-Kurn, J. Stenger, S. Inouye, A. P. Chikkatur, and W. Ketterle, “*Observation of Metastable States in Spinor Bose-Einstein Condensates*”, Phys. Rev. Lett. **82**, 2228 (1999).
- [94] Y. Shin, M. Saba, A. Schirotzek, T. A. Pasquini, A. E. Leanhardt, D. E. Pritchard, and W. Ketterle, “*Distillation of Bose-Einstein Condensates in a Double-Well Potential*”, Phys. Rev. Lett. **92**, 150401 (2004).
- [95] J. M. McGuirk, D. M. Harber, H. J. Lewandowski, and E. A. Cornell, “*Normal-Superfluid Interaction Dynamics in a Spinor Bose Gas*”, Phys. Rev. Lett. **91**, 150402 (2003).
- [96] T. Świslocki, E. Witkowska, J. Dziarmaga, and M. Matuszewski, “*Double Universality of a Quantum Phase Transition in Spinor Condensates: Modification of the Kibble-Zurek Mechanism by a Conservation Law*”, Phys. Rev. Lett. **110**, 045303 (2013).
- [97] W.J. Kwon, G. Moon, J. Choi, S.W. Seo, and Y. Shin, “*Relaxation of superfluid turbulence in highly oblate Bose-Einstein condensates*”, Phys. Rev. A **90**, 063627 (2014).
- [98] M. Matuszewski, “*Rotonlike Instability and Pattern Formation in Spinor Bose-Einstein Condensates*”, Phys. Rev. Lett. **105**, 020405 (2010).

- [99] K. Fujimoto and M. Tsubota, “*Direct and inverse cascades of spin-wave turbulence in spin-1 ferromagnetic spinor Bose-Einstein condensates*”, Phys. Rev. A **93**, 033620 (2016).
- [100] H. Saito, Y. Kawaguchi, and M. Ueda, “*Kibble-Zurek mechanism in a quenched ferromagnetic Bose-Einstein condensate*”, Phys. Rev. A **76**, 043613 (2007).
- [101] M. Vengalattore, S. R. Leslie, J. Guzman, and D. M. Stamper-Kurn, “*Spontaneously Modulated Spin Textures in a Dipolar Spinor Bose-Einstein Condensate*”, Phys. Rev. Lett. **100**, 170403 (2008).
- [102] K. Fujimoto and M. Tsubota, “*Spin turbulence in a trapped spin-1 spinor Bose-Einstein condensate*”, Phys. Rev. A **85**, 053641 (2012).
- [103] B. Villaseñor, R. Zamora-Zamora, D. Ernal, and V. Romero-Rochín, “*Quantum turbulence by vortex stirring in a spinor Bose-Einstein condensate*”, Phys. Rev. A **89**, 033611 (2014).
- [104] L. A. Williamson and P. B. Blakie, “*Universal Coarsening Dynamics of a Quenched Ferromagnetic Spin-1 Condensate*”, Phys. Rev. Lett. **116**, 025301 (2016).
- [105] A. Vilenkin, “*Cosmic strings and domain walls*”, Phys. Rep. **121**, 263 (1985).
- [106] M. M. Salomaa, “*Monopoles in the rotating superfluid helium-3 A-B interface*”, Nature **326**, 367 (1987).
- [107] D. I. Bradley, S. N. Fisher, A. M. Guénault, R. P. Haley, J. Kopu, H. Martin, G. R. Pickett, J. E. Roberts, and V. Tsepelin, “*Relic topological de-*

- fects from brane annihilation simulated in superfluid ^3He* ", Nat. Phys. **4**, 46 (2008).
- [108] J. A. Bert, B. Kalisky, C. Bell, M. Kim, Y. Hikita, H. Y. Hwang, and K. A. Moler, "*Direct imaging of the coexistence of ferromagnetism and superconductivity at the $\text{LaAlO}_3/\text{SrTiO}_3$ interface*", Nat. Phys. **7**, 767 (2011).
- [109] M. O. Borgh and J. Ruostekoski, "*Topological Interface Engineering and Defect Crossing in Ultracold Atomic Gases*", Phys. Rev. Lett. **109**, 015302 (2012).
- [110] M. O. Borgh and J. Ruostekoski, "*Topological interface physics of defects and textures in spinor Bose-Einstein condensates*", Phys. Rev. A **87**, 033617 (2013).
- [111] H. Takeuchi, K. Kasamatsu, M. Tsubota, and M. Nitta, "*Tachyon Condensation Due to Domain-Wall Annihilation in Bose-Einstein Condensates*", Phys. Rev. Lett. **109**, 245301 (2012).
- [112] O. D. Lavrentovich and S. S. Rozhkov, "*Strings with boojums at their ends: topological defects of a new type in nematic liquid crystals*", JETP Lett. **47**, 258 (1988).
- [113] Y. Kondo, J. S. Korhonen, M. Krusius, V. V. Dmitriev, E. V. Thuneberg, and G. E. Volovik, "*Combined Spin-Mass Vortex with Soliton Tail in Superfluid $^3\text{He} - B$* ", Phys. Rev. Lett. **68**, 3331 (1992).
- [114] J. S. Korhonen, Y. Kondo, M. Krusius, E. V. Thuneberg, and G. E. Volovik, "*Combined Spin-Mass Vortex with Soliton Tail in Superfluid $^3\text{He} - B$* ", Phys. Rev. Lett. **68**, 3331 (1993).

- [115] A. J. A. James and A. Lamacraft, “*Phase Diagram of Two-Dimensional Polar Condensates in a Magnetic Field*”, Phys. Rev. Lett. **106**, 140402 (2011).
- [116] J. W. Kirchner, “*Aliasing in $1/f^\alpha$ noise spectra: Origins, consequences, and remedies*”, Phys. Rev. A **71**, 066110 (2005).
- [117] G. I. Mias, N. R. Cooper, and S. M. Girvin, “*Quantum noise, scaling, and domain formation in a spinor Bose-Einstein condensate*”, Phys. Rev. A **77**, 023616 (2008).
- [118] J. D. Sau, S. R. Leslie, D. M. Stamper-Kurn, and M. L. Cohen, “*Theory of domain formation in inhomogeneous ferromagnetic dipolar condensates within the truncated Wigner approximation*”, Phys. Rev. A **80**, 023622 (2009).
- [119] H. E. Nistazakis, D. J. Frantzeskakis, P. G. Kevrekidis, B. A. Malomed, and R. Carretero-González “*Bright-dark soliton complexes in spinor Bose-Einstein condensates*”, Phys. Rev. A **77**, 033612 (2008).
- [120] B. Xiong and J. Gong, “*Dynamical creation of complex vector solitons in spinor Bose-Einstein condensates*”, Phys. Rev. A **81**, 033618 (2010).
- [121] T. M. Bersano, V. Gokhroo, M. A. Khamehchi, J. D’Ambroise, D. J. Frantzeskakis, P. Engels, and P. G. Kevrekidis, “*Three-component Soliton States in Spinor $F = 1$ Bose-Einstein Condensates*”, Phys. Rev. Lett. **120**, 063202 (2018).
- [122] M. Uchiyama, J. Ieda, and M. Wadati, “*Dark Solitons in $F = 1$ Spinor Bose-Einstein Condensate*”, J. Phys. Soc. Jpn. **75**, 064002 (2006).

- [123] D. L. Feder, M. S. Pindzola, L. A. Collins, B. I. Schneider, and C. W. Clark, “*Dark-Soliton states of Bose-Einstein condensates in anisotropic traps*”, Phys. Rev. A **62**, 053606 (2000).
- [124] Z. Dutton, M. Budde, C. Slowe, and L. V. Hau, “*Observation of Quantum Shock Waves Created with Ultra-Compressed Slow Light Pulses in a Bose-Einstein Condensate*”, Science **293**, 663 (2001).
- [125] G. Huang, V. A. Makarov, and M. G. Velarde, “*Two-dimensional solitons in Bose-Einstein condensates with a disk-shaped trap*”, Phys. Rev. A **67**, 023604 (2003).
- [126] C.-L. Hung, X. Zhang, L.-C. Ha, S.-K. Tung, N. Gemelke, and C. Chin, “*Extracting density–density correlations from in situ images of atomic quantum gases*”, New. J. Phys. **13**, 075019 (2011).
- [127] S. W. Seo, J. Choi, and Y. Shin, “*Scaling behavior of density fluctuations in an expanding quasi-two-dimensional degenerate Bose gas*”, Phys. Rev. A **89**, 043606 (2014).
- [128] S. W. Seo, B. Ko, J. H. Kim, and Y. Shin, “*Observation of vortex-antivortex pairing in decaying 2D turbulence of a superfluid gas*”, Sci. Rep. **7**, 4587 (2017).
- [129] T. Kanai, W. Guo, and M. Tsubota, “*Flows with fractional quantum circulation in Bose-Einstein condensates induced by nontopological phase defects*”, Phys. Rev. A **97**, 013612 (2018).
- [130] J. D. Sau, S. R. Leslie, M. L. Cohen, and D. M. Stamper-Kurn, “*Spin*

- squeezing of high-spin, spatially extended quantum fields*”, New. J. Phys. **12**, 085011 (2010).
- [131] A. L. Fetter, “*Rotating trapped Bose-Einstein condensates*”, Rev. Mod. Phys. **81**, 647 (2009).
- [132] M. R. Matthews, B. P. Anderson, P. C. Haljan, D. S. Hall, C. E. Wieman, and E. A. Cornell, “*Vortices in a Bose-Einstein Condensate*”, Phys. Rev. Lett. **83**, 2498 (1999).
- [133] A. E. Leanhardt, A. Görlitz, A. P. Chikkatur, D. Kielpinski, Y. Shin, D. E. Pritchard, and W. Ketterle, “*Imprinting Vortices in a Bose-Einstein Condensate using Topological Phases*”, Phys. Rev. Lett. **89**, 190403 (2002).
- [134] K. W. Madison, F. Chevy, W. Wohlleben, and J. Dalibard, “*Vortex Formation in a Stirred Bose-Einstein Condensate*”, Phys. Rev. Lett. **84**, 806 (2000).
- [135] J. R. Abo-Shaeer, C. Raman, J. M. Vogels, and W. Ketterle, “*Observation of Vortex Lattices in Bose-Einstein Condensates*”, Science **292**, 476 (2001).
- [136] K. W. Madison, F. Chevy, V. Bretin, and J. Dalibard, “*Stationary States of a Rotating Bose-Einstein Condensate: Routes to Vortex Nucleation*”, Phys. Rev. Lett. **86**, 210403 (2001).
- [137] C. Raman, J. R. Abo-Shaeer, J. M. Vogels, K. Xu, and W. Ketterle, “*Imprinting Vortices in a Bose-Einstein Condensate using Topological Phases*”, Phys. Rev. Lett. **87**, 210402 (2001).

- [138] E. Hodby, G. Hechenblaikner, S. A. Hopkins, O. M. Maragó, and C. J. Foot, “*Vortex Nucleation in Bose-Einstein Condensates in an Oblate, Purely Magnetic Potential*”, Phys. Rev. Lett. **88**, 010405 (2001).
- [139] P. C. Haljan, I. Coddington, P. Engels, and E. A. Cornell, “*Driving Bose-Einstein-Condensate Vorticity with a Rotating Normal Cloud*”, Phys. Rev. Lett. **87**, 210403 (2001).
- [140] N. R. Cooper, N. K. Wilkin, and J. M. F. Gunn, “*Quantum Phases of Vortices in Rotating Bose-Einstein Condensates*”, Phys. Rev. Lett. **87**, 120405 (2001).
- [141] V. Schweikhard, I. Coddington, P. Engels, V. P. Mogendorff, and E. A. Cornell, “*Rapidly Rotating Bose-Einstein Condensates in and near the Lowest Landau Level*”, Phys. Rev. Lett. **92**, 040404 (2004).
- [142] V. Bretin, S. Stock, Y. Seurin, and J. Dalibard, “*Fast Rotation of a Bose-Einstein Condensate*”, Phys. Rev. Lett. **92**, 050403 (2004).
- [143] M. Roncaglia, M. Rizzi, and J. Dalibard, “*From rotating atomic rings to quantum Hall states*”, Sci. Rep. **1**, 43 (2011).
- [144] K.-P. Marzlin and W. Zhang, “*Quantized circular motion of a trapped Bose-Einstein condensate: Coherent rotation and vortices*”, Phys. Rev. A **57**, 4761 (1998).
- [145] H. Ott, J. Fortágh, S. Kraft, A. Günther, D. Komma, and C. Zimmermann, “*Nonlinear Dynamics of a Bose-Einstein Condensate in a Magnetic Waveguide*”, Phys. Rev. Lett. **57**, 4761 (1998).

- [146] E. Lundh, A. Collin, and K.-A. Suominen, “*Rotational States of Bose Gases with Attractive Interactions in Anharmonic Traps*”, Phys. Rev. Lett. **92**, 070401 (2004).
- [147] G.-Q. Li, L.-B. Fu, J.-K. Xue, X.-Z. Chen, and J. Liu, “*Collective excitations of a Bose-Einstein condensate in an anharmonic trap*”, Phys. Rev. A **74**, 055601 (2006).
- [148] M.-S.Heo, J. Choi, Y. Shin, “*Fast production of large ^{23}Na Bose-Einstein condensates in an optically plugged magnetic quadrupole trap*”, Phys. Rev. A **83**, 013622 (2011).
- [149] S. Stringari, “*Collective Excitations of a Trapped Bose-Condensed Gas*”, Phys. Rev. Lett. **77**, 2360 (1996).
- [150] R. Onofrio, D. S. Durfee, C. Raman, M. Köhl, C. E. Kuklewicz, and W. Ketterle, “*Surface Excitations of a Bose-Einstein Condensate*”, Phys. Rev. Lett. **84**, 810 (2000).
- [151] F. Dalfovo and Stringari, “*Shape deformations and angular-momentum transfer in trapped Bose-Einstein condensates*”, Phys. Rev. A **63**, 011601 (2000).
- [152] A. Recati, F. Zambelli, and S. Stringari, “*Overcritical Rotation of a Trapped Bose-Einstein Condensate*”, Phys. Rev. Lett. **86**, 377 (2001).
- [153] S. Sinha and Y. Castin, “*Dynamic Instability of a Rotating Bose-Einstein Condensate*”, Phys. Rev. Lett. **87**, 190402 (2001).
- [154] M. Tsubota, K. Kasamatsu, and M. Ueda, “*Vortex lattice formation in a rotating Bose-Einstein condensate*”, Phys. Rev. A **65**, 023603(2002).

- [155] K. Kasamatsu, M. Tsubota, and M. Ueda, “*Nonlinear dynamics of vortex lattice formation in a rotating Bose-Einstein condensate*”, Phys. Rev. A **67**, 033610 (2003).
- [156] E. Lundh, J.-P. Martikainen, and K.-A. Suominen, “*Vortex nucleation in Bose-Einstein condensates in time-dependent traps*”, Phys. Rev. A **67**, 063604 (2003).
- [157] C. Lobo, A. Sinatra, and Y. Castin, “*Vortex Lattice Formation in Bose-Einstein Condensates*”, Phys. Rev. Lett. **92**, 020403 (2004).
- [158] N. G. Parker and C. S. Adams, “*Emergence and Decay of Turbulence in Stirred Atomic Bose-Einstein Condensates*”, Phys. Rev. Lett. **95**, 145301 (2005).
- [159] D. Guéry-Odelin, “*Spinning up and down a Boltzmann gas*”, Phys. Rev. A **62**, 033607 (2000).
- [160] E. Lundh, “*Multiply quantized vortices in trapped Bose-Einstein condensates*”, Phys. Rev. A **65**, 043604 (2002).
- [161] G. M. Kavoulakis and G. Baym, “*Rapidly rotating Bose-Einstein condensates in anharmonic potentials*”, New J. Phys. **5**, 51 (2003).
- [162] E. Tiesinga, C. J. Williams, P. S. Julienne, K. M. Jones, P. D. Lett, and W. D. Phillips, “*A Spectroscopic Determination of Scattering Lengths for Sodium Atom Collisions*”, J. Res. Natl. Inst. Stand. Technol. **101**, 505 (1996).

- [163] H.-J. Miesner, D. M. Stamper-Kurn, M. R. Andrews, D. S. Durfee, S. Inouye, and W. Ketterle, “*Bosonic Stimulation in the Formation of a Bose-Einstein Condensate*”, *Science* **279**, 1005 (1998).
- [164] J. E. Williams, E. Zaremba, B. Jackson, T. Nikuni, and A. Griffin, “*Dynamical Instability of a Condensate Induced by a Rotating Thermal Gas*”, *Phys. Rev. Lett.* **88**, 070401 (2002).
- [165] A. A. Penckwitt, R.J. Ballagh, and C. W. Gardiner, “*Nucleation, Growth, and Stabilization of Bose-Einstein Condensate Vortex Lattices*”, *Phys. Rev. Lett.* **88**, 070401 (2002).
- [166] M. V. Berry, “*Quantal phase factors accompanying adiabatic changes*”, *Proc. R. Soc. Lond. A* **392**, 45 (1984).
- [167] A. Shapere and F. Wilcze, “*Geometric Phase in Physics*”, World Scientific, Singapore (1989).
- [168] A. Stern, “*Berry’s phase, motive forces, and mesoscopic conductivity*”, *Phys. Rev. Lett.* **68**, 1022 (1992).
- [169] T.-L. Ho and V. B. Shenoy, “*Local Spin-Gauge Symmetry of the Bose-Einstein Condensates in Atomic Gases*”, *Phys. Rev. Lett.* **77**, 2595 (1996).
- [170] F. Zambellie and S. Stringari, “*Quantized Vortices and Collective Oscillations of a Trapped Bose-Einstein Condensate*”, *Phys. Rev. Lett.* **81**, 1754 (1998).
- [171] F. Chevy, K. W. Madison, and J. Dalibard, “*Measurement of the Angular Momentum of a Rotating Bose-Einstein Condensate*”, *Phys. Rev. Lett.* **85**, 2223 (2000).

- [172] C. Ryu, M. F. Andersen, P. Cladé, V. Natarajan, K. Helmerson, and W. D. Phillips, “*Observation of Persistent Flow of a Bose-Einstein Condensate in a Toroidal Trap*”, Phys. Rev. Lett. **99**, 260401 (2007).
- [173] A. Ramanathan, K. C. Wright, S. R. Muniz, M. Zelan, W. T. Hill, C. J. Lobb, K. Helmerson, W. D. Phillips, and G. K. Campbell, “*Superflow in a Toroidal Bose-Einstein Condensate: An Atom Circuit with a Tunable Weak Link*”, Phys. Rev. Lett. **106**, 130401 (2011).
- [174] S. Beattie, S. Moulder, R. J. Fletcher, and Z. Hadzibabic, “*Persistent Currents in Spinor Condensates*”, Phys. Rev. Lett. **110**, 025301 (2013).
- [175] I. Lesanovsky and W. von Klitzing, “*Time-Averaged Adiabatic Potentials: Versatile Matter-Wave Guides and Atom Traps*”, Phys. Rev. Lett. **99**, 083001(2007).
- [176] B. E. Sherlock, M. Gildemeister, E. Owen, E. Nugent, and C. J. Foot, “*Time-averaged adiabatic ring potential for ultracold atoms*”, Phys. Rev. Lett. **83**, 043408 (2011).
- [177] J. Choi, S. Kang, S. W. Seo, W. J. Kwon, and Y. Shin, “*Observation of a Geometric Hall Effect in a Spinor Bose-Einstein Condensate with a Skyrmion Spin Texture*”, Phys. Rev. Lett. **111**, 245301 (2013).
- [178] Y.-a. Liao, A. S. C. Rittner, T. Paprotta, W. Li, G. B. Partridge, R. G. Hulet, S. K. Baur & E. J. Muller, “*Spin-imbalance in a one-dimensional Fermi gas*”, Nature **467**, 567 (2010).
- [179] K. G. Wilson, “*Renormalization Group and Critical Phenomena. I. Renor-*

malization Group and the Kadanoff Scaling Picturen”, Physics Review B, **4**, 3174 (1971).

[180] N. Goldenfeld, “*Lecture on Phase Transitions and the Renormalization Group*”, Addison-Welsey publishing (1992).

초 록

비 평형 동역학은 시간에 따른 강한 외부 자극이나, 보존되지 않는 물리량, 에너지의 흐름 등의 정의가 어려운 복잡한 요소로 인해 이론적인 접근이 쉽지 않다. 그렇기 때문에 비 평형 계에 대한 연구는 통계역학적 이해도가 높은 평형 계의 물리 법칙을 비 평형 계로 확장시키는 방향으로 연구되어 왔다. 이러한 노력 중 진전이 있는 분야는 상 전이 동역학 분야이다. 상 전이 동역학 연구는 어떤 과정을 통해 계의 새로운 안정적인 상태에 도달할 것인지, 어떤 들뜸 상태(excitations)가 얼마나 나타날지 등에 초점이 맞춰져 있다. 임 계점 근처의 평형 계는 상관 길이(correlation length), 공간 차원(dimension), 질서 변수의 대칭성(the symmetry of order parameter)에 의해 모든 통계역학적 물리량의 특이점이 스케일링 양상으로 나타난다는 스케일링 가정(scaling hypothesis)으로 기술된다. 이러한 스케일링 가정은 비 평형 상태의 상 전이 동역학에도 적용될 수 있음이 잘 알려져 있고 더 나아가 계의 보편성(universality)를 찾으려는 노력이 계속되고 있다. 또한, 상 전이를 일으키는 들뜸 상태는 그 계의 질서 변수 다양체의 대칭성에 의해 나타나는 위상적 결함(topological defects)이 생성되는 것으로 확인 할 수 있음이 잘 알려져 있다.

전형적인 상 전이 동역학 연구 방법은 양자적 켄치(quantum quench)로 이는 계의 해밀토니안을 갑자기 변화시켜 기저 상태였던 계를 들뜬 상태에서 새로운 상태로 가는 것을 관찰하는 방법이다. 하지만, 다 체계 양자 시스템에서 이러한 비 평형 상태의 이론적 연구와 계사는 너무 복잡하기 때문에 실험적인 방법이 필요하다. 이를 위해서는 주변 환경의 영향을 받지 않는 고립된 계가 필요하고, 외부 변수들을 통제할 수 있는 연구 환경을 갖춰야 한다. 극저온 양자기체 계는 외부 자기장과 전자기파를 이용하여 변수들을 비교적 쉽게 조절할 수 있고 충분히 오랜 시간동안 결맞음이 유지될 정도로 외부 환경으로부터 영향을 받지

않는 계로 비 평형 상 전이 동역학을 연구하는 최적의 연구 환경을 제공한다.

이러한 배경을 바탕으로 이 학위 논문에서는 반 강자성 상호작용(antiferromagnetic)을 갖는 준 2차원 스피너 보즈-아인슈타인 응집체(spinor BEC)에서 나타나는 두 방향의 상 전이 동역학에 대한 연구를 다룬다. 반 강자성 스피너 BEC에서 나타나는 위상(phase)은 quadratic Zeeman energy에 의해 easy-axis polar 상(EAP phase)과 easy-plane polar 상(EPP phase)으로 결정된다. 우리는 microwave dressing 기술을 이용하여 이차 Zeeman energy를 조절하여 급작스러운 상 전이 동역학 과정에 접근하였다.

EAP 상에서 EPP 상으로의 상 전이(The EAP-to-EPP phase transition)의 초반의 평균장 이론에 의해 수평방향의 마그논(transverse magnon)이 들뜨면서 동적 불안정성에 의해 진행된다. 이러한 초반 동역학은 스핀 난류가 생성되면서 벗어나게 된다. 그러나 평균장 이론에 의한 초반의 공간적인 스케일링 양상은 스핀 난류의 생성 과정에서 계속 유지가 되며, 시간 상의 스케일링 또한 존재하였다. 계가 안정화됨에 따라 스핀 난류가 사라지고 상 전이의 결과로 위상적 결함인 반 양자수 소용돌이 (half-quantum vortex, HQV)를 확인하였다.

EPP 상에서는 에너지 갭이 있는 수평방향의 마그논 이외에도 에너지 갭이 없는 자기장 축 방향의 마그논 들뜸(gapless axial magnon excitation)에 의해 스핀 요동(spin fluctuations)이 생길 수 있다. 아무런 스핀 요동이 없는 경우, EPP 상에서 EAP 상으로의 상 전이(The EPP-to-EAP phase transition)는 앞서 the EAP-to-EPP 상 전이와 마찬가지로 초반 동역학은 평균장 이론에 의해 스케일링 양상이 나타나며, 상 전이 동역학의 결과로 순환이 1인 양자 소용돌이 (singly charged quantum vortex)를 확인할 수 있다. 하지만, 특이하게도 2차원 반 강자성 스피너 BEC에서만 나타날 수 있는 한 끝이 HQV로 끝나는 솔리톤 (soliton terminated by HQVs)이 나타나는 것을 관측하였다. 이러한 위상 물체를 magnetic composite-soliton(MCS)이라 명명하고 이를 Bragg spectroscopy와 Stern-Gerlach imaging을 이용하여 구조를 분석하였다. MCS는 BEC 내부의 흐

름에 의해 점점 작은 위상 물체로 쪼개지며 특정 조건에서 양자 소용돌이가 될 수 있다. 이 경우, 양자 소용돌이의 핵(core) 부분이 자성(magnetization)을 가질 수 있다. 또한, 마지막으로 gapless axial magnon excitation을 이용하여 스핀 요동이 동역학 불안정성에 어떠한 영향을 주는지 관측하였다.

2차원의 낮은 차원에서는 열적 요동이 먼 거리 질서도(long-range order)를 파괴하여 질서 변수가 정의되지 못하지만, 준 먼 거리 질서도(quasi long-range order)에 의해 상 전이 현상이 존재할 수 있음이 알려져 있다. 이를 Berezinskii-Kosterlitz Thouless(BKT) 상 전이라고 부른다. MCS는 spin-1 BEC에서 나타나는 BKT 상전이를 매개하는 매개체로서 우리의 관측결과는 paired superfluidity의 가능성을 보여주는 첫 증거라고 볼 수 있다.

이 논문은 스칼라 BEC에서 스커미온(Skyrmion) 스핀 구조를 이용한 QV 격자 구조 생성 과정에 관한 연구도 포함하고 있다. 스커미온 스핀 구조는 스핀들이 공간적으로 변화하고 있기 때문에 Berry 곡률이 유한한 값을 갖게 되고 중성 원자는 기하학적인 전자기력을 받는다. 우리는 사중극 자기장을 이용해 스칼라 BEC 시료에 기하학적 자기력을 가하였고 비 조화 우물(anharmonic trapping potential)에 갇힌 스칼라 BEC 전체가 회전하는 움직임이 초유체 내부의 회전에 의해 변화하는 과정과 주변의 열적 기체(thermal cloud)의 영향을 확인하였다. 또한, 기하학적 홀 효과의 방향 비대칭성(chirality of geometrical Hall effect)을 관측하였다.

주요어 : 반강자성 스피너 보즈-아인슈타인 응집체, 상 전이, 스케일링 가설, 스핀 양자 난류, 위상적 결합, 양자 요동.

학 번 : 2012-20353

Publication List

SCI Journals

- [1] J. Choi, S. Kang, and Y. Shin, “*Observation of a Geometric Hall Effect in a Spinor BEC with a Skyrmion Spin Texture*”, Physical Review Letters **111**, 245301 (2013).
- [2] S. Kang, J. Choi, S.W. Seo, W.J. Kwon, and Y. Shin, “*Rotating a BEC by shaking an anharmonic axisymmetric magnetic potential*”, Physical Review A **91**, 013603 (2015).
- [3] S.W. Seo, S. Kang, W. J. Kwon, and Y. Shin, “*Half-Quantum Vortices in an Antiferromagnetic Spinor Bose-Einstein Condensate*”, Physical Review Letters **115**, 015301 (2015).
- [4] S. Kang, S.W. Seo, J.H. Kim, and Y. Shin, “*Emergence and scaling of spin turbulence in quenched antiferromagnetic spinor BECs*”, Physical Review A **95**, 053638 (2017).
- [5] S. Kang, and Y. Shin, “*Observation of magnetic composite-solitons in an quasi-2D antiferromagnetic spinor Bose-Einstein condensate*”, arxiv: (2018).
- [6] S. Kang, and Y. Shin, “*Suppressing the amplification of the transverse spin fluctuations by the axial spin fluctuations*”, in preparation (2018).

Appendix

Appendix A

Scaling hypothesis

Near the critical point, the order parameter susceptibility $\chi \sim (\langle\phi^2\rangle - \langle\phi\rangle^2)$ diverges and the spatial fluctuations become strong and long-range, assuming $\xi = \xi_{\pm}|q|^{-\nu}$ as $|q| \rightarrow 0$ with $\nu > 0$. Then we may write f with the Landau-Ginzburg-Wilson Hamiltonian [180] as

$$\begin{aligned}\frac{f}{k_B T} &= \frac{\mathcal{H}[\mathcal{S}]}{k_B T} = \int d^d x \left[\frac{r}{2} S(\vec{x})^2 + \frac{1}{2} [\vec{\nabla} S(\vec{x})]^2 + \frac{u}{4} S(\vec{x})^4 - b(\vec{x} S(\vec{x})) \right] \\ &\sim \xi^{-d} (A_0 + A_1 \left(\frac{l_i}{\xi}\right)^\sigma + \dots),\end{aligned}$$

where $S(\vec{x})$ is a local order parameter satisfying $\phi = \langle S \rangle$, $r = a(Q - Q_c)$ with $a > 0$, σ is non-negative exponent, l_i s are certain local length scales and A_i s are coefficients with weak temperature dependence in d dimensions. Therefore, the two-point order parameter correlation function $G(\vec{x}) = \langle S(\vec{x})S(0) \rangle - \phi^2$ and thermodynamic susceptibility becomes

$$\begin{aligned}G(q, \vec{k}) &= \int \frac{d^d x}{(2\pi)^d} G(q, \vec{x}) e^{-i\vec{k}\cdot\vec{x}} = \int \frac{d^d x}{(2\pi)^d} |\vec{x}|^{(d-2-\eta)} \tilde{G}_{\pm}(\vec{x}/\xi) \\ &= |\vec{k}|^{(-2+\eta)} \tilde{G}_{\pm}(\vec{k}\xi), \\ \chi(q, \vec{k}) &\sim \xi^{2-\eta} \sim |q|^{-\gamma} \text{ as } \vec{k} \rightarrow 0,\end{aligned}$$

yielding the hyperscaling relations of $\alpha = 2 - d\nu$, $\beta = \nu(d - 2 + \eta)/2$, and $\delta = (d + 2 - \eta)/(d - 2 + \eta)$. This manifests the salient point of the scaling hypothesis: everything can be expressed in terms of ξ , invariant under scale transformation near the critical point. The insensitivity to the length transformation identifies the fixed point of the transformation and leads to the renormalization group method [179].

Appendix B

Calculation of quantum depletion

Quantum depletion represents the excitation number of quasi-particles, containing even no real excitations, induced by the interaction. Consider the case of an antiferromagnetic $F = 1$ neutral atoms (Eqn. 3.3). For the EAP phase, the quantum depletion is given as

$$\frac{N - N_0}{N} = \frac{1}{N} \sum_{\mathbf{k} \neq 0} \langle \hat{a}_{0,\mathbf{k}} a_{0,\mathbf{k}}^\dagger + \hat{a}_{+1,\mathbf{k}} a_{+1,\mathbf{k}}^\dagger + \hat{a}_{-1,\mathbf{k}} a_{-1,\mathbf{k}}^\dagger \rangle \quad (\text{B.1})$$

$$= \frac{\sqrt{m^3}}{3\pi^2 \hbar^3} (\sqrt{nc_0^2} + 2\sqrt{n|c_2|^3}) \times f((q/c_2n - 1) + \text{sgn}(c_2)),$$

where $f(t) \equiv \frac{3}{\sqrt{2}} \int dx \left(\frac{x^2 + t + 1}{\sqrt{(x^2 + t)(x^2 + t + 2)}} - 1 \right) x^2.$ (B.2)

For $q < 0$ the quantum depletion is given as

$$\frac{N - N_0}{N} = \frac{\sqrt{m^3}}{3\pi^2 \hbar^3} (\sqrt{nc_0^2} + \sqrt{n|c_2|^3}) \times (1 + f(|q|/c_2n)). \quad (\text{B.3})$$

Above result is obtained from Ref. [85].

In our experiments, we are only interested in the part, which is related to the transverse magnon modes. Therefore, the quantum depletion can be rewritten as

$$\begin{aligned} n_{\pm 1} &= \frac{1}{(2\pi)^3} \int d\mathbf{k} \langle \hat{n}_{\pm 1}(\mathbf{k}) \rangle \\ &= \frac{1}{(2\pi)^3} \int d\mathbf{k} \langle \delta \hat{\Psi}_{\pm 1}(\mathbf{k})^\dagger \delta \hat{\Psi}_{\pm 1}(\mathbf{k}) \rangle. \end{aligned} \quad (\text{B.4})$$

According to Ref. [88], by taking account of the Bose statistics for normal gas,

$$\langle \hat{n}_{\pm 1}(k, T) \rangle = \frac{\varepsilon_k}{E_k} \frac{1}{e^{\beta E_k} - 1} + \frac{\varepsilon_k}{2E_k} - \frac{1}{2}, \quad (\text{B.5})$$

where $\beta = 1/k_B T$, k_B is the Boltzmann constant, and $\varepsilon_k = \hbar^2 k^2 / 2M$. We only consider the temperature-independent terms. Then, we get

$$n_{\pm 1} = 4\pi k_0^3 \int dx \left(\frac{(x^2 + 1)}{2\sqrt{x^2(x^2 + 2)}} - \frac{1}{2} \right) x^2, \quad (\text{B.6})$$

where $k_0 = \sqrt{2|c_2|nm}/\hbar$. In our experiments, we assume that the spin fluctuation is identical for each sequence. Mathematica code is written in below.

```

ln[28]:= h = 6.626 * 10^-34;
hbar = h / 2 / pi;
kb = 1.38 * 10^-23;
m0 = 1.66 * 10^-27;
a0 = 5.292 * 10^-11;
u = 10^-6;
mRb = 87 m0;

mNa = 23 m0;
a = 2.75 * 10^-9;
c0 =  $\frac{4 \pi \hbar^2 a}{mNa}$ ;
c2 =  $\frac{4 \pi \hbar^2}{3 mNa} 2.47 a0$ ;
wx = 3.8 * 2 pi; wy = 5.5 * 2 pi; wz = 402 * 2 pi;
TotalM = 8.8 * 10^6; (*total atom number*)
M = TotalM 0.9; (*bec atom number*)
wbar = (wx wy wz)^1/3; (*average frequency of xyz axis*)
mu =  $\frac{\hbar wbar}{2} \left( \frac{15 M a}{\sqrt{\hbar wbar / mNa / wbar}} \right)^{2/5}$ ;
n =  $\frac{\mu}{c0}$ ;
Rx =  $\sqrt{\frac{2 \mu}{mNa wx^2}}$ ; Ry =  $\sqrt{\frac{2 \mu}{mNa wy^2}}$ ; Rz =  $\sqrt{\frac{2 \mu}{mNa wz^2}}$ ;
nNa[x_, y_, z_] := n  $\left( 1 - \frac{x^2}{Rx^2} - \frac{y^2}{Ry^2} - \frac{z^2}{Rz^2} \right)$ 
Tc = 0.94 hbar wbar (TotalM)^1/3 / kb;
TNa = Tc (1 - 0.9)^1/3;
nNa0 = nNa[0, 0, 0];

b0 =  $\frac{4 \pi}{(2 \pi)^3} \left( \frac{2 mNa c2 nNa0}{\hbar^2} \right)^{3/2}$ 
NIntegrate [
  x^2  $\left( \frac{(x^2 + 1)}{\sqrt{x^2 (x^2 + 2)}} \frac{1}{\text{Exp}[\sqrt{x^2 (x^2 + 2)} \frac{c2 nNa0}{kb TNa}] - 1} + \frac{(x^2 + 1)}{2 \sqrt{x^2 (x^2 + 2)}} - \frac{1}{2} \right)$ ,
  {x, 0, infinity}] / nNa0;

constb0 = NIntegrate [x^2  $\left( \frac{(x^2 + 1)}{2 \sqrt{x^2 (x^2 + 2)}} - \frac{1}{2} \right)$ , {x, 0, infinity}];

b0 =  $\frac{4 \pi}{(2 \pi)^3} \left( \frac{2 mNa c2 nNa0}{\hbar^2} \right)^{3/2}$  constb0 / nNa0
(*quantum spin fluctuation*)
b[x_, y_, z_] :=  $\frac{4 \pi}{(2 \pi)^3} \left( \frac{2 mNa c2 nNa[x, y, z]}{\hbar^2} \right)^{3/2}$  constb0 / nNa[x, y, z]
b2[x_, y_, z_] :=  $\frac{4 \pi}{(2 \pi)^3} \left( \frac{2 mNa c2 nNa[x, y, z]}{\hbar^2} \right)^{3/2}$  constb0

```

Out[49]= 3.29816 × 10⁻⁶

Appendix C

Examples of SCPI commands

We use N5185A Function Generator from Agilent to generate microwave pulses. There exist 5 ms delay to perform SCPI commands, after TTL signal. It needs initializing commands before starting experimental sequence such as

```
"TRIG:SOUR EXT ; :INIT:CONT ON ; :FREQ:MODE LIST ;  
LIST:RETR OFF ;"
```

TRIGgger:SOURce EXTernal Choose trigger source as external TTL signal. When TTL signal is positive, a function generator transmits the modulating signal.

:INITiate:CONTiuous ON This command selects restart sweep automatically or wait until the trigger source is received, after the previous sweep is finished. Only single sweep will be performed, if choose **OFF**.

:FREQuency:MODE LIST Select frequency sweep mode. When appropriate trigger source is received, executes the commands to start the LIST or STEP frequency sweep.

:LIST:RETRace OFF The last sweep point is sustained, until the sweep is initiated and triggered again.

Because we generate rapid phase transition and study the relaxation dynamics by changing microwave frequency, the final microwave frequency should be unchanged for long hold times. But, **:LIST:RETR OFF** command affects the next sequence because of 5 ms signal delay by disturbing the initial preparation of the well-defined condensate before quench. Thus, at the end of sequences, we commands the start point of the next sequence using GPIB control.

Example of sweep commands.

```
SWE:DWEL 0.002
SWE:POIN 4
FREQ:STAR 3 MHZ
FREQ:STOP 6 MHZ
```

Then, frequency changes as

Time after TTL signal	Frequency	Time Difference
5 ms	3 MHz	
12 ms	4 MHz	7 ms
19 ms	5 MHz	7 ms
26 ms	6 MHz	7 ms

We confirm that these commands clearly works in the sweep range of a tens of MHz. Minimum dwell time is 5 ms. Therefore, when we set the dwell time of each step as 0.0001 s(=100 μ s), the step dwell time becomes 5.1 ms. If the step dwell time is set to 0.001 s(=1 ms), the actual step dwell time will be 6 ms.

:SWEep:DWELl Set step dwell time.

:SWEep:POINTs Set the number of steps.

:FREQuency:STARt Set the starting frequency of modulating signal.

:FREQuency:STOP Set the final frequency of modulating signal.

Appendix D

Sad history

1.

We were trying to figure out the magnetic field gradient, generated by the grad.z and grad.xy coils. But, since we empirically found the perfect conditions for removing the field inhomogeneity, we did not need the calibration. We guess that the quadrupole zero fields, generated by each grad. coil pairs, are placed as in fig. D(b). Empirically, we minimize the magnetic field gradient following the process: By using one gradient coils, make the Ramsey fringe pattern aligns vertically. Then, remove the field inhomogeneity as possible, by using other coils. Elaborately, tune the both gradient coil pairs to cancel out the field inhomogeneity.

2. We were trying to measure skyrmion decay in a polar BEC. We expected that a skyrmion would be divided into two half-quantum vortices, where the total mass current is zero. The orientation of two HQVs' supercurrents should be opposite. Figure D(d) shows an image of the desired result. However, the experiments wouldn't be completed, because of the technical issues.

A skyrmion spin texture has been imprinted by a quadrupole magnetic

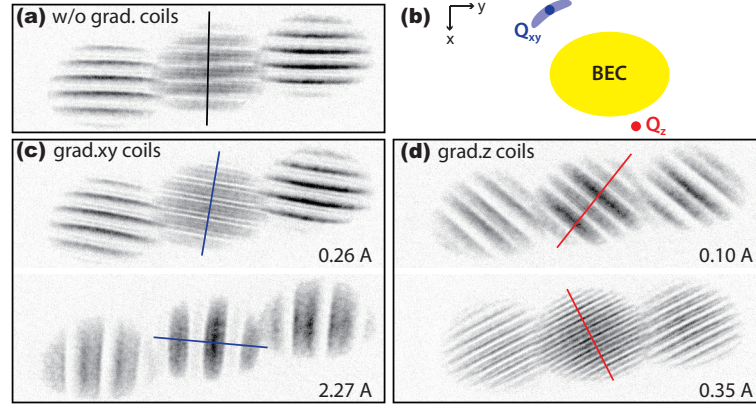


Figure D.1: Trying to figure out the magnetic field inhomogeneity of the (c) grad.xy and (d) grad.z coils using the Ramsey interferometry. The DC magnetic field is 35 mG and the interrogation time is $\tau = 10$ ms. The orientation of the field gradient, generated by the grad.z coils are confirmed as red line in below image. (b) illustrates predicted zero-field positions on top.

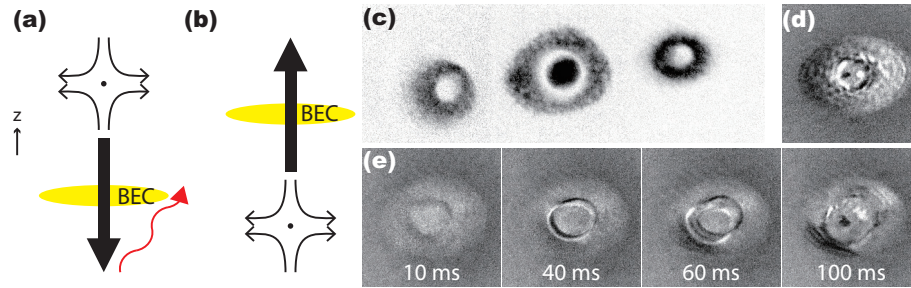


Figure D.2: Trying to observe the dynamics of Skyrmion decay. (a,b) Two schematic experimental sequences. (c) SG image of created Skyrmion after 24 ms spin separation. (d) Desired result. (e) Temporal evolution of (c), taken by *In-situ* magnetization image. The quadratic Zeeman energy, $q/h = 0.3$ Hz.

gradient. We used the quadrupole coils to generate quadrupole field gradient. The z -directional bias coils and Feshbach coils are used to control $\pm z$ -directional bias magnetic fields. The skyrmion was imprinted as in Fig. D(c). Then, the quadrupole fields was turned off and it went upward. Thus, for the sequence of Fig. D(a), the condensate felt the field inhomogeneity and skyrmion ring always split in fixed direction as in Fig. D(e). However, the backflow current of the Feshbach coils inhibited experiments with the sequence of Fig. D(b) at that time. Hence, we put the skyrmion decay study in the future, and moved on the study of the phase transition dynamics.